Spintronics.
Lecture notes.

I.V. Bobkova

Contents

Chapter 1

GMR, TMR and related phenomena

Progress in nanofabrication techniques has made it possible to create artificial structures such as magnetic multilayers and nanocontacts, the characteristic scale length L of which can be shorter than the spin diffusion length and the mean free path and can even be close to the Fermi wavelength λ_F. In these cases, novel transport phenomena occur: giant magnetoresistance (GMR), tunnel magnetoresistance (TMR), and ballistic magnetoresistance (BMR) are typical examples. GMR and TMR both occur when a change in the relative orientation of the magnetization in different regions causes a change of the electrical resistance. GMR occurs in structures containing ferromagnetic regions separated by nonmagnetic conducting regions, while for TMR the nonmagnetic regions are insulating. BMR occurs when the scale of the contact region of two ferromagnets is close to λ_F.

1.1 Spin-Dependent Transport in Ferromagnetic Metals

One of the most important requirements for MR in nanoscale ferromagnets is spin dependence of the electrical resistivity.

Few ferromagnetic materials are composed of a single element. The exceptions are the transition metals (TMs), such as Fe, Co, and Ni, and rare earth metals. This is in marked contrast to superconductivity, which appears in many pure metals. In rare earth metals, electrons responsible for transport and magnetism can be distinguished. However, this distinction is not clear in TMs, that is, both s- and d-electrons contribute to transport and magnetism. The electronic structure of TMs consists of mainly s- and d-orbitals. The relative position of the Fermi level E_F to the s- and d-states depends on the material, i.e., the number of s+d electrons per atom.

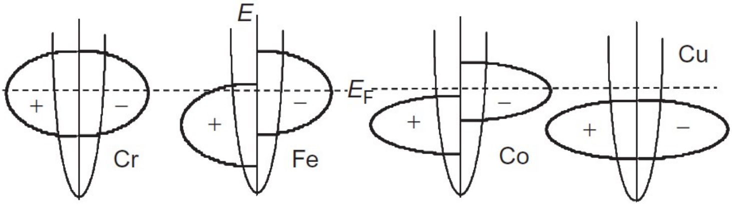

Figure 1.1: Adopted from [1]. Schematic DOS of Cr, Fe, Co, and Cu. + and - indicate majority and minority spin states, identical to up and down spin, respectively, in uniformly magnetized materials.

Fig. 1.1 shows the schematic density of states (DOS) of the typical TMs Cr, Fe, and Co, and the DOS of Cu. The electronic states are composed of wide s-bands and narrow d-bands. The d-part of the DOS is high because the d-states are almost localized near atoms. The s- and d-states hybridize to form complicated electronic states. The electronic structures for TMs give rise to the characteristic features of both magnetism and electrical transport. The spin dependence of the resistivity is governed by the spin dependence of the electronic states near the Fermi level, and by spin-dependent impurity potentials in ferromagnetic alloys.

The simplest formula for the electrical conductivity σ is given by the Drude formula:

$$\sigma = \frac{e^2 n \tau}{m}, \tag{1.1}$$

where e, n, τ and m are the electrical charge, carrier density, lifetime and effective mass of carrier electrons, respectively. For ferromagnets, the spin dependence of these quantities must be taken into account in the Drude formula, since the electronic states of ferromagnets are spin polarized due to the number of spin-up and spin-down electrons not being compensated. Basically, n, τ and m are all spin dependent. For transition metals the conductivity is mainly due to the s-electrons exhibiting a small effective mass. Therefore, the concentrations and masses of spin-up and spin-down electrons in Eq. (1.1) are approximately the same according to the s-band structure in Fig. 1.1. Most important is the spin dependence of the lifetime, since it affects electron scattering very strongly.

The lifetime is related to the mean free path l via the relation $l = v_F \tau$, where v_F is the Fermi velocity. For typical ferromagnetic metals, l is much shorter that the spin-diffusion length λ_s, and therefore the spins of the carrier electrons are well conserved in the time scale τ. In this case, $\uparrow$ and $\downarrow$ spin electrons can be treated independently in evaluating the electrical conductivity, that is, $\sigma = \sum_s \sigma_s$, where $s = \uparrow, \downarrow$. This assumption is the Mott's two-current model, which will be discussed below. Although Mott's two-current model explains the experimental results of electrical resistivity in ferromagnetic metals, it is rather difficult to confirm the model directly by experiment, since $\sigma_\uparrow$ and $\sigma_\downarrow$ cannot be separated independently from the σ data. However, Fert and Campbell [2] have approached the problem by measuring the residual resistivity and temperature dependence for various binary and ternary alloys and succeeded in deducing the ratio $\alpha = \sigma_\uparrow/\sigma_\downarrow$ for diluted alloys of Fe, Co, and Ni metals. The ratio is referred to as the α-parameter. α-Parameters for TM impurities in Fe are presented in Fig. 1.2.

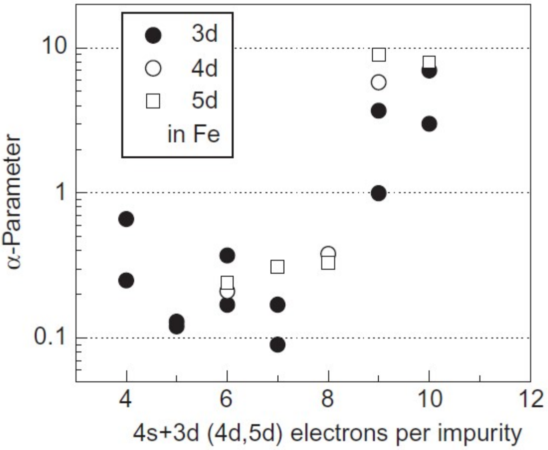

Figure 1.2: Adopted from [1]. Experimental values of α-parameters for 3d, 4d, and 5d TM impurities in Fe [2].

What is the main reason of the spin dependence of the scattering time? The spin dependence of τ caused by impurity scattering of electrons in ferromagnetic metals may be evaluated by using the formula:

$$\tau_s^{-1} = \frac{2\pi}{\hbar} N_i V_s^2 D_s(E_F) \tag{1.2}$$

which is given by the Born approximation, where N_i, V_s, and $D_s(E_F)$ are the impurity density, scattering potential, and

DOS at the Fermi energy E_F, respectively. Here, both V_s and $D_s(E_F)$ are spin dependent. Eq. (1.2) indicates that the lifetime becomes short as the scattering potential becomes large and the number of final states of the scattering process increases. Let us consider TM impurities in Fe. Since $D_\uparrow(E_F) \sim D_\downarrow(E_F)$ for ferromagnetic Fe, the spin dependence of the lifetime is caused mainly by V_s. From the other hand, the spin dependence of τ can also be caused by $D_s(E_F)$. As an example, one can consider Co, see Fig. 1.1, where the majority s-electrons cannot be scattered into d-states, what leads to the increased mobility and the reduced resistance.

1.2 GMR

Magnetic multilayers are composed of an alternating stack of thin magnetic and nonmagnetic layers. The thickness of each layer is a few nanometers. Trilayers, where a nonmagnetic layer is sandwiched by two magnetic layers, can also be considered to be multilayers. Some magnetic multilayers show large MR. When the nonmagnetic layers are metals, the MR is called giant MR (GMR) and when the nonmagnetic layer in a trilayer is an insulator, the MR is called tunnel MR (TMR).

Magnetic multilayers have the following two important characteristics:

1. The alignment of the magnetization of the magnetic layers is easily controlled by an external magnetic field, since the coupling between the magnetization of the magnetic layers is weakened by the presence of the nonmagnetic layer between them.

2. Each layer is thin enough for carrier electrons to feel a change in the magnetization direction of the magnetic layers (the spin does not have enough time to relax within a layer).

GMR and TMR depend strongly on the type of magnetic and nonmagnetic layers, and their combination.

1.2.1 Experiments on GMR.

The basic structure of magnetic multilayers composed of a ferromagnetic A metal and a nonmagnetic B metal is shown in Fig. 1.3. The thickness of each layer is $1 - 10$ nm and the number of layers ranges from 3 (for trilayers) to about 100. Fe, Co, Ni, and their alloys are frequently used for the ferromagnetic A layers, while nonmagnetic TMs such as Cr and Ru or noble metals Cu, Ag, and Au are used for the nonmagnetic B layers.

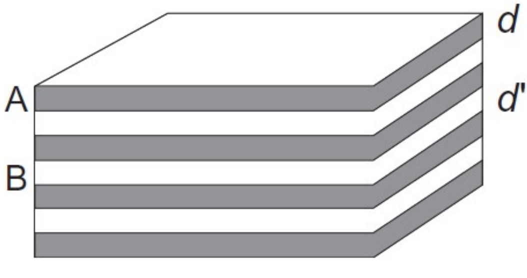

Figure 1.3: Adopted from [1]. Schematic picture of magnetic multilayers with ferromagnetic A and nonmagnetic B layers. d and d' indicate the layer thickness.

The first observation of antiparallel (AP) coupling between magnetic layers was reported by Grunberg et al. [3] for Fe/Cr trilayers. They also observed negative MR, that is, a resistivity reduction under an external magnetic field. The magnitude of the MR of Fe/Cr trilayers was observed to be a few percent. Two years later, Fert's group [4] reported MR as large as 40% for Fe/Cr multilayers. This MR was the largest so far observed for magnetic metal films and was called giant MR (GMR).

After the discovery of GMR, many experimental works have been performed.

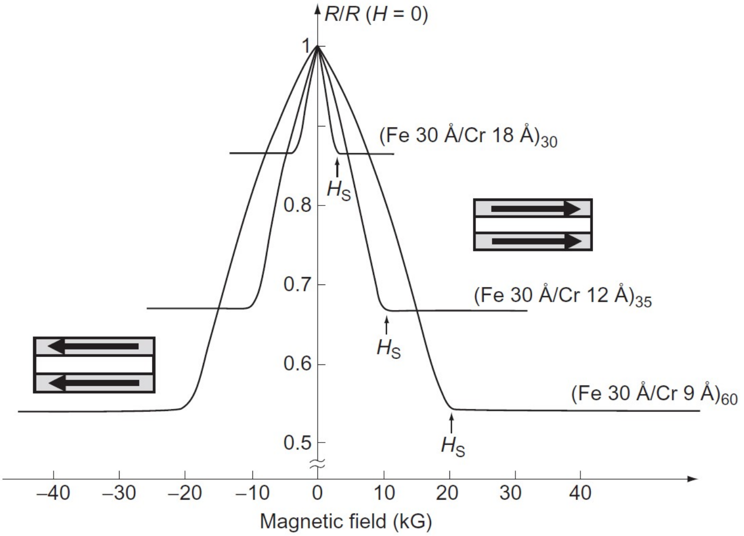

Figure 1.4: Adopted from [1]. Resistivity change due to an external magnetic field for Fe/Cr multilayers [4].

Fig. 1.4 shows the experimental results for Fe/Cr multilayers [4]. The resistivity decreases with increasing magnetic field due to a change in the alignment of the magnetization of the Fe layers. The resistivity is high when the alignment is AP and is low when the alignment is parallel (P). The magnitude of the MR is expressed by the so-called MR ratio, defined as:

$$MR = \frac{\rho_{AP} - \rho_P}{\rho_{AP}} \tag{1.3}$$

or

$$MR = \frac{\rho_{AP} - \rho_P}{\rho_P}. \tag{1.4}$$

Tables 1.5 show MR ratios observed for several combinations of magnetic and nonmagnetic metals. We see that the

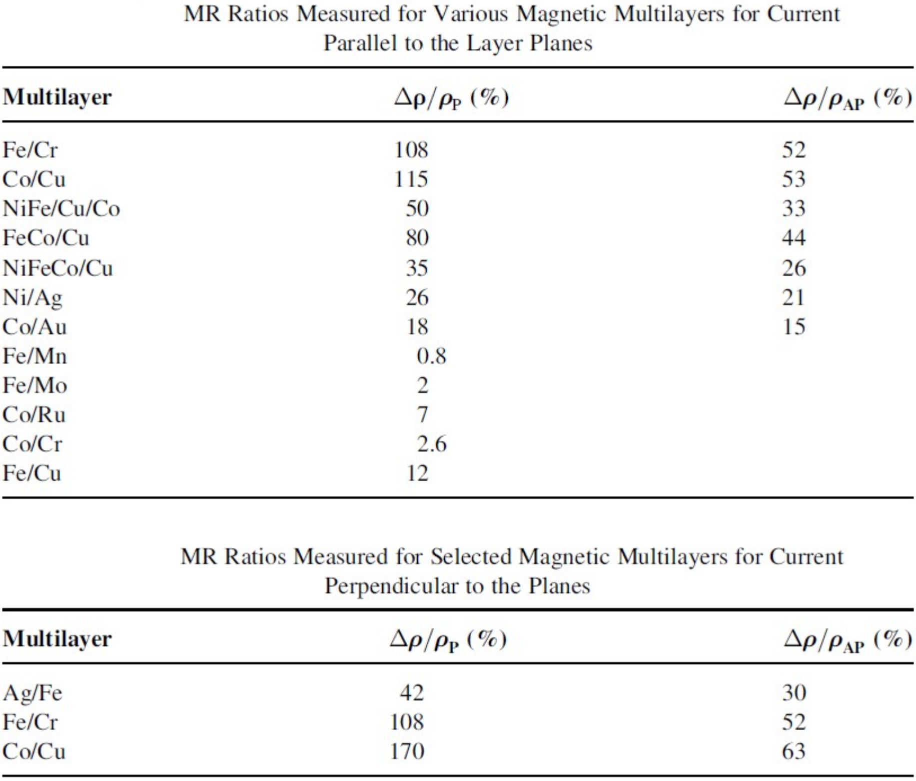

MR Ratios Measured for Various Magnetic Multilayers for Current Parallel to the Layer Planes

Multilayer	$\Delta\rho/\rho_P$ (%)	$\Delta\rho/\rho_{AP}$ (%)
Fe/Cr	108	52
Co/Cu	115	53
NiFe/Cu/Co	50	33
FeCo/Cu	80	44
NiFeCo/Cu	35	26
Ni/Ag	26	21
Co/Au	18	15
Fe/Mn	0.8	
Fe/Mo	2	
Co/Ru	7	
Co/Cr	2.6	
Fe/Cu	12	

MR Ratios Measured for Selected Magnetic Multilayers for Current Perpendicular to the Planes

Multilayer	$\Delta\rho/\rho_P$ (%)	$\Delta\rho/\rho_{AP}$ (%)
Ag/Fe	42	30
Fe/Cr	108	52
Co/Cu	170	63

Figure 1.5: MR ratios.

MR ratio depends on the combination of metals. Thus, an issue to be clarified is the material dependence of GMR and the relation between the MR ratio and the electronic structures of the constituent metals of the magnetic multilayers.

GMR appears when the AP alignment of the magnetization is changed to P alignment by an external magnetic field. Therefore, AP alignment of the magnetization is a prerequisite for GMR. A detailed study of the alignment of magnetization has found that the coupling of magnetization in magnetic layers changes as a function of the nonmagnetic layer thickness.

The coupling between magnetic layers is called interlayer exchange coupling. Fig. 1.6 shows an experimentally determined oscillation of coupling energy as a function of layer thickness [5].

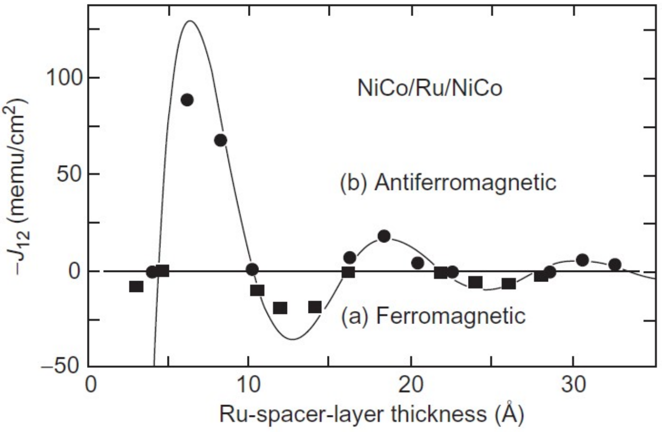

Figure 1.6: Oscillation of coupling energy as a function of nonmagnetic layer thickness in NiCo/Ru/ NiCo multilayers [5].

The period of the oscillation is rather long and the magnitude decays as the thickness of the nonmagnetic layer increases. The effect has the same origin as the so-called Ruderman-Kittel-Kasuya-Yosida (RKKY) interaction between magnetic impurities in metals. That is, one of the magnetic layers polarizes the conducting electrons in the nonmagnetic spacer, and the polarization of the conductivity electrons interacts by the exchange mechanism with the magnetization of the other layer. The decay of the magnitude for multilayers is proportional to L^2, where L is the nonmagnetic layer thickness, in contrast to r^3 for the RKKY interaction.

Multilayers with thicker nonmagnetic layers have nearly zero exchange coupling; however, the magnetization direction of the magnetic layers may be controlled by using the difference in the coercive force between magnetic layers of different metals. An example is Co/Cu/NiFe multilayers shown in Fig. 1.7, in which NiFe is a soft magnet with a magnetization easily changed by a weak external magnetic field.

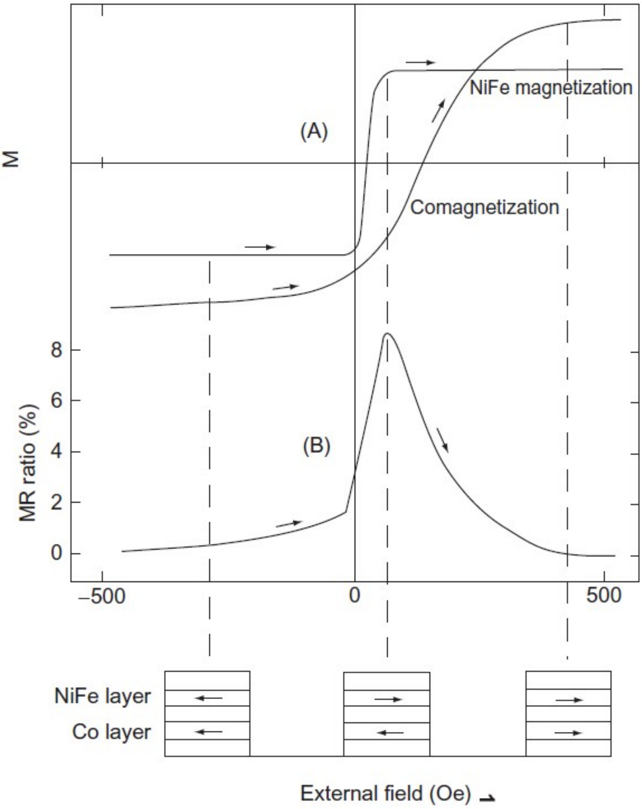

Figure 1.7: Adopted from [1]. Experimental results of GMR for noncoupling Co/Cu/NiFe magnetic multilayers. [6].

Technological applications of GMR, for example, sensors, require a sharp response of the magnetization direction to the external magnetic field within a few Oersteds. To achieve such sensitivity, a trilayer structure with an attached antiferromagnet has been designed. The magnetization of the magnetic layer adjacent to the antiferromagnetic layer is pinned by the antiferromagnetism and only the other magnetic layer responds to the external magnetic field. This kind of trilayer is called a spin valve. PtMn and FeMn are typical antiferromagnets used in spin valves.

The experiments presented so far have used a geometry with the current flowing parallel to the layer planes. GMR with this geometry is called current-in-plane (CIP). GMR with a geometry with current flowing perpendicular to the planes is called CPP.

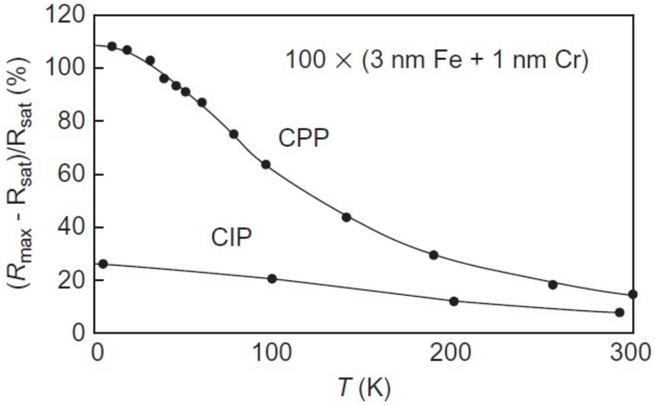

Figure 1.8: Temperature dependence of CPP-GMR for a microfabricated sample of Fe/Cr multilayers is compared with that of CIP-GMR. Adopted from [1].

The temperature dependence of CPP-GMR for a microfabricated sample of Fe/Cr multilayers is compared with that of CIP-GMR in Fig. 1.8. We see that CPP-GMR is much larger than CIP-GMR, which is a general trend for GMR. It will be explained below. The disadvantage of the CPP geometry is that the resistivity of a sample is too small to be detected, since the layer thickness is usually less than micrometers and the resistivity of the leads is overwhelming. Therefore, one needs to use special methods to detect the CPP-GMR, such as utilizing superconducting leads or microfabricating the sample.

1.2.2 Phenomenological explanation of GMR.

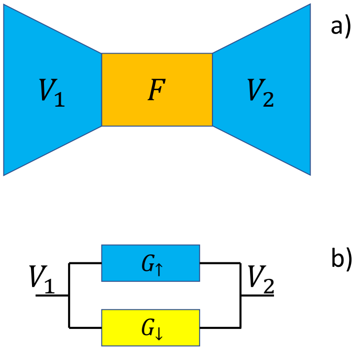

Figure 1.9: (a) A ferromagnetic metal coupling two particle reservoirs with potentials V_1 and V_2; and (b) circuit model of transport through a single ferromagnetic layer. The conductance of spin-up electrons is $G_\uparrow$ and the conductance of spin-down electrons is $G_\downarrow$.

In the framework of the two-channel resistor model a ferromagnet between two leads is described by the equivalent scheme shown in Fig. 1.9(b). The electric current through the ferromagnet can be found as a sum of two spin channels

$$j = j_\uparrow + j_\downarrow = (G_\uparrow + G_\downarrow)(V_1 - V_2) = G(V_1 - V_2), \qquad (1.5)$$

while the spin current is

$$j_s = j_\uparrow - j_\downarrow = Pj, \qquad (1.6)$$

where we have introduced the total conductance of the junction $G = G_\uparrow + G_\downarrow$ and the conductance spin polarization $P = (G_\uparrow - G_\downarrow)/(G_\uparrow + G_\downarrow)$. Here and below we will denote by $P_A = (A_\uparrow - A_\downarrow)/(A_\uparrow + A_\downarrow)$ the degree of spin polarization of a general spin-dependent quantity A.

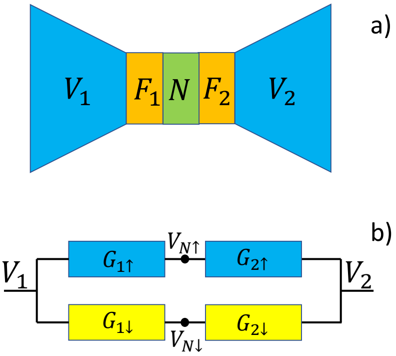

Figure 1.10: (a) A ferromagnetic spin-valve; and (b) circuit model of transport through two ferromagnets in series.

Now let us consider in the framework of the two-resistor model a spin valve. Sketch of the system and the equivalent scheme are presented in Fig. 1.10. In contrast to the bulk of a ferromagnet the spin accumulation $V_s = V_{N,\uparrow} - V_{N,\downarrow}$ in the normal interlayer between two ferromagnets can be nonzero, where $V_{N,\uparrow(\downarrow)}$ are the electrochemocal potentials of the normal interlayer for spin-up and spin-down channels, respectively. From the equivalent scheme shown in Fig. 1.10(b) it is easy to find that

$$V_{N\uparrow,\downarrow} = \frac{G_{2\uparrow,\downarrow}V_2 + G_{1\uparrow,\downarrow}V_1}{G_{2\uparrow,\downarrow} + G_{1\uparrow,\downarrow}}. \tag{1.7}$$

Expressing $G_{i\uparrow,\downarrow}$ via the total conductance of the corresponding junction G_i and the conductance spin polarization P_i as $G_{i\uparrow,\downarrow} = G_1(1 \pm P_i)/2$ one can obtain the spin accumulation and the spin current in the interlayer from Eq. (1.7):

$$V_s = \frac{2(V_1 - V_2)G_1G_2(P_1 - P_2)}{[G_1(1-P_1) + G_2(1-P_2)][G_1(1+P_1) + G_2(1+P_2)]}, \tag{1.8}$$

$$j_s = \frac{G_1G_2[G_1(1-P_1^2)P_2 + G_2(1-P_2^2)P_1](V_1 - V_2)}{[G_1(1-P_1) + G_2(1-P_2)][G_1(1+P_1) + G_2(1+P_2)]}. \tag{1.9}$$

Let us consider a symmetric spin-valve with $G_1 = G_2$ in parallel (P) $P_1 = P_2$ and antiparallel (AP) $P_1 = -P_2$ configurations:

In the P-configuration:

$$V_s = 0 \tag{1.10}$$

$$j_s = \frac{GP}{2}(V_1 - V_2), \tag{1.11}$$

while in the AP-configuration:

$$V_s = (V_1 - V_2)P \tag{1.12}$$

$$j_s = 0. \tag{1.13}$$

Now let us find the magnetoresistance of the spin valve. It can be defined as

$$MR = \frac{R_{AP} - R_P}{R_{AP}}. \tag{1.14}$$

The resistance of the general spin-valve can be found as

$$R^{-1} = \frac{j_\uparrow + j_\downarrow}{V_1 - V_2} = \frac{G_1G_2[G_1(1-P_1^2) + G_2(1-P_2^2)]}{[G_1(1-P_1) + G_2(1-P_2)][G_1(1+P_1) + G_2(1+P_2)]}. \tag{1.15}$$

$$R_P^{-1} = \frac{G}{2}, \tag{1.16}$$

$$R_{AP}^{-1} = \frac{G(1-P^2)}{2}, \tag{1.17}$$

$$MR = P^2. \tag{1.18}$$

It is seen that the resistance of the AP state is higher in the framework of our model. This is because the applied voltage is used in part for the kinetic energy cost associated to the accumulation of spins, and this accumulation is maximal for the AP-configuration. The described model is oversimplified and does not take into account the finite resistance of the normal interlayer and the spin-flip scattering. Now we consider the influence of the finite resistance of the interlayer, and in the next section we are going to develop a theory, which is able to properly account for the spin-flip scattering.

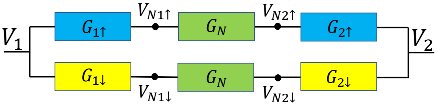

Figure 1.11: Circuit model of transport through two ferromagnets in series taking into account the finite resistance of the normal interlayer.

The equivalent scheme of the spin-valve taking into account the interlayer resistance is shown in Fig. 1.11. Basing on this scheme it is easy to calculate that for the symmetric spin-valve

$$MR = \frac{16 G_N^2 P^2}{\left[G(1-P^2) + 4G_N\right]^2}. \tag{1.19}$$

It is seen that the finite resistance of the spin-valve always reduces magnetoresistance $MR_{G_N} < MR_{G_N \to \infty}$. In case $G_N \ll G$, which is relevant for semiconductor interlayers, the magnetoresistance is greatly reduced $MR \sim (G_N/G)^2$, what is called by "conductivity mismatch problem".

It is important to realize that the parameters $G_{\uparrow,\downarrow}$ are effective parameters. For typical GMR multilayers they cannot be considered as bulk conductivities of the ferromagnets. The bulk conductivity of the ferromagnets is not relevant to to GMR multilayers because characterictic lengths of the layers are typically smaller that the mean free path.

There are two possible sources of spin-dependent resistivity in multilayers from the viewpoint of electronic states:

1. Spin-dependent resistivity caused by interfacial roughness. As described, the origin of the spin-dependent resistivity in metals and alloys is the spin dependence of the scattering potentials caused by roughness. The roughness due to random arrangement of atoms also exists in multilayers. In molecular beam epitaxy (MBE) and sputtering fabrication methods, it is impossible to avoid intermixing of atoms at interfaces. The intermixing of magnetic A atoms and nonmagnetic B atoms at an A/B interface gives rise to spin-dependent random potentials near the interface. The situation is similar to that in ferromagnetic alloys.

2. Band matching/mismatching at interfaces. The essence of the origin of electrical resistivity is the absence of translational invariance along the current direction, because the momentum of electrons need not be conserved in this case. When the interfaces are clean, translational invariance parallel to the layer planes is satisfied and there is no electrical resistivity. Even in this case, however, there is electrical resistivity perpendicular to the layer planes, since there is no translational invariance along this direction for thin multilayers. In this case, the difference between the electronic structure of the

constituent metals of the multilayers acts as a source of spin-dependent electrical resistivity and gives rise to CPP-GMR. In Co/Cu multilayers, for example, band matching between ↑ spin states is much better than between ↓ spin states, as schematically shown in Fig. 1.1. Therefore, $\rho_\uparrow < \rho_\downarrow$. In Fe/Cr multilayers, the opposite relation, $\rho_\uparrow > \rho_\downarrow$ is realized.

For current flowing perpendicular to the planes, both are crucial for the spin dependence of the resistivity, while the spin-dependent random potential is likely to be more greatly responsible for GMR for current flowing parallel to the planes.

1.3 TMR.

TMR in ferromagnetic tunnel junctions (FTJs) was reported prior to the discovery of GMR (1975,1982). The observed MR ratios, however, were rather small at the time. A large TMR at room temperature was reported for Fe/Al-O/Fe in 1995, and it has attracted considerable attention due to its wide potential application in sensors and memory storage devices in the near future.

FTJs are made of a thin (about 1-nm thick) nonmagnetic insulator sandwiched between two ferromagnetic electrodes. A schematic diagram of such a junction is shown in Fig. 1.12. The ferromagnetic metals used are predominantly Fe, Co, and their alloys, while amorphous Al_2O_3 is one of the most stable materials for the insulating barrier. Recently, a single-crystal MgO layer has been used as the barrier in order to generate high TMR ratios.

Fig. 1.13 shows the experimental results for the resistance in an Fe/Al-O/Fe tunnel junction as a function of the external magnetic field. The resistance is high when the magnetization of the two ferromagnetic electrodes is AP, and it is low when the magnetization is parallel. One of the characteris-

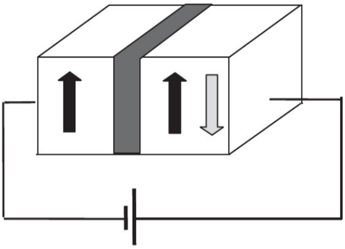

Figure 1.12: Adopted from [1]. A schematic representation of the FTJ.

tics of TMR is that the external magnetic field required to rotate the magnetization is sufficiently low. This is because there is almost no coupling between the magnetizations of the two electrodes as a result of the insulating barrier inserted between them. The AP and P alignments of the magnetization are realized by using a small difference in the coercive force between the two ferromagnets. The current flows perpendicular to the layer planes, which is similar to CPP-GMR. The resistance in the FTJs is much higher than that in CPP-GMR. This makes it possible to measure the junction resistance without microfabricating the samples. This could be considered to be another characteristic of TMR.

Now we discuss theoretical explanations of TMR. Let us denote the left and right electrodes as L and R, respectively. When the tunneling process is independent of the wave vectors of tunneling electrons, the tunnel conductance Γ is proportional to the product of the densities of states of the L and R electrodes, and is given by

$$\Gamma \propto \sum_s D_{Ls}(E_F) D_{Rs}(E_F), \tag{1.20}$$

where s denotes the spin. The proportionality constant includes the transmission coefficient of electrons through the in-

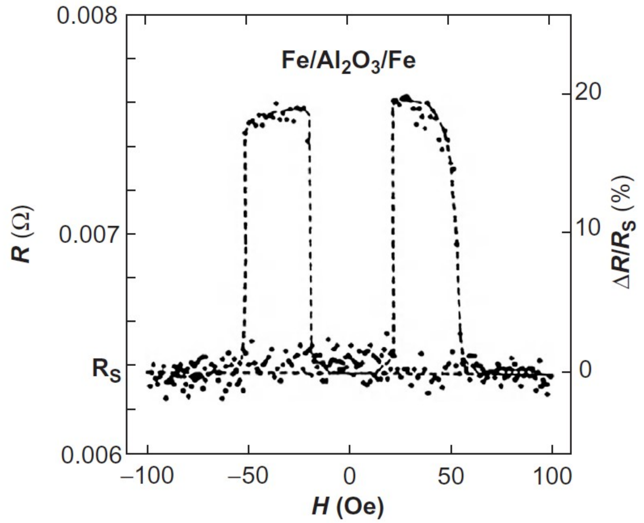

Figure 1.13: Experimental results for the resistance in an Fe/Al-O/ Fe tunnel junction [8].

sulating barrier. By using this expression, the conductance for P magnetization alignment is given by

$$\Gamma_P \propto D_{L+}(E_F)D_{R+}(E_F) + D_{L-}(E_F)D_{R-}(E_F), \qquad (1.21)$$

and that for AP magnetization alignment is given by

$$\Gamma_{AP} \propto D_{L+}(E_F)D_{R-}(E_F) + D_{L-}(E_F)D_{R+}(E_F). \qquad (1.22)$$

Since the resistivity $\rho_{P(AP)}$ corresponds to $\Gamma^{-1}_{P(AP)}$, the MR ratio is given by:

$$MR = \frac{\Gamma^{-1}_{AP} - \Gamma^{-1}_{P}}{\Gamma^{-1}_{AP}} = \frac{2P_L P_R}{1 + P_L P_R}, \qquad (1.23)$$

where $P_{L(R)}$ is the spin polarization of L(R) electrodes and is defined by:

$$P_{L(R)} = \frac{D_{L(R)+} - D_{L(R)-}}{D_{L(R)+} + D_{L(R)-}}. \qquad (1.24)$$

Although the transmission coefficient governs the magnitude of the tunnel conductance, it does not appear in the expression for the MR ratio. An intuitive picture of the tunneling process explained above is shown in Fig. 1.14, where in P alignment, majority and minority spin electrons in the L electrode tunnel through the barrier into the majority and minority spin states in the R electrode, respectively. In AP alignment, however, the majority and minority spin electrons in L electrode tunnel into the minority and majority spin states in R electrode, respectively.

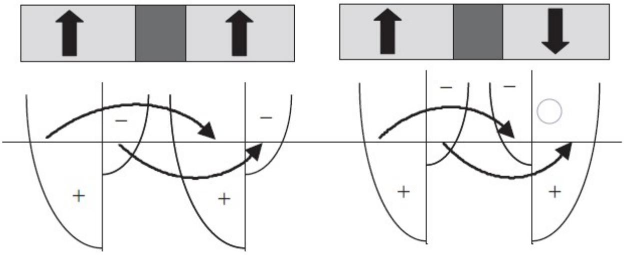

Figure 1.14: Adopted from [1]. A schematic representation to show the tunneling process in FTJs for P and AP alignments.

Eq. (1.23) indicates that the spin polarization of the electrodes govern the MR ratio. The spin polarization has been experimentally determined by using junctions of ferromagnet/Al/superconductor, or by analyzing the tunneling spectrum obtained using point contacts. Measured values of the spin polarization are shown in Table 1.15. Using these values, the experimentally measured MR ratios are explained rather well. For example, the MR ratio measured for Fe/Al-O/Fe junctions is about 0.3 and this value is close to the theoretical value calculated by using the experimental value of P for Fe. However, the MR ratio observed for a single crystal Fe/MgO/Fe junction is 0.7-0.8, which cannot be explained in terms of the spin polarization of Fe. It is also difficult to explain the spin polarization P by using a first-principles calculation. The ratios of P deduced from the height of the DOS at the Fermi energy are inconsistent with experimentally measured ones, for example, theoretical values for P are negative for Co and Ni, while experimental ones are positive. Bulk Fe has a positive value of P, while surface Fe has a negative value. In order to explain TMR, one should study the spin polarization of the tunnel conductance itself.

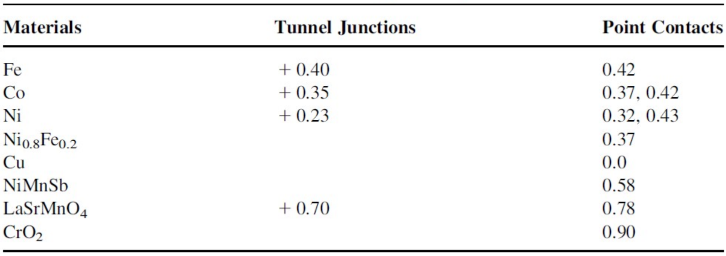

Materials	**Tunnel Junctions**	**Point Contacts**
Fe	+ 0.40	0.42
Co	+ 0.35	0.37, 0.42
Ni	+ 0.23	0.32, 0.43
$Ni_{0.8}Fe_{0.2}$		0.37
Cu		0.0
NiMnSb		0.58
$LaSrMnO_4$	+ 0.70	0.78
CrO_2		0.90

Figure 1.15: Adopted from [1]. Spin polarizations observed in tunnel junctions and point contacts for various metals.

When the DOS of either a ↑ or ↓ spin state is zero at the Fermi level, and one of two spin states is metallic and the other is insulating, the metals are referred to as halfmetals. The spin polarization P of these half-metals is 100%, and therefore halfmetals have potential applicability as magnetoresistive devices. Many oxides, including CrO_2, Fe_3O_4, and perovskite $LaSrMnO_3$, have been shown to be half-metallic by using first-principles band calculations. The first theoretical prediction for half-metallicity was done for Heusler alloys, which contain TM elements. In experiments in which point contacts and tunnel junctions were used to measure spin polarization, lower values than 100% were obtained for P (e.g., 90% for CrO_2, $70-85\%$ for $LaSrMnO_3$, and 60% for Heusler alloys). Recently, relatively high MR ratios have been observed in FTJs with Heusler alloys, suggesting that the value of P is about 86%.

1.4 BMR.

Garcia et al. [9] have measured the MR effect for Ni point contacts, and reported that the MR ratio becomes large when the conductance approaches 0. The maximum MR ratio was 280%. The results are shown in Fig. 1.16. The MR effect thus observed was termed ballistic magnetoresistance (BMR). The interpretation of BMR is connected to the phenomenon of conductance quantization in metals.

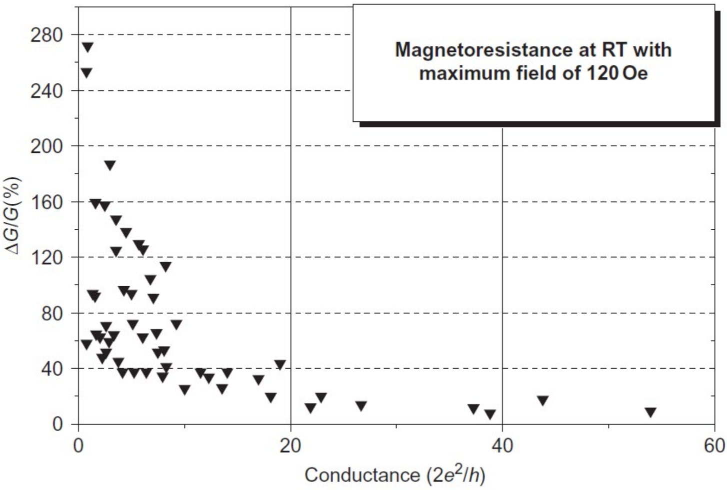

Figure 1.16: Experimental results of conductance change as a function of quantized conductance in point contacts [9].

When a current flows in a region that has a length scale shorter than the mean free path, the conductance becomes quantized. The quantization of the conductance was discovered by van Wees et al. in a two-dimensional electron gas (2DEG). They controlled the width of a channel in which electrons flowed by applying a gate voltage to 2DEG, and observed that the conductance changed in a stepwise manner, in steps of $2e^2/h$. This phenomenon of quantized conductance may be understood as follows. Constricted regions, in which a current flows, may be considered to be pseudo-one-dimensional. The electronic state of such constricted regions is quantized perpendicular to the current flow. The quantization of the electronic state is characterized by the Fermi wavelength λ_F. When the width of the constricted region is close to λ_F, only one state is available for electrons, and therefore two electrons (having up and down spins) may contribute to a current, giving rise to a conductance of $\Gamma_0 = 2e^2/h$. Indeed, the current of a one-dimensional chain subject to a voltage is given as:

$$I = 2e \int\limits_{E_F}^{E_F+eV} D(E)v(E)dE, \tag{1.25}$$

where using the relations for free electrons the DOS $D(E) = (1/2\pi\hbar)\sqrt{m/2E}$ and the velocity of electrons $v(E) = p/m$. Therefore, the conductance is given as:

$$\Gamma = \frac{2e^2}{h}. \tag{1.26}$$

The factor 2 indicates spin degeneracy. Because only two propagating states exist in a one-dimensional chain, that is, left going and right going waves, there is only one conducting path (called a channel) where electrons flow for each spin. The channel gives a conductance of $\Gamma_0 = 2e^2/h$, which is called the quantum conductance. This value is 3.43107 cm/s and is equal to $(26k\Omega)^{-1}$.

If the width of the sample is increased, the conductance increases stepwise in steps of $(2e^2/h)n$. The length scale of the constricted region is usually smaller than the mean free path, and the effect of scattering may be neglected. Such transport is referred to as ballistic transport. Conductance quantization was first observed in semiconductors. Conductance quantization can be easily observed in semiconductors since λ_F is several 10 nm. By contrast, λ_F in metals is 1 nm, which makes the observation of conductance quantization difficult in conventional metals. To realize ballistic transport in metals, the constricted region should be less than 1 nm. Potential methods for achieving this include the break-junction method, in which a narrow wire is slowly bent to produce a small link just before breakdown of the wire, and the point-contact method in which the sharp tip of metallic wire is contacted onto the metals surface.

The factor of 2 that appears in the quantized conductance Γ_0 indicates spin degeneracy. Since spin degeneracy is lifted in ferromagnets, conductance quantization might be expected to be given by $\Gamma_0/2$. In order to confirm this expectation, many experiments have been performed with break junctions and point contacts made of ferromagnets. Fig. 1.17 shows the average conductance observed for many break junctions made from Ni wires [10]. The results show that the quantized conductance is Γ_0 when an external magnetic field H of less than 50 Oe is applied, but it is $\Gamma_0/2$ when $H > 50Oe$.

So far a complete understanding of BMR has not been achieved. However, there are suggestions that the conductance quantization is of relevance for this phenomenon. The Imamura et al. [11] have studied the conductance quantization for nanocontacts of two ferromagnets, and showed that the parameter region at which a conductance quantization of $\Gamma_0/2$ appears depends on the alignment of the magnetization of the two ferromagnets. A difference in the conductance quantization between the P and AP alignments of the magnetization may give rise to a large MR ratio. There are also other interpretations of the BMR. One of them is to attribute the large MR to the vanishing of the domain walls at the ferromagnetic

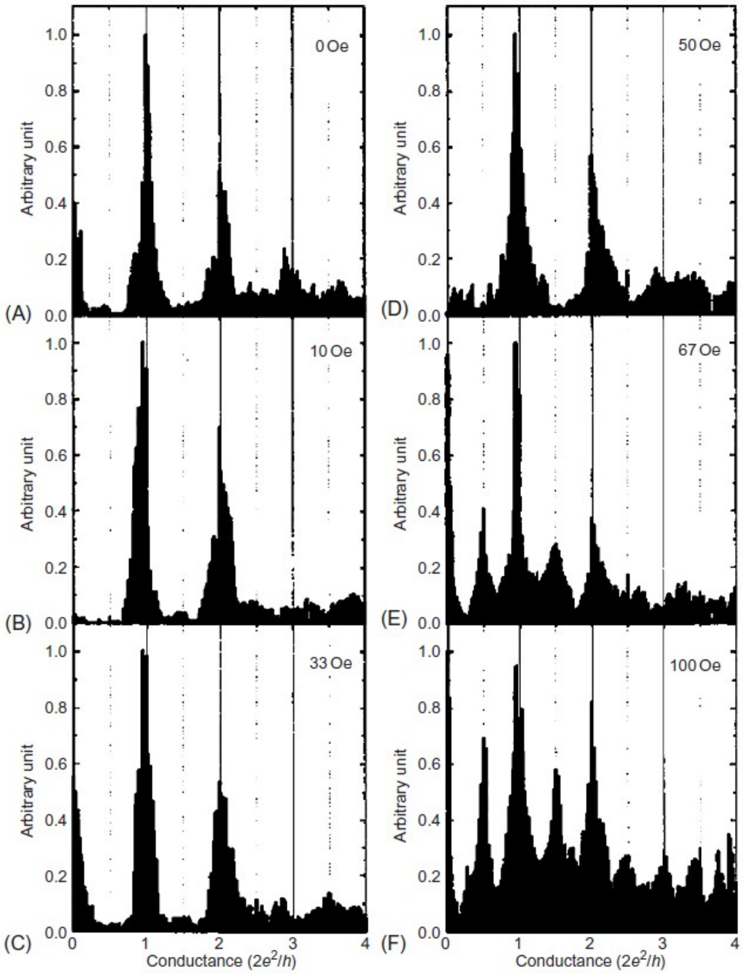

Figure 1.17: Experimental results of conductance quantization performed for many break junctions of Ni wires with and without an external magnetic field [10].

constriction.

1.5 Other magnetoresistive phenomena.

1.5.1 Normal magnetoresistance.

The general situation is characterized by increase of resistance when a magnetic field is applied. It is called positive or normal magnetoresistance. It occurs in non-magnetic metals as a consequence of the Lorenz force. The external field forces the electrons on spiral trajectories. Thus, the effective mean free path between two collisions is reduced which leads to an increase of the resistance.

Below the Curie temperature ferromagnetic transition metals exhibit a reduced resistance compared to non-magnetic transition metals like Pd, see Fig. 1.18.

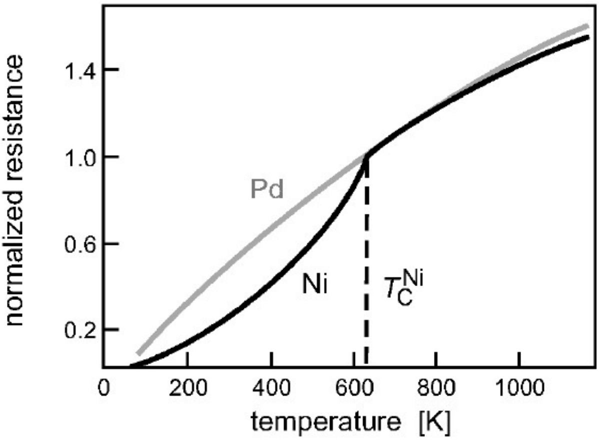

Figure 1.18: Adopted from [12]. Resistance as a function of temperature for Ni and Pd. The curves are normalized with respect to the critical temperature of Ni. Data taken from [13].

It is called negative magnetoresistance. As it was mentioned before, for transition metals the conductivity is mainly determined by s-electrons with small effective mass. The resistance can be explained by scattering of the s-electrons into the empty states of the d-bands near the Fermi level. The DOS for Ni is similar to the DOS of Co, shown in Fig. 1.1. Therefore, the majority s-electrons cannot scatter into the corresponding d-states, what leads to the increased mobility and reduced resistance. The DOS of Pd is close the DOS of Cr, that is, there are a lot of empty d-states for electrons to scatter at the Fermi level and, therefore, the resistance for Pd is high.

1.5.2 Anisotropic magnetoresistance.

The effect of anisotropic magnetoresistance (AMR) is induced by current and occurs in ferromagnetic metals like Fe, Ni, Co upon application of an external magnetic field. The physical origin of the AMR is a spin-orbit coupling on 3-d orbitals. In the presence of the spin-orbit coupling $\Delta E_{so} \sim \boldsymbol{LS}$ the orbital angular momentum on the orbitals tends to align collinear with the magnetization (which is determined mainly by the spin of d electronic shell). In this configuration the cross section of s-electrons scattering into the d-orbital is increased, if they flow along the magnetization ($\boldsymbol{I}||\boldsymbol{M}$) and is decreased if they flow perpendicular to the magnetization ($\boldsymbol{I} \perp \boldsymbol{M}$) see Fig. 1.19. The magnetization direction is typically determined by the direction of the applied field.

The magnetic field dependence of the AMR is presented in Fig. 1.20. There is no difference between resistances at zero field. Upon application of the magnetic field the difference between the resistance for current parallel to the magnetization $R_{\|}$ and the resistance for current perpendicular to the magnetization $R_{\perp}$ becomes immediately apparent. $R_{\perp}$ decreases while $R_{\|}$ increases. With increasing the magnitude of the applied field the difference between resistances rapidly reaches a

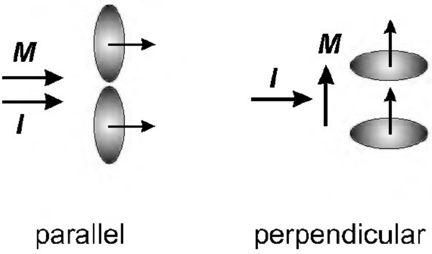

Figure 1.19: Adopted from [12]. Origin of anisotropic magnetoresistance.

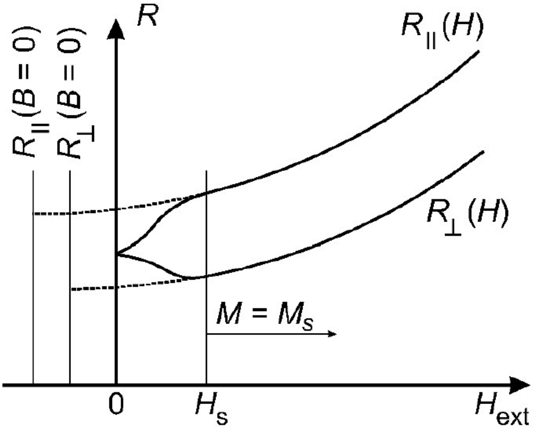

Figure 1.20: Adopted from [12]. Resistance as a function of an external magnetic field.

maximum at H_s.

The angle dependence of the resistance for an arbitrary mutual orientation of the magnetization and the current is

$$R(\theta) = R_{\perp} + (R_{\|} - R_{\perp}) \cos^2 \theta, \tag{1.27}$$

where θ is the angle between the directions of the current and the magnetization.

1.6 Applications.

1.6.1 Hard disk drive magnetic read head.

Magnetic recording read heads have come a long way since the introduction of magnetic disk drive technology by IBM in 1957. Since then, recording densities increased from $2kBit/in^2$ to about $750GBit/in^2$ in the year 2011. Thus, over the years, magnetic recording head technology has evolved from bulk inductive heads with wire-wound coils in the early years of magnetic recording to lithographically defined thin film inductive heads in 1979 to anisotropic magnetoresistance (AMR) read heads in 1991 to current-in-plane giant magnetoresistance (CIP-GMR) read heads in 1996 and most recently to tunnel magnetoresistance (TMR) read heads in 2006. With the evolution of the recording technology, the areal recording density has increased dramatically.

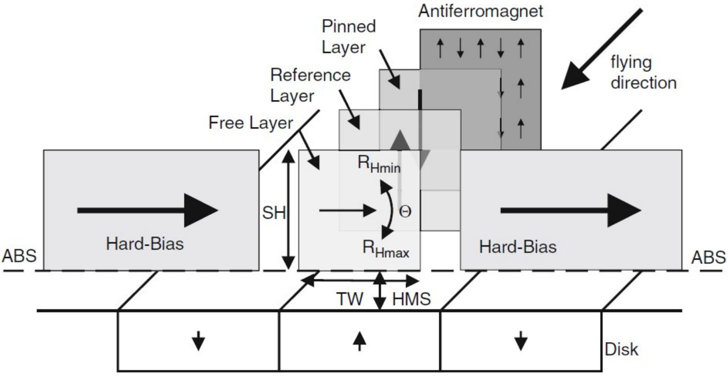

Figure 1.21: Adopted from [14]. Schematic view of a TMR magnetic read head.

Generally, the TMR effect follows the simple geometrical relationship

$$TMR = \frac{R_{AP} - R_P}{R_{AP}} \cos(\boldsymbol{M}_1, \boldsymbol{M}_2). \tag{1.28}$$

The TMR varies with the cosine of the angles between the two magnetizations. In a TMR structure such as read head or an MRAM cell, these layers are generally referred to as the free and reference layers. However, unlike in an MRAM cell where full reversal of the free layer magnetization from parallel to antiparallel alignment with respect to the reference layer and a finite switching field is desired to maximize TMR and stabilize the bit, a read sensor is a linear analog device, and thus only small rotations of the free layer magnetization are utilized. Schematic view of a TMR read-sensor is shown in Fig. 1.21. In order to linearize the response of a TMR read sensor, the free and reference layer magnetizations are prepared perpendicular to each other in the quiescent state in which no field is applied. A rotation of the free layer magnetization will lead to the variation of the angle between the magnetization directions of the reference and free layers, which is detectable as the change in electrical resistance.

1.6.2 MRAM.

The ideal memory, a fast and dense nonvolatile memory with unlimited endurance, does not exist. Consequently, most systems use a combination of working memories such as SRAM and DRAM and storage memories such as NAND Flash and HDD. The working memories have fast read/write access speed and unlimited endurance but do not have nonvolatility. The storage memories have nonvolatility and density but do not have fast read/write access speed. They work cooperatively with each other to attain both fast accessibility and nonvolatility of data. However, there are drawbacks. When such a system is turned on, data, which is located in storages should be copied to the working memories to set up memory systems for usage. The setup is called booting and it takes about a minute in the case of personal computers. When such a system is in use, the working memories consume a lot of energy to keep those data because SRAM leaks current and DRAM needs refresh operation. The battery power consumption is a major problem for mobile systems such as cellular phones.

Fast nonvolatile memories with unlimited endurance have a potential to solve these problems. MRAM is the only nonvolatile memory that has relatively fast read/write accessibility and unlimited endurance. Future memory hierarchy is expected as in Fig. 1.22.

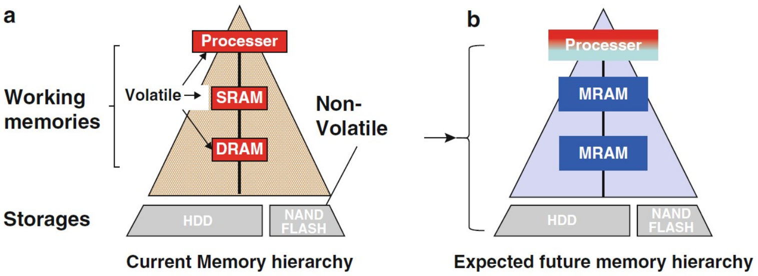

Figure 1.22: Adopted from [14]. Memory storage hierarchy used in systems. Since working memories are nonvolatile and storages are slow, a combination of working memories and storage memories are used. MRAM has a potential to replace the working memories.

However, an innovation was needed. The commercialized MRAM is not as fast as SRAM, not as dense as DRAM. Much work has been done on MTJ materials and MRAMs. In particular, spin transfer torque (STT)-writing on MTJs with perpendicular magnetization (simply expressed as P-MTJs) solves most of the problems. As a result, it is thought that we are very close to solving the above-mentioned drawbacks of the present SRAM, DRAM/NAND, and HDD memory hierarchy by designing a normally-off memory hierarchy which uses MRAMs.

MRAM is defined as a memory which uses magnetoresistance effect for reading principle regardless of writing principles. There are AMR (Anisotropic Magneto- Resistance), GMR (Giant MagnetoResistance), and TMR (Tunnel MagnetoResistance) for magnetoresistance effect. Commercialized MRAM has used TMR. Elements which have TMR are called MTJs (Magnetic Tunnel Junctions). MRAM, which uses STT writing as a writing principle, is called STT-MRAM.

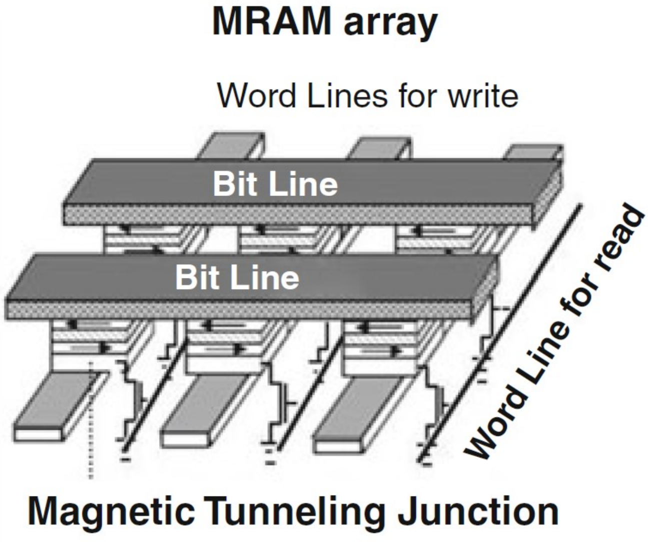

Figure 1.23: Adopted from [14]. Arrays with MTJs as storage elements.

Fig. 1.23 shows a field writing MRAM and the schematic drawing of its array. Digital data is stored in the MTJ, as magnetization directions of a storage layer, rightward or leftward in case of in-plane MTJ, and upward or downward in case of perpendicular MTJ. MRAM has nonvolatility, relatively high read and write speed, and unlimited endurance. Especially, unlimited endurance is the merit which no other nonvolatile memories have. Unlimited endurance comes from the magnetization switching mechanism which is free from atomic relocation.

Chapter 2

Spin accumulation, injection and detection

2.1 Spin current and accumulation

In metallic ferromagnets, the differences between electronic bands and scattering cross-sections of impurities for majority and minority spins at the Fermi energy cause spin-dependent mobilities. In the presence of applied electric fields and not too strong spin-flip scattering processes, a two-channel resistor model is applicable, according to which currents of two different species flow in parallel. The difference between spin-up and spin-down electric currents is called a spin-current.

In general the spin current is a tensor in the direct product of the coordinate and spin spaces

$$\hat{j}_s(\boldsymbol{r},t) = \sum_i \boldsymbol{v}_i(\boldsymbol{r},t) \otimes \boldsymbol{s}_i(\boldsymbol{r},t) + \textit{spin waves} \tag{2.1}$$

The summation is over all the electrons, $\boldsymbol{v}_i$ is a velocity of electron i, it is a vector in the coordinate space, and $\boldsymbol{s}$ is a spin of electron i, it is a vector in spin space. The last term in

Eq. (2.1) expresses the contribution to the spin current carried by spin waves. The definition of the spin current as a difference between spin-up and spin-down currents means the projection of the spin current *in the spin space* onto the direction of the magnetization. Therefore, this projection is a vector in the coordinate space.

An imbalance between the electrochemical potentials is called spin-accumulation, which is a vector. It is parallel to the magnetization if the system is described by the only magnetization direction. If the magnetization of the system is inhomogeneous, the situation can be more complicated. Spin accumulation is a non-equilibrium phenomenon, but its lifetime is usually much longer than all other relaxation time scales. Spin-flip scattering by spin-orbit interaction and magnetic impurities and disorder destroys a non-equilibrium spin-accumulation. In the bulk of metallic ferromagnets the spin accumulation vanishes beyond a spin diffusion length λ_{sF}, although spin-currents persist under the applied electric field $j_s = \frac{\hbar}{2e}(j_\uparrow - j_\downarrow) = \frac{\hbar}{2e}(\sigma_\uparrow - \sigma_\downarrow)\boldsymbol{E}$.

2.2 Spin injection across a ferromagnet/metal interface.

Let us consider a ferromagnet/paramagnet heterostructure. We will assume that the up-spin electrons are the majority in the ferromagnet. Consequently, the up-spin electrons will be the major contributors to any current injected by the ferromagnet. As a result, there will be a surplus of up-spin electrons in the paramagnet near the interface with the ferromagnet. This will cause spin accumulation in the paramagnet near the interface and an associated magnetic moment per unit volume. Under steady-state condition, the spin accumulation cannot extend into the paramagnet indefinitely since some of the up-spin electrons will eventually be converted into down-spin electrons as a result of spin-flip scattering events. In fact, far into the bulk of the paramagnet, the population of up-spin and down-spin electrons should be the same; therefore, we expect the spin accumulation to decay with distance as we move away from the interface.

We consider a ferromagnet/normal metal interface in the plane $x = 0$ and assume that the system is homogeneous in the y- and z- directions. The ferromagnet fills the half-space $(x < 0)$ and the normal metal is located in the half-space $(x > 0)$ and the electron current is assumed to flow from left to right.

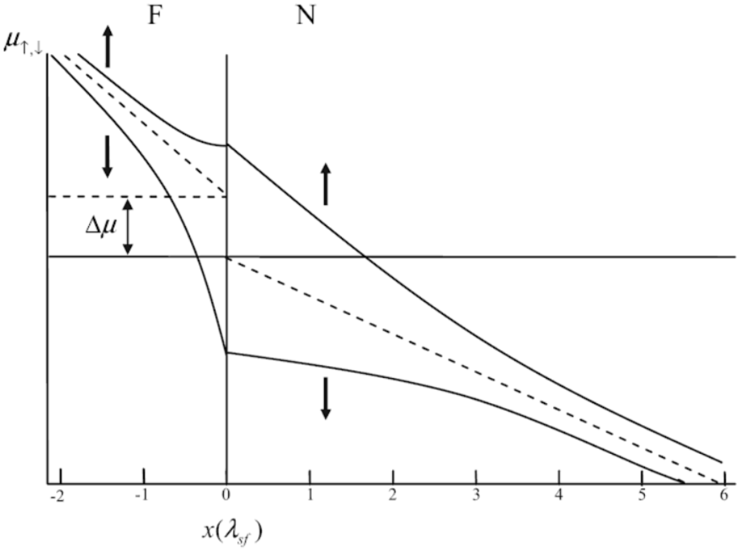

Figure 2.1: Electrochemical potentials for spin up and spin down electrons at the ferromagnet/paramagnet interface. The dashed line is the weighted chemical potential $\mu = (\mu_{\uparrow} + \mu_{\downarrow})/2$. Adopted from [15].

We assume that the spin relaxation rate is smaller than the spin-independent elastic scattering rate and the thermalization rate. In this case the distribution of spin-up and spin-down electrons can be described by the Fermi-distribution functions with spatially dependent spin-up and spin-down chemical potentials, which can be different from each other near the interface. In a steady state the total current j does not depend on x due to the current continuity.

At a distance far from the interface (exceeding the spin accumulation length in either material), the two electrochemical potentials $\mu_\uparrow$ and $\mu_\downarrow$ will converge toward each other since the up-spin and down-spin populations should be near their equilibrium values.

Furthermore, P_σ is expected to change abruptly at the interface due to the difference in conductivities of the two materials, but P_j must be continuous in the absence of spin-flip scattering mechanisms at $x = 0$. Consequently, in regions that are a few diffusion lengths away from the interface, $dP_j/dx \neq 0$ and $\mu_\uparrow \neq \mu_\downarrow$. This electrochemical potential difference is the driving force for the spin current conversion across the interface.

Further our goal is to derive the diffusion equation describing the behavior of the spin imbalance $\mu_s = \mu_\uparrow - \mu_\downarrow$. The electric current in each of the spin subbands $\sigma = \uparrow, \downarrow$ in the framework of the linear response theory in the presence of the electric field and the electron concentration gradient can be expressed as

$$j_\sigma = \sigma_\sigma E + eD_\sigma \boldsymbol{\nabla} n_\sigma, \tag{2.2}$$

the concentration in the framework of the linear response theory

$$n_\sigma(x) \approx n_{0\sigma} + N_\sigma(e\varphi + e\mu_\sigma), \tag{2.3}$$

where N_σ is the density of states, which is assumed to be approximately energy-independent in metals in the vicinity if the Fermi level. Here and below we assume $e > 0$. Taking into account that $\sigma_\sigma = e^2 N_\sigma D_\sigma$ one can obtain from Eq. (2.3)

$$\mu_\sigma = \frac{e\delta n_\sigma D_\sigma}{\sigma_\sigma} - \varphi \tag{2.4}$$

Comparing Eq. (2.2) and Eq. (2.4) we find that

$$j_\sigma = \sigma_\sigma \boldsymbol{\nabla} \mu_\sigma. \tag{2.5}$$

In the steady state the continuity equation takes the form

$$\boldsymbol{\nabla} j_\sigma = e\Big(\frac{\delta n_\sigma}{\tau_{\sigma\bar{\sigma}}} - \frac{\delta n_{\bar{\sigma}}}{\tau_{\bar{\sigma}\sigma}}\Big), \tag{2.6}$$

where $\tau_{\sigma\bar{\sigma}}$ - is the average time for flipping spin σ to $\bar{\sigma}$. From the detailed balance we obtain

$$\frac{N_\uparrow}{\tau_{\uparrow\downarrow}} = \frac{N_\downarrow}{\tau_{\downarrow\uparrow}}. \tag{2.7}$$

substituting $\delta n_\sigma = N_\sigma e(\varphi + \mu_\sigma)$ into Eq. (2.6) and taking into account the detailed balance Eq. (2.7) one can obtain:

$$\boldsymbol{\nabla} j_\sigma = e^2 \frac{N_\uparrow N_\downarrow}{N_\uparrow + N_\downarrow} \frac{\mu_\sigma - \mu_{\bar{\sigma}}}{\tau_s}, \tag{2.8}$$

where $\tau_s = \tau_{\uparrow\downarrow}\tau_{\downarrow\uparrow}/(\tau_{\uparrow\downarrow} + \tau_{\downarrow\uparrow})$.

From Eqs. (2.5) and (2.8) we obtain the following equation for the spin imbalance $\mu_s = \mu_\uparrow - \mu_\downarrow$:

$$\nabla^2 \mu_s = \mu_s / L_s^2. \tag{2.9}$$

The effective spin imbalance decay length $L_s = \sqrt{\bar{D}\tau_s}$, and $\bar{D} = (D_\uparrow\sigma_\downarrow + D_\downarrow\sigma_\uparrow)/\sigma$, where $(\sigma = \sigma_\uparrow + \sigma_\downarrow)$.

The total electric current can also be written as

$$j = j_\uparrow + j_\downarrow = \sigma(\boldsymbol{\nabla}\mu + \frac{1}{2} P_\sigma \boldsymbol{\nabla}\mu_s), \tag{2.10}$$

and, consequently the gradient of the averaged electrochemical potential is

$$\boldsymbol{\nabla}\mu = \frac{j}{\sigma} - \frac{P_\sigma}{2}\boldsymbol{\nabla}\mu_s \tag{2.11}$$

In order to find the electrochemical potentials $\mu_{\uparrow,\downarrow}$ we are to solve Eqs. (2.9) and (2.11) with the appropriate boundary conditions at the F/N interface $x = 0$.

If there is no spin flip at the interface then each of the currents j_σ conserves separately, therefore we can write

$$P_j(-0) = P_j(+0) = P_I. \tag{2.12}$$

The quantity P_I is the extremely important characteristics - the measure of the spin injection efficiency through the interface (it is called "spin injection efficiency"). If $P_I = 1$ - the current through the interface is fully spin polarized and the spin injection efficiency is absolute, and $P_I = 0$ corresponds to the completely unpolarized current.

The given subband current j_σ at the interface is connected to the jump of the chemical potential as follows:

$$j_\sigma = \Sigma_\sigma(\mu_{\sigma,N}(+0) - \mu_{\sigma,F}(-0)), \tag{2.13}$$

where Σ_σ is the conductance of the interface for spin σ.

Making use of Eqs. (2.12) and (2.13) the interface jumps of the spin imbalance and the averaged electrochemical potential can be expressed as

$$\mu_{s,N}(+0) - \mu_{s,F}(-0) = \frac{r_c j}{2}\Big(P_I - P_\Sigma\Big), \tag{2.14}$$

$$\mu_N(+0) - \mu_F(-0) = \frac{j r_c}{4}\Big(1 - P_I P_\Sigma\Big) \tag{2.15}$$

where $r_c = (\Sigma_\uparrow + \Sigma_\downarrow)/\Sigma_\uparrow\Sigma_\downarrow$ and $P_\Sigma = (\Sigma_\uparrow - \Sigma_\downarrow)/(\Sigma_\uparrow + \Sigma_\downarrow)$.

Solving Eq. (2.9) we find

$$\mu_{s,N}(x) = \mu_{s,N}(0)e^{-x/L_{s,N}}, \tag{2.16}$$

$$\mu_{s,F}(x) = \mu_{s,F}(0)e^{x/L_{s,F}} \tag{2.17}$$

and the interface values $\mu_{s,N}(0)$ and $\mu_{s,F}(0)$ can be expressed via P_I making use of

$$P_I = \frac{\frac{1}{2}\sigma\boldsymbol{\nabla}\mu_s + P_\sigma\sigma\boldsymbol{\nabla}\mu}{j}. \tag{2.18}$$

From the above equation applied separately to $x = -0$ and $x = +0$ one can find:

$$\mu_{s,N}(0) = -\frac{P_I j r_N}{2} \tag{2.19}$$

$$\mu_{s,F}(0) = \frac{j r_F}{2}(P_I - P_\sigma), \tag{2.20}$$

where $r_N = 4L_{sN}/\sigma_N$ and $r_F = 4L_{sF}/[\sigma_F(1-P_\sigma^2)]$ are the effective resistances of the N and F regions involved in the spin imbalance.

From Eqs. (2.19), (2.20) and the boundary condition (2.14) one can easily find the spin injection efficiency P_I:

$$P_I = \frac{r_F P_\sigma + r_c P_\Sigma}{r_c + r_N + r_F}. \tag{2.21}$$

This expression has an extremely simple interpretation in terms of the equivalent curcuit, which is shown in Fig. (2.2).

Now let us consider the important special cases. At first we consider a transparent junction $r_c \to 0$. In this case

$$P_I = \frac{r_F}{r_N + r_F}P_\sigma \tag{2.22}$$

the spin injection efficiency is determined by the conductivity polarization of the ferromagnet and the ratio of the ferromagnet and paramagnet resistances. For the injection into

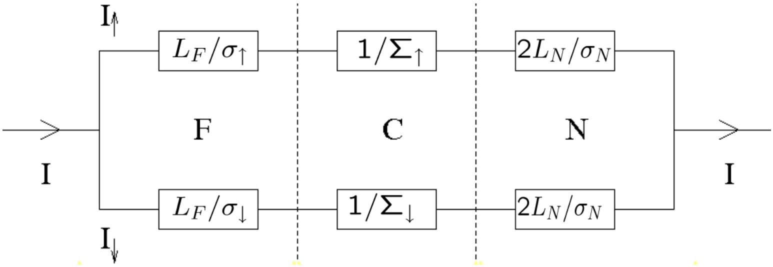

Figure 2.2: Equivalent circuit scheme describing the spin imbalance at a N/F interface. Adopted from the presentation by Y. Fabian.

a semiconductor $r_N \gg r_F$ this is again the conductivity mismatch problem. However, this problem does not appear for tunnel junctions with $r_c \gg r_N, r_F$. In this case $P_I \approx P_\Sigma$ - that is, the spin injection efficiency is determined by the interface polarization.

The schematic dependence of the spin current and spin accumulation via the F/N interface is shown in Fig. 2.3.

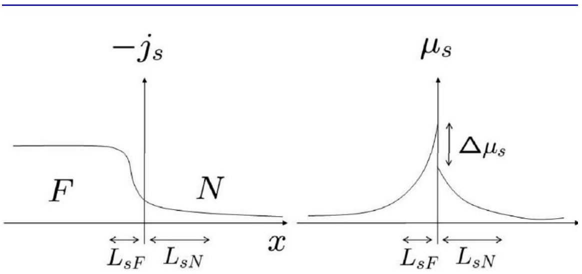

Figure 2.3: Spin current (left) and spin accumulation (right) at the F/N interface. Adopted from the presentation by Y. Fabian.

Let's now consider the spin injection efficiency into a spin valve on the basis of the diffusive theory. The sketch of the spin valve is shown in Fig. 2.4.

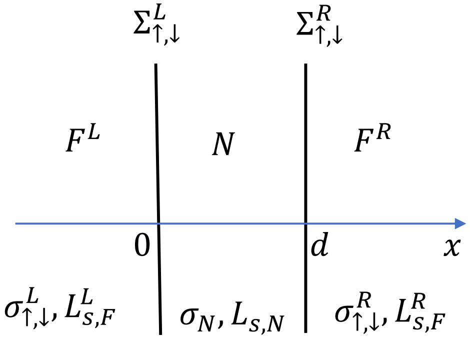

Figure 2.4: Sketch of the spin valve.

$$\begin{aligned} \mu_{sL} &= \mu_{sL}(0)e^{x/L_{F,L}} \\ \mu_{sR} &= \mu_{sR}(d)e^{(d-x)/L_{F,R}}. \end{aligned} \tag{2.23}$$

The values $\mu_{sL}(0)$ and $\mu_{sR}(0)$ can be expressed via the corresponding spin injection efficiencies $P_{L,R}$ according to Eq. (2.20)

$$\begin{aligned} \mu_{sL}(0) &= \frac{jr^L_F(P^L_I - P^L_\sigma)}{2} \\ \mu_{sR}(d) &= -\frac{jr^R_F(P^R_I - P^R_\sigma)}{2}. \end{aligned} \tag{2.24}$$

Further we assume that $d \ll L_{s,N}$. In this case the spin current $j_s = (\sigma_N/2)\nabla\mu_s$ is spatially constant in the interlayer. Therefore, $P^L_I = P^R_I = P_I$. In this approximation $\mu_{sN} = \mu_{sN}(0) + [\mu_{sN}(d) - \mu_{sN}(0)](x/d)$. Then

$$j_s = P_I j = (\sigma_N/2)[\mu_{sN}(d) - \mu_{sN}(0)]/d. \tag{2.25}$$

Now from Eq. (2.14) we obtain

$$\begin{aligned} \mu_{sN}(0) - \frac{jr^L_F(P_I - P^L_\sigma)}{2} &= \frac{jr^L_c}{2}(P_I - P^L_\Sigma) \\ -\frac{jr^R_F(P_I - P^R_\sigma)}{2} - \mu_{sN}(d) &= \frac{jr^R_c}{2}(P_I - P^R_\Sigma). \end{aligned} \tag{2.26}$$

Taking into account Eq. (2.25) from Eq. (2.26) we obtain

$$P_I = \frac{P_\sigma^L r_F^L + P_\Sigma^L r_c^L + P_\sigma^R r_F^R + P_\Sigma^R r_c^R}{r_{LNR}},$$
$$r_{LNR} = r_c^L + r_c^R + r_F^L + r_F^R + \frac{4d}{\sigma_N}. \tag{2.27}$$

The above expression for P_I can be rewritten in a convenient form using the spin injection efficiencies for two *disconnected* N/F interfaces $\gamma_{L,R}$, which are expressed by Eq. (2.21)

$$P_I = \frac{\gamma_L(r_F^L + r_c^L + r_N) + \gamma_R(r_F^R + r_c^R + r_N)}{r_{LNR}}. \tag{2.28}$$

In case of identical ferromagnets in parallel configuration $\gamma_L = \gamma_R = \gamma$ and

$$P_I^P = \frac{2\gamma_L(r_F + r_c + r_N)}{r_{LNR}}, \tag{2.29}$$

while in case of two identical ferromagnets in antiparallel configuration $\gamma_L = -\gamma_R$

$$P_I^{AP} = 0. \tag{2.30}$$

2.3 Resistance of the F/N interface.

From the local charge neutrality condition $\delta n_\uparrow + \delta n_\downarrow = 0$ it follows that

$$\varphi = -\mu - P_N \frac{\mu_s}{2}, \tag{2.31}$$

where $P_N = (N_\uparrow - N_\downarrow)/(N_\uparrow + N_\downarrow)$ is the density of states polarization. Then taking into account that $P_N = 0$ in the paramagnet and making use of the boundary conditions (2.15) we obtain

$$\varphi_N(0) - \varphi_F(0) = -\frac{jr_c}{4}\Big(1 - P_I P_\Sigma\Big) + \frac{\mu_{s,F}(0)}{2} P_{N,F}. \tag{2.32}$$

Integrating Eq. (2.11) over the ferromagnet and over the paramagnet separately we obtain

$$\mu_N(x) = \frac{j}{\sigma_N}x + \mu_N(0), \tag{2.33}$$

$$\mu_F(x) = \frac{j}{\sigma_F}x - \frac{P_\sigma}{2L_{s,F}}\mu_{s,F}(x) + C_F. \tag{2.34}$$

Deep in the ferromagnet far from the F/N interface $\mu_s = 0$ and $\varphi = -\mu$. Therefore, the voltage between the ferromagnet and the normal metal can be found as

$$\varphi_N(l_N) - \varphi_F(-l_F) = -\frac{l_N}{\sigma_N}j - \frac{l_F}{\sigma_F}j - \mu_N(0) + C_F. \tag{2.35}$$

Subtracting the Ohmic part of the resistance we obtain

$$R = \frac{\mu_N(0) - C_F}{j} = \frac{1}{\Sigma_\uparrow + \Sigma_\downarrow} + \frac{r_N(r_F P_\sigma^2 + r_c P_\Sigma^2) + r_c r_F (P_\sigma - P_\Sigma)^2}{4(r_c + r_N + r_F)}. \tag{2.36}$$

It is that the spin injection always enhances the resistance of a F/N junction. Physically it can be understood from Fig. (2.5).

2.4 Detection of the nonequilibrium spin accumulation.

Now let us consider different methods of detection of the spin accumulation. First of all, any kind of non-equilibrium in an electronic system results in an electro-motive force. This general statement is completely applicable to spin non-equilibrium. A valve spin-e.m.f. arises at the spin selective contacts. Measuring the spin-e.m.f. in metals has been used for detecting

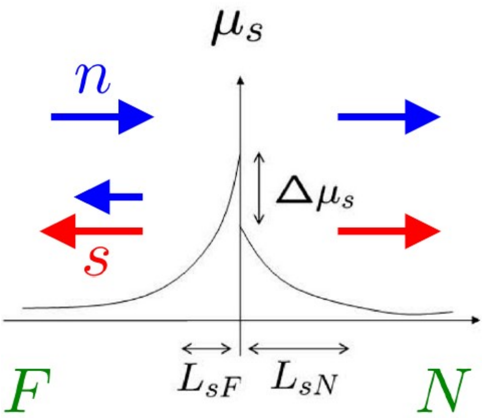

Figure 2.5: Adopted from the presentation by Yaroslav Fabian. Why the additional resistance of N/F interface is positive? It is seen that the "spin potential" rises upon approaching the interface irrespective of the sign of $\Delta\mu_s$. Therefore, the part of incoming spin is reflected from the interface and, therefore, the part of electrons is reflected also because it is the electrons that carry the spin. As a result, the part of the electric charge is reflected, what increases the resistance.

the electrical spin injection. Now we consider the effect of the electromotive force.

For an open circuit with $j = 0$ one can find from Eq. (2.32) (accounting for $P_I j = j_\uparrow - j_\downarrow = j_s(0)$)

$$\varphi_N(0) - \varphi_F(0) = \frac{r_c j_s(0) P_\Sigma}{4} + \frac{\mu_{s,F}(0)}{2} P_{N,F}. \qquad (2.37)$$

Now we assume that the spin imbalance $\mu_N(\infty)$ is induced in the paramagnet far from the F/N interface by an external source (see Fig. 2.6). Our goal is to measure the value of this imbalance by means of the voltage measurements.

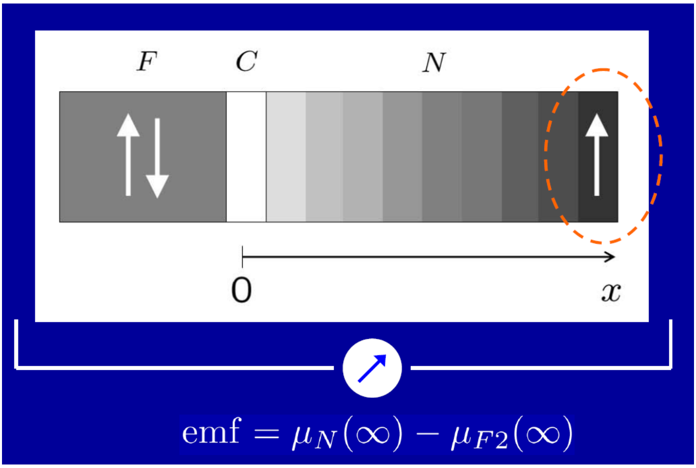

Figure 2.6: Voltage induced at the F/N interface due to the spin accumulation. Adopted from the presentation by Y. Fabian.

In this case the profile of the spin imbalance in the paramagnet takes the form

$$\mu_{s,N}(x) = \mu_{s,N}(\infty) + \Big[\mu_{s,N}(0) - \mu_{s,N}(\infty)\Big] e^{-x/L_{s,N}} \tag{2.38}$$

From Eqs. (2.19), (2.20) it can be deduced that

$$j_s(0) = \frac{2\mu_{s,F}(0)}{r_F} = -\frac{2(\mu_{s,N}(0) - \mu_{s,N}(\infty))}{r_N}. \tag{2.39}$$

Together with the boundary condition (2.14), which for the open circuit takes the form $\mu_{s,N}(0) - \mu_{s,F}(0) = r_c j_s(0)/2$ the above equation allows for obtaining

$$j_s(0) = \frac{2\mu_{s,N}(\infty)}{r_c + r_F + r_N} \tag{2.40}$$

$$\mu_{s,N}(0) = \mu_{s,N}(\infty)\frac{r_c + r_F}{r_c + r_F + r_N} \tag{2.41}$$

$$\mu_{s,F}(0) = \mu_{s,N}(\infty)\frac{r_F}{r_c + r_F + r_N} \tag{2.42}$$

Integrating Eq. (2.11) over the ferromagnet and over the paramagnet separately and making use of Eq. (2.37) finally we obtain:

$$\varphi_N(l_N) - \varphi_F(-l_F) = \frac{r_c P_\Sigma + r_F P_\sigma}{2(r_c + r_N + r_F)} \mu_{s,N}(l_N) = \frac{P_I}{2} \mu_{s,N}(l_N). \quad (2.43)$$

2.4.1 Nonlocal spin detection.

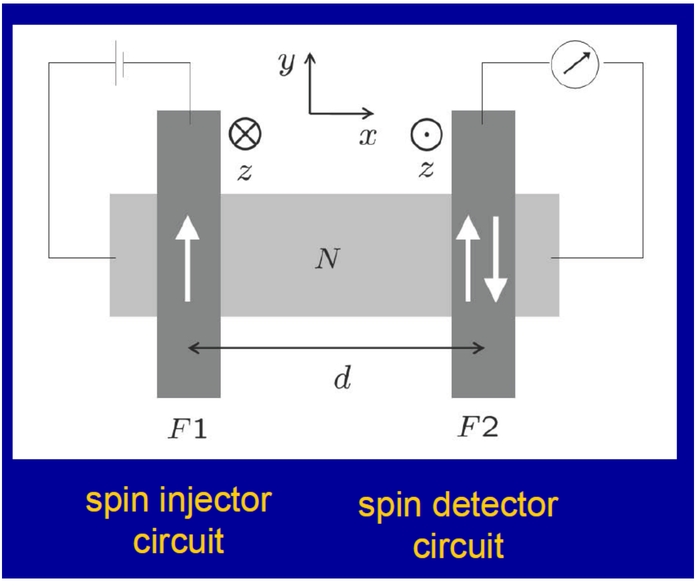

Figure 2.7: Sketch of the typical nonlocal detection scheme. Adopted from the presentation by Y. Fabian.

The classical scheme of a nonlocal spin accumulation measurement is presented in Fig. 2.7. There are two different electric circuits in the setup. The electric current is injected from the ferromagnet F1 into the normal wire and travels via the left circuit. There is no electric current between the injector

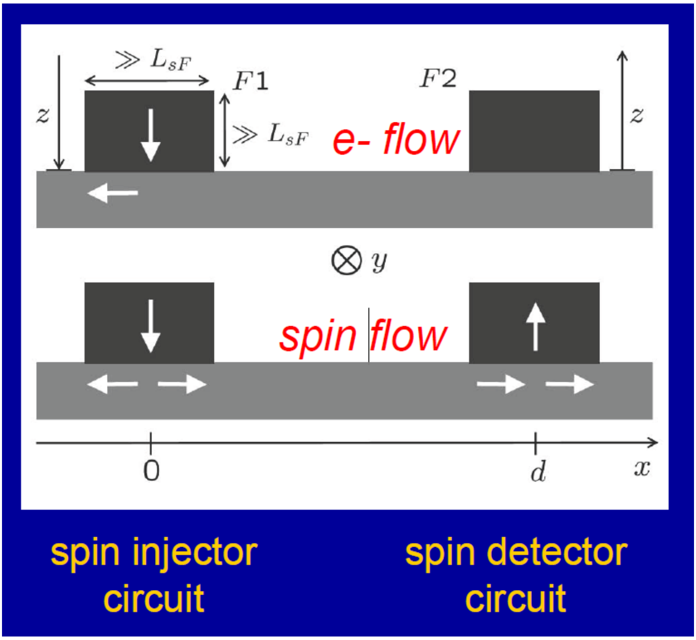

Figure 2.8: Electrical current and spin current flows in the nonlocal scheme. Adopted from the presentation by Y. Fabian.

and detector ferromagnets, but the spin imbalance is created symmetrically around the interface between F1 and the wire (see Fig. 2.8) and, in particular, spreads to the detector point. If the detector circuit is open, the electric voltage is induced between F2 and the wire according to the theory described above.

The interfaces between the detector, injector and the wire are assumed to be low-transparent $r_c \gg r_N, r_F$. In this case according to Eq. (2.41) $\mu_{s,N}(\infty) \approx \mu_{s,N}(0)$, that is the open detector circuit practically does not influence the distribution of the spin imbalance in the wire. In this case the voltage (2.43) measured by the detector is

$$\varphi_N(\infty) - \varphi_F(-\infty) \approx \frac{P_D}{2}\mu_{s,N}(x=d), \qquad (2.44)$$

where $P_D \approx P_{\Sigma,D}$ is the spin injection efficiency of the detector and $\mu_{s,N}(x=d) \approx -\frac{P_I}{2} j r_N e^{-d/L_{s,N}} \approx -(1/2) P_{\Sigma,I} j r_N e^{-d/L_{s,N}}$ is the spin imbalance induced by the injector at the detector point. Finally we obtain the following value of the *nonlocal resistance*, that is the ratio of the voltage in the detector circuit to the current in the injector circuit:

$$R_{nl} = \frac{\varphi_N(\infty) - \varphi_F(-\infty)}{j} \approx \frac{1}{4} P_{\Sigma,I} P_{\Sigma,D} r_N e^{-d/L_{s,N}}. \quad (2.45)$$

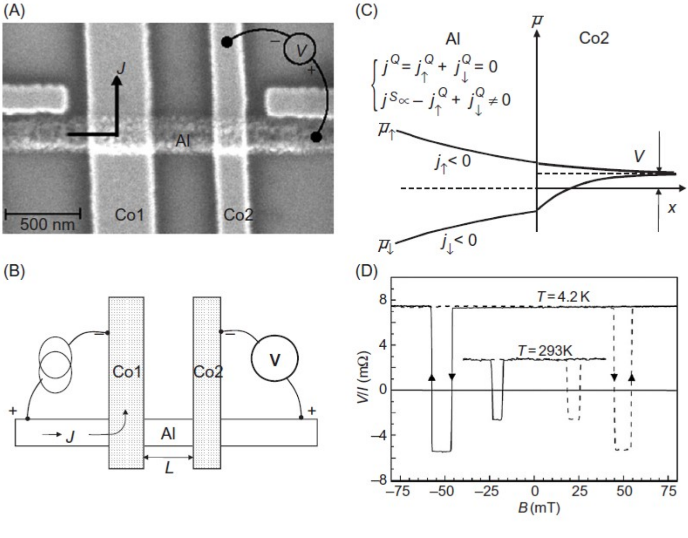

Figure 2.9: Experimental results on nonlocal spin imbalance detection [16].

Experimental results on nonlocal spin imbalance detection are presented in Fig. 2.9. In Fig. 2.9(D) it is seen that the nonlocal resistance is always positive except for narrow regions of the magnetic field, where the ferromagnets are in antiparallel configuration.

2.4.2 Optical detection of spin accumulation.

Optical experiments allow for measurements of $n_\uparrow - n_\downarrow$. From Eqs. (2.3) and Eq. (2.31) it can be deduced that

$$n_\uparrow - n_\downarrow = N_\uparrow(e\varphi + e\mu_\uparrow) - N_\downarrow(e\varphi + e\mu_\downarrow) = \frac{2eN_\uparrow N_\downarrow}{N}\mu_s(x). \quad (2.46)$$

Therefore, optical measuments also provide a way of spin accumulation detection.

Chapter 3

Spin field-effect transistors

Our presentation in this chapter closely follows [14, 15]. The fundamental device at the heart of all digital computing hardware is the binary switch that has two well-separated stable states. They store and encode the binary bits 0 and 1. When the switch is implemented with metal-oxide-semiconductor field-effect transistors (MOSFET), the two states are the high-conductance (on) and low-conductance (off) states of the device. The MOSFET is turned on by moving charge into the channel and turned off by moving charge out. Switching is therefore associated with motion of charges. In all charge-based switches, the switching action invariably requires charge motion. This is because charge is a scalar quantity. Therefore, the two states must be distinguished by a difference in the magnitudes of the charge in the device. Switching will require changing the magnitude by an amount ΔQ, in a time Δt, leading to a current flow of magnitude $I = \Delta Q/\Delta t$. This current causes an unavoidable energy dissipation of $I^2 R\Delta t = \Delta Q^2 R/\Delta t$, where R is the resistance in the path of the current. One can reduce this dissipation by increasing Δt (switching slowly) or by decreasing ΔQ, but neither is desirable since the former makes the switch slow and error prone, while the latter reduces noise immunity since it decreases the logic-level separation by bringing the two states closer together.

The above shortcoming of charge-based devices has motivated the search for alternate state variables, such as electron spin, to encode binary bits. For example, a single electron's spin polarization in a magnetic field has two stable states that are parallel and antiparallel to the field. These two mutually antiparallel polarizations can encode the bits 0 and 1. Switching between them merely requires flipping the spin, without moving the electron in space and causing current flow. This eliminates the $I^2 R\Delta t$ dissipation, but does not eliminate dissipation altogether since the two spin states are nondegenerate and separated in energy by the Zeeman splitting $g\mu_B B$. Therefore, even if a single spin is used as a binary switch, the minimum energy dissipation would have been $g\mu_B B$ per bit flip event. In fact, the minimum energy dissipation for any single entity (single spin, single charge, single anything) will be always $k_B T ln(1/p)$, where p is the probability of random switching between the two states as long as the switch is in thermodynamic equilibrium with its surrounding at temperature T. From that perspective, it should make no difference whether single charge or single spin is used as the vehicle to encode logic bits. However, what does make a difference is that no single entity is ever stable enough in a noisy environment to encode logic bits reliably. Therefore, an ensemble of entities (many spins, many single electron charges) is required to encode a logic bit in a robust fashion. In that case, spin has a very important advantage over charge. The minimum energy dissipated to switch an ensemble of information carriers (spins, charges, etc.) is $N k_B T ln(1/p)$, where N is the number of degrees of freedom that the ensemble possesses. In the case of charges, $N = N_e$ is the number of charges in the ensemble.

This happens because the different charges act independently. However, in the case of spin, $N \sim 1$, since exchange interaction between spins makes all of them act in unison, that is the magnetism is a *macroscopic* quantum state. In a single-domain magnet, effectively $N = 1$. Therefore, the minimum ratio of the dissipations incurred in switching a spin ensemble and a charge ensemble is $1/N_e$ which gives spin a significant advantage over charge when $N_e > 1$.

In a spin field-effect transistor (SPINFET), the current flowing between two terminals (the source and the drain) is modulated by applying an electrostatic potential to the third terminal (the gate), as in a MOSFET. The difference is that the gate potential does not modulate the charge, or number of charge carriers, in the channel, but instead modulates the spin polarization of the carriers. If the source and drain contacts are efficient spin filters, then modulation of the spin polarization can modulate the current flowing between the source and drain, thus realizing transistor action. The gate potential can therefore turn the transistor on or off, but without changing the amount of charge in the channel. In other words, $\Delta Q = 0$, which should make the energy dissipation $\Delta Q^2 R/\Delta t$ vanish. That it does, but there is additional energy cost associated with modulating spin polarization, and that cost may or may not exceed $\Delta Q^2 R/\Delta t$. If it does exceed, then the SPINFET is actually less energy efficient than the MOSFET. The reality is that spin transistors are generally no more energy efficient than MOSFETs, and they are not faster either. In fact, they may have major shortcomings that make them less desirable than MOSFETs as binary switches.

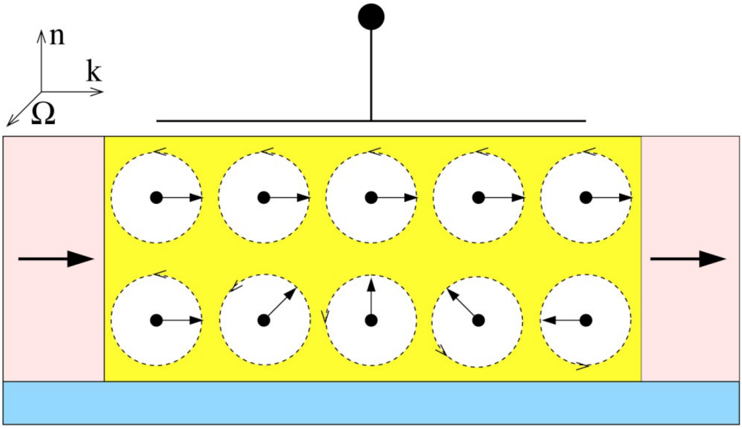

Figure 3.1: The Datta-Das SPINFET. Adopted from [18].

3.1 The Datta-Das SPINFET.

In many ways, the first proposal for a Spin Field Effect Transistor (SPINFET) [17] now called the Datta-Das transistor after the two proponents of this device was a watershed event in the field of spintronics. It was the first time anyone proposed using the spin degree of freedom of a charge carrier to realize an active device which can process information in a tractable way. The SPIN FET device proposed in [17] looks exactly like a conventional metal-insulator semiconductor field effect transistor (MISFET) except that the source and drain contacts are ferromagnetic. Fig. 3.1 shows a schematic of this device. For simplicity we will assume that the channel is strictly one dimensional (a quantum wire) whose width is smaller than the Fermi wavelength of carriers in the channel, so that only the lowest subband is occupied by electrons. Both source and drain contacts are magnetized in such a way that their magnetic moments are parallel to each other and point along the direction of current flow ($+x$-axis). When a potential difference is imposed between these contacts, the ferromagnetic source injects carriers into the channel with their spins polarized in the $+x$-direction. These are the majority spins in the ferromagnetic source contact. We will now make the following idealized assumptions:

1. The ferromagnetic source injects only the majority spins and no minority spins at all. Moreover, there should be no loss of spin polarization at the interface due to spin flip scattering. In other words, the spin injection efficiency at the source end, defined as

$$\zeta = \frac{I_{\uparrow} - I_{\downarrow}}{I_{\uparrow} + I_{\downarrow}} \tag{3.1}$$

is unity, $\zeta = 1$.

2. We will also assume that the drain is an idealized spin filtering ferromagnet which only transmits the majority spins and completely blocks the minority spins.

3. When the gate voltage is zero, there are no stray symmetry breaking electric fields in the (y, z)-plane that induce any Rashba interaction. Note that the source-to-drain electric field, which drives the current in the channel, is in the x-direction which is the same direction as the carrier velocity; hence, it does not cause a Rashba spin-orbit interaction. Only when the gate voltage is non-zero there can be a Rashba interaction in the channel due to the electric field caused by the gate voltage. There is also no Dresselhaus spin-orbit interaction and no stray magnetic fields in the channel (we ignore the magnetic field caused by the ferromagnetic contacts).

4. There is no spin relaxation in the channel. There can be momentum and energy relaxing collisions in the channel transport need not be ballistic but these scatterings must not relax spin. This is a realistic assumption since we will know that in a strictly one dimensional channel with a single transverse subband occupied, there is no Dyakonov-Perel spin relaxation in space. There is also no Elliott-Yafet spin relaxation

if there is no magnetic field in the channel. This is because if the only spin-orbit interaction is the Rashba interaction, then each spin-split band has a fixed (wavevector-independent) spin quantization axis. In that case, intraband scattering does not change spin polarization and interband scattering (due to a non-magnetic scatterer) is forbidden because the spin eigenstates in two different bands are orthogonal. Therefore, there is no Elliott-Yafet relaxation.

5. We will ignore effects due to multiple reflections of an electron between the source and drain contacts.

Under these assumptions right after injection from the source, all electrons in the channel of the Datta-Das transistor will have their spins polarized along the direction of current flow, i.e., the $+x$-direction since the source is magnetized in the $+x$-direction and injects spin with 100% efficiency. When the gate voltage is turned on, it causes a transverse electric field in the y-direction, which causes Rashba spin-orbit interaction in the channel. This interaction will act as an effective magnetic field in the z direction which will be given by

$$\boldsymbol{B}_R = \kappa E_y v_x \hat{z}, \tag{3.2}$$

where κ is the material-dependent constant E_y is the y-directed gate electric field and v_x is the x-directed velocity of carriers in the channel.

The pseudo-magnetic field $\boldsymbol{B}_R$ is directed along the z-axis. It will cause the electrons entering the channel with x-polarized spins to execute Larmor precession in the (x, y)-plane as they travel toward the drain. The equation of motion for a free magnetic dipole can be obtained from Newtons second law for rotation,

$$\frac{\partial \boldsymbol{J}}{\partial t} = \boldsymbol{\tau} \tag{3.3}$$

where $\boldsymbol{J}$ is the angular momentum and $\boldsymbol{\tau}$ is the torque. Substituting $\boldsymbol{\mu} = -\frac{g\mu_B}{\hbar}\boldsymbol{J}$ and $\tau = \boldsymbol{\mu} \times \boldsymbol{B}$ obtain

$$\frac{\partial \boldsymbol{\mu}}{\partial t} = -\frac{g\mu_B}{\hbar}\boldsymbol{\mu} \times \boldsymbol{B}. \tag{3.4}$$

The angular frequency of this precession is the Larmor frequency

$$\Omega = \frac{d\phi}{dt} = \frac{g\mu_B B_R}{\hbar} = \frac{g\mu_B \kappa}{\hbar} E_y v_x. \tag{3.5}$$

The spatial rate of spin precession is given by

$$\frac{d\phi}{dx} = \frac{d\phi}{dt}\frac{1}{v_x} = \frac{g\mu_B \kappa}{\hbar} E_y. \tag{3.6}$$

It is important to note from the above equation that the spatial rate of spin precession depends on the gate voltage but is independent of the carrier velocity along the channel. This means that the spin of every electron, regardless of its velocity (and hence kinetic energy), precesses by exactly the same angle as it travels from source to drain. This angle is given by

$$\Phi = \frac{g\mu_B \kappa}{\hbar} E_y L. \tag{3.7}$$

An electron may suffer numerous momentum and energy randomizing collisions and arrive at the drain with arbitrary velocity, but it does not matter, if the collisions are spin-independent. When any electron arrives at the drain, with whatever velocity and whatever scattering history, its spin has precessed by exactly the same angle as any other electron in traversing the channel since is independent of the electrons velocity. The angle Φ depends only on E_y, or the gate voltage, which is the same for every electron. If the gate voltage is of such magnitude that $\Phi = (2n + 1)\pi$, then every electron arriving at the drain will have its spin polarized anti-parallel to the drains magnetization. These electrons are completely blocked by the drain since the drain transmits only those electrons whose spins are polarized in the $+x$-direction. Therefore, the source-to-drain current falls to zero. Without a gate voltage, the spins do not precess so that every electron arriving at the drain has its spin polarized parallel to the drains magnetization. These electrons are all transmitted by the drain so that the source-to-drain current is non-zero. Thus, when the gate voltage is zero, the conductance is maximum and when the gate voltage is V_{off}, corresponding to $\Phi = (2n+1)\pi$, the conductance is minimum and ideally zero. Therefore, the gate voltage changes the conductance between a maximum and minimum value using spin precession and realizes basic switching transistor action. Note that the switching action has been explained by invoking a classical particle picture (Larmor precession of a particle about a pseudo magnetic field), and no wave interference was necesssary. This underscores the fact that the switch is a purely classical device.

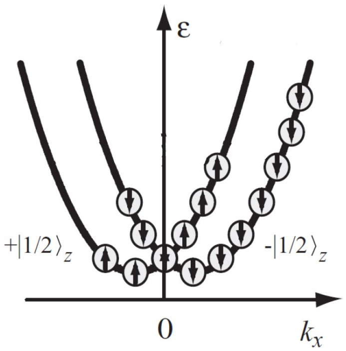

Figure 3.2: Rashba spin-split 1D electron subbands.

The wave picture, however, becomes necessary if we want to find the conductance of the device at any arbitrary gate voltage. The energy dispersion relations in the one-dimensional channel of the Datta Das transistor (with no Dresselhaus interaction and no channel magnetic field) are two horizontally displaced parabolas. An electron with energy E has wavevectors k_1 and k_2 in the two spin resolved bands. The corresponding eigenspinors are the $+z$ and $-z$-polarized states $(1\ \ 0)^T$ and $(0\ \ 1)^T$. The source contact is magnetized in the $+x$-direction and hence injects only $+x$-polarized spins in the channel. Consider an electron injected with energy E. Its spin state at the source end can be written as a superposition of the channel eigenspinors:

$$\Psi_{source} = \frac{1}{\sqrt{2}}\begin{pmatrix} 1 \\ 1 \end{pmatrix} = \frac{1}{\sqrt{2}}\begin{pmatrix} 1 \\ 0 \end{pmatrix} + \frac{1}{\sqrt{2}}\begin{pmatrix} 0 \\ 1 \end{pmatrix}. \tag{3.8}$$

At the drain end the spin state of the electron is

$$\Psi_{drain} = \frac{1}{\sqrt{2}}\begin{pmatrix} 1 \\ 0 \end{pmatrix} e^{ik_1 L} + \frac{1}{\sqrt{2}}\begin{pmatrix} 0 \\ 1 \end{pmatrix} e^{ik_2 L}. \tag{3.9}$$

The eigenspinor in the drain contact, which is also magnetized in the $+x$ direction, is $(1/\sqrt{2})(1\ \ 1)^T$. Therefore, if we neglect multiple reflections within the channel, then the transmission amplitude into the drain is given by the projection of Ψ_{drain} on the eigenspinor in the drain contact:

$$t(E) = \frac{1}{2}(1\ \ 1)\begin{pmatrix} e^{ik_1 L} \\ e^{ik_2 L} \end{pmatrix} = \frac{1}{2}\Big(e^{ik_1 L} + e^{ik_2 L}\Big), \tag{3.10}$$

and

$$T(E) = |t(E)|^2 = \frac{1}{4}\Big|1 + e^{i(k_1 - k_2)L}\Big|^2 = \cos^2\frac{\Phi}{2} \tag{3.11}$$

since $k_2 - k_1 = 2m^*\alpha_R/\hbar = g\mu_B\kappa E_y/\hbar$.

Therefore, we can write the channel conductance as

$$G = G_0 \cos^2\frac{\Phi}{2}. \tag{3.12}$$

Oscillatory transfer characteristics have unusual applications. Suppose we apply a sinusoidal voltage of frequency f to the gate and the amplitude of this voltage is nV_{off}. Then the source-to-drain current will oscillate with a frequency nf. Thus, we have realized a single stage frequency multiplier.

It should be obvious that, in this device, although current modulation is achieved through spin precession, spin itself plays no direct role in information handling. Information is still encoded in charge which carries the current from the source to the drain. The transistor is still switched between the on and off states by changing the current or the amount of charge transmitting through the device. The role of spin is only to provide an alternate means of changing the current.

Now let us discuss shortcomings of the SPINFET. The generic problem, which affects all the spin transistors that require spin injection and detection is not 100% spin injection efficiency. If we introduce spin injection efficiency of the source $\zeta_S = (I_\uparrow - I_\downarrow)/(I_\uparrow + I_\downarrow)$ and the "spin detection efficiency of the drain" $\zeta_D = (T_\uparrow - T_\downarrow)/(T_\uparrow + T_\downarrow)$, where $T_{\uparrow,\downarrow}$ are transparencies of the channel/drain interface for spin up (down) quasiparticles, then the ratio of on-to-off conductance is

$$\frac{G_{on}}{G_{off}} = \frac{1 + \zeta_S \zeta_D}{1 - \zeta_S \zeta_D}. \tag{3.13}$$

In order to achieve a conductance on-off ratio of 10^5, required of modern transistors, $\zeta_S = \zeta_D = 99.9995\%$, which is a very high order. The primary impediment to realization of usable SPINFETs at this time is inadequate spin injection efficiency.

The other problems are (i) small values of the Rashba constant leading to the necessity to make very long channels (of the order of $1 \mu m$) or to apply a very high gate voltages as compared to the usual semiconductor transistors and (ii) channel stray fields from the source and drain ferromagnets, which make Φ dependent on the quasiparticle velocity greatly reducing G_{on}/G_{off}. The first of these problems leads to losing the energy efficiency with respect to MOSFET. Indeed, the SPINFET is switched without changing the carrier concentration in the channel. Therefore, it might appear that no current needs to flow to switch the transistor, thus eliminating the $I^2R\Delta t$ loss. Unfortunately, this is not true since switching is still accomplished with a gate voltage and some current flow is needed to charge up the gate (a capacitor) to the required voltage. The energy dissipated to charge up the gate to a voltage V_G is still $CV_G^2/2$ if the gate is charged abruptly or non-adiabatically. Thus, in terms of gate dissipation, the SPINFET is no different from the MOSFET where the gate dissipation is again the same. It does not matter what the gate voltage does whether it changes the carrier concentration or the spin polarization of the carriers. Therefore, the SPINFET provides no special advantage. If any advantage were to accrue, it would be solely due to the fact that the gate voltage required to switch a SPINFET is smaller than that required to switch a MOSFET. For nanoscale transistors it is not the case. In fact, the SPINFET normally will require a much larger gate voltage than a comparable MOSFET and hence is less energy efficient, as long as the channel length is shorter than $\sim 1\mu m$. The problem is that the gate voltage in a spin transistor changes the spin polarization of carriers by affecting spin-orbit interaction. The gate voltage dependence of spin-orbit interaction in the conduction band of most semiconductors is very weak, so that a very large gate voltage will be required to induce sufficient change in the spin polarization to turn a SPINFET from on to off, or vice versa.

The problem of stray fields is connected to the so-called spin Hanle effect. The spin Hanle effect is based on precession of a spin about a magnetic field. Consider a one-dimensional spin valve structure shown in Fig. 3.3 consisting of two ferromagnetic contacts magnetized in the direction of current flow. The left contact is a spin-polarizer that injects electrons with

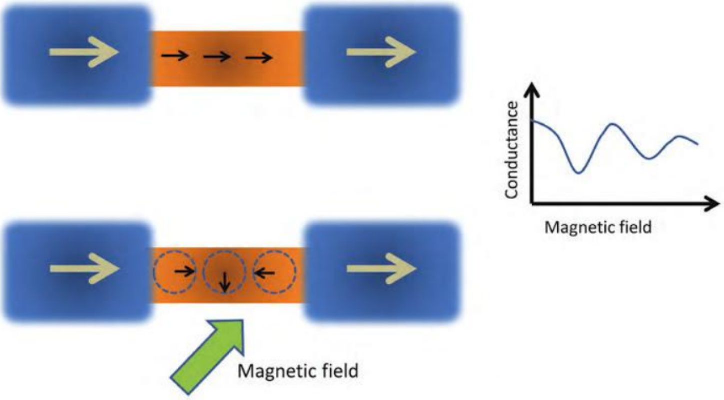

Figure 3.3: The spin Hanle effect. The magnetic field is applied perpendicular to the figure plane. Adopted from [15].

spins polarized in the direction of current flow into the spacer layer and the right contact is a spin analyzer that selectively transmits electrons whose spins are aligned along the direction of its own magnetization. We will assume that there is no spin relaxation in the spacer layer. In that case, the conductance of the structure will vary as $\cos^2(\theta/2)$ where θ is the angle between the spin polarization of the electrons arriving at the right contact and the magnetization of the right contact. In the absence of any magnetic field, spin-orbit interaction, and spin relaxing events, the injected spins will arrive intact at the right contact. Since both contacts are magnetized in the same direction, $\theta = 0$ in this case and the conductance will be maximum. Next, imagine that a magnetic field is applied perpendicular to the direction of current flow (and hence perpendicular to the injected spin polarization). The spins will then execute Larmor precession about this magnetic field as they traverse the spacer layer. The angle by which they will precess will determine the angle θ:

$$\theta = \Omega \frac{L}{v} = \frac{g\mu_B B}{\hbar} \frac{L}{v}, \tag{3.14}$$

where Ω is the spin precession frequency, $\boldsymbol{B}$ is the magnetic flux density, L is the spacer regions length, and v is the electron velocity. If we compare the above equation to Eq. (3.7), we see that in contrast to the spin-orbit induced spin precession angle, the real magnetic field induced precession angle depends on the electron velocity. Clearly, the conductance, which is proportional to $\cos^2(\theta/2)$, will oscillate as B is varied, and these are called Hanle oscillations. However, because θ depends on v, different electrons having different velocities precess by different angles. Ensemble averging over the electron velocities will make the conductance oscillation amplitude decay with increasing magnetic field strength. This effect is parasitic to the SPINFET because in the presence of the spin precession induced by the stray fields electrons with different velocities will require different gate voltages to reverse their spins on the distance between the source and the drain.

Chapter 4

Spin torques and magnetization dynamics.

Here we are going to study the dynamics of macroscopic magnetization in ferromagnets, which can be caused by applying of an external magnetic field or an external electric current.

4.1 Landau-Lifshitz-Gilbert equation.

We separately treat the conduction part and magnetization part in a ferromagnetic metal. The former is assumed to be conducting s-electrons and the latter is localized d-spins, which are ferromagnetically coupled to each other. For the conduction electrons, we will consider in a later section the case of current-driven magnetization dynamics. In this section, we focus on the magnetization part. The magnetization vector field $\boldsymbol{M}$ is the magnetic moment of d-electrons per unit volume and is defined by

$$\boldsymbol{M} = -\gamma \frac{\hbar \boldsymbol{S}}{a^3} = M_s \boldsymbol{m}, \tag{4.1}$$

where $\gamma > 0$ is the gyromagnetic ratio, S is the magnitude of spin, a is a lattice constant. Note that the direction of magnetization vector is opposite to the local spin $\boldsymbol{S}$. In the following we use the unit vector $\boldsymbol{m} = (\sin\theta\cos\phi, \sin\sin\phi, \cos\theta)$ directed along the magnetization and the amplitude of the magnetization density is denoted by M_s.

Now our goal is to investigate the magnetization dynamics in a ferromagnet under the action of the applied magnetic field. The equation of motion for a free magnetic dipole can be obtained from Newtons second law for rotation,

$$\frac{\partial \boldsymbol{J}}{\partial t} = \boldsymbol{\tau} \tag{4.2}$$

where $\boldsymbol{J}$ is the angular momentum and $\boldsymbol{\tau}$ is the torque. Substituting $\boldsymbol{\mu} = -\gamma \boldsymbol{J}$ and $\tau = \boldsymbol{\mu} \times \boldsymbol{B}$ obtain

$$\frac{\partial \boldsymbol{\mu}}{\partial t} = -\gamma \boldsymbol{\mu} \times \boldsymbol{B}. \tag{4.3}$$

The magnetic dipole precesses about the magnetic field. If any form of dissipation is present, the free dipole will eventually align with the applied magnetic field to minimize its energy.

Magnetic dipoles in solids are not free, but are constrained by, for instance, exchange interactions, magnetocrystalline anisotropies, and dipole- dipole interactions. However, just as the free dipole, magnetic dipoles in a solid $\boldsymbol{M} = \boldsymbol{\mu}/V$ will minimize their energy in equilibrium. Now let us briefly discuss different contributions to the magnetic energy of a ferromagnet.

4.1.1 Exchange energy.

We will use the classical Heisenberg hamiltonian to derive the expression for the exchange energy in terms of continuous magnetization density $\boldsymbol{M}$

$$E_{i,j} = -J \boldsymbol{S}_i \boldsymbol{S}_j, \tag{4.4}$$

where J is the exchange integral and $\boldsymbol{S}_i$ and $\boldsymbol{S}_j$ are two neighboring classical spins. With the magnitude of the spins S and unit vectors $\boldsymbol{n}_i = \boldsymbol{S}_i/S$ and $\boldsymbol{n}_j = \boldsymbol{S}_j/S$ it can be written as

$$E_{ij} = -JS^2\boldsymbol{n}_i\boldsymbol{n}_j = -JS^2[1 - \frac{1}{2}(\boldsymbol{n}_i - \boldsymbol{n}_j)^2]. \tag{4.5}$$

The exchange energy of a ferromagnet is calculated by summing up

$$E_{ex} = -\sum_{ij} J_{ij}S^2[1 - \frac{1}{2}(\boldsymbol{n}_i - \boldsymbol{n}_j)^2]. \tag{4.6}$$

Further this expression has to be adapted to the continuous magnetization field $\boldsymbol{m}$:

$$E_{ex} = -\sum_{ij} J_{ij}S^2\boldsymbol{n}_i\boldsymbol{n}_j = -\int d^3\boldsymbol{r}\sum_i A_i\boldsymbol{m}(\boldsymbol{r})\boldsymbol{m}(\boldsymbol{r} + \Delta\boldsymbol{r}_i), \tag{4.7}$$

where A_i and $\Delta\boldsymbol{r}_i$ depend on the particular crystal structure. Substituting $\boldsymbol{m}(\boldsymbol{r})\boldsymbol{m}(\boldsymbol{r}+\Delta\boldsymbol{r}_i) = 1-\frac{1}{2}[\boldsymbol{m}(\boldsymbol{r})-\boldsymbol{m}(\boldsymbol{r}+\Delta\boldsymbol{r}_i)]^2 \approx 1 - \frac{1}{2}\sum_k(\Delta\boldsymbol{r}_i\boldsymbol{\nabla}m_k)^2$ into the above equation we get

$$E_{ex} = C + \int d^3\boldsymbol{r}\sum_{ijk} A_{jk}\frac{\partial m_i}{\partial x_j}\frac{\partial m_i}{\partial x_k}, \tag{4.8}$$

where C results from the integration of the constant term and can be omitted, and A_{jk} is the matrix of exchange constants. By rotation of the cooordinate system this matrix can diagonalized, what yields

$$E_{ex} = \int d^3\boldsymbol{r}\sum_{ij} A_j\Big(\frac{\partial m_i}{\partial x_j}\Big)^2, \tag{4.9}$$

where A_j are positive. In case of cubic and isotropic materials this expression can be reduced to

$$E_{ex} = \int d^3\boldsymbol{r}A\sum_i\Big(\boldsymbol{\nabla}m_i\Big)^2. \tag{4.10}$$

4.1.2 Demagnetization energy.

The demagnetization energy, also called magnetostatic energy or stray field energy, is the energy in the magnetic field created by the magnetization itself. This means that this energy accounts for the dipole-dipole interaction of elementary magnets. The demagnetization energy can be written as

$$E_{dem} = -\frac{1}{2} \int d^3\boldsymbol{r} \boldsymbol{H}_{dem} \boldsymbol{M}, \tag{4.11}$$

where the demagnetization field depends essentially on the geometry of the system and can be expressed via the so-called demagnetization tensor. Mathematically it can be calculated exploiting the notion of "magnetic charges" $-div\boldsymbol{M}$ according to $div\boldsymbol{H} = -4\pi div\boldsymbol{M}$, what follows from $\boldsymbol{B} = \boldsymbol{H} + 4\pi\boldsymbol{M}$ and $div\boldsymbol{B} = 0$. Physically it takes into account the reduction of the internal field in the ferromagnet with respect to the bulk value $4\pi\boldsymbol{M}$ due to fields of the surrounding dipoles. $\boldsymbol{H}_{dem}$ can be calculated analytically only for a number of simplest geometries. An ellipsoid possesses by a constant demagnetizing field $\boldsymbol{H}_{dem} = -\hat{N}\boldsymbol{M}$, where $\hat{N}$ is the demagnetizing tensor.

4.1.3 Anisotropy energy.

Depending on the crystal structure of a ferromagnetic material, it energetically favors the alignment of the magnetization parallel to certain axes. This energy contribution results from spin-orbit interaction and is referred to as anisotropy energy. The energetically favored axes are called easy axes. Depending on the lattice structure material may have one or more easy axes. In the simplest case a material has a single easy axis. This uniaxial anisotropy energy is given by

$$E_{an} = -\int d^3r[K_{u1}(\boldsymbol{m}\boldsymbol{e}_u)^2 + K_{u2}(\boldsymbol{m}\boldsymbol{e}_u)^4], \tag{4.12}$$

where $\boldsymbol{e}_u$ is the unit vector in the direction of the easy axis and $K_{u1,2}$ are anisotropy constants. The phenomenological expression is a result of the Taylor expansion up to the fourth order. Only even powers are allowed in order to fulfill the symmetry condition $E_{an}(\boldsymbol{m}_{easy}) = E_{an}(-\boldsymbol{m}_{easy})$. Uniaxial symmetry occurs in materials with hexagonal or tetragonal crystal structure, e.g. cobalt.

4.1.4 Landau-Lifshitz-Gilbert equation.

Outside equilibrium the effective field, which is defined as $\boldsymbol{H}_{eff} = -(\delta E/\delta \boldsymbol{M})$, will exert a torque $-\gamma \boldsymbol{M} \times \boldsymbol{H}_{eff}$ on the magnetization. This torque causes the magnetization dynamics. The macroscopic dynamics of the magnetization is directly coupled to the microscopic thermal motion of spin waves and also to the conduction electrons and phonons (magnetostriction, magnonphonon scattering). By ways of coupling to these thermal baths, the macroscopic dynamics of the magnetization will be damped out and loose kinetic energy to random thermal motion. To derive the appropriate damping term in the magnetizations equation of motion from first principles is generally quite challenging. This problem can be circumvented by constructing a phenomenological damping term. The most commonly used model is Gilbert damping. Gilbert damping is viscous damping, in which the damping force is proportional to the rate of change of the magnetization, $\alpha \partial \boldsymbol{M}/\partial t$. In the presence of damping, the equation of motion of the magnetization must therefore be

$$\frac{\partial \boldsymbol{M}}{\partial t} = -\gamma \boldsymbol{M} \times \boldsymbol{H}_{eff} + \frac{\alpha}{M_s} \boldsymbol{M} \times \frac{\partial \boldsymbol{M}}{\partial t}, \tag{4.13}$$

this equation is called Landau-Lifshitz-Gilbert (LLG) equation. α is the Gilbert damping parameter and the effective field is calculated as the variational derivative of the full magnetization energy of the ferromagnet. For a thin ferromagnetic film with a uniaxial anisotropy it takes the form

$$\boldsymbol{H}_{eff} = (1/M_s^2)(KM_x\boldsymbol{x} - K_\perp M_y\boldsymbol{y} + A_{ex}\nabla_x^2\boldsymbol{M}) + \boldsymbol{H}_{ext}, \quad (4.14)$$

where $K > 0$ and $K_\perp > 0$ are the anisotropy constants for the easy and hard axes, respectively. the demagnetization field for a thin film geometry is collected into the hard axis anisotropy and can be approximately taken as $\boldsymbol{H}_{dem} = -4\pi M_y\boldsymbol{e}_y$ if the film is in the (x, z)-plane. $\boldsymbol{H}_{ext}$ is the externally applied magnetic field. We assume that the film is elongated along x-axis and the film magnetization depends only on x-coordinate.

4.2 Spin-transfer torques and current-induced magnetization dynamics

The spin transport in heterogeneous magnetic structures with collinear magnetization configuration gives rise to a spin accumulation in diffusive systems. When the electrodes' magnetizations become noncollinear, as in spin valves or magnetic domain wall (DW) structures, a spin accumulation showing a component transverse to the background magnetization appears (see Fig. 4.1). This transverse component of the spin accumulation exerts a torque on the background magnetization via the exchange interaction, leading to magnetization reorientation, switching, or excitations.

Another way to understand the spin transfer torque (STT) is through the angular momentum conservation: the net balance of spin current flowing through an enclosed region is the rate of the total angular momentum change, which is defined as an STT (see Fig. 4.2). We will show later that these two pictures are equivalent only when one neglects the spin-flip scattering and the spin-orbit coupling.

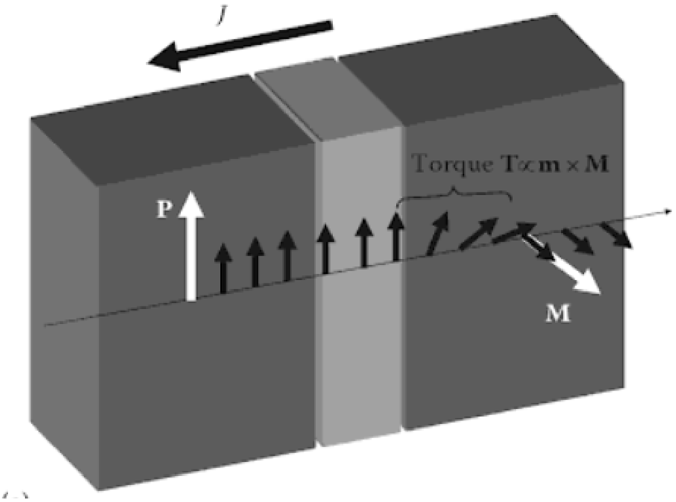

Figure 4.1: Schematics of the spin density profile in a metallic spin-valve without spin diffusion: when impinging into the right layer, the spin density $\boldsymbol{m}$ possesses a component perpendicular to the local magnetization $\boldsymbol{M}$ and exerts a torque of the form $\boldsymbol{T} \sim \boldsymbol{m} \times \boldsymbol{M}$. Adopted from [19].

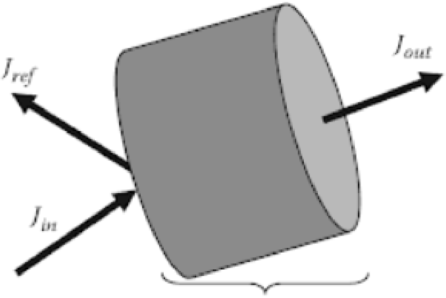

Figure 4.2: Spin transfer picture: the net balance of spin current density is equivalent to a spin transfer to the local magnetization, in the absence of spin diffusion. Adopted from [19].

4.3 $s-d$ model

We work in the framework of the so-called $s-d$ model to describe the spin transport and magnetization dynamics. The $s-d$ model artificially separates the itinerant electrons in $s-p$ bands, which are responsible for the spin transport from the localized d bands, which determine the magnetization. From the microscopic point of view, the $s-d$ model is excessively simplistic. This simplified description introduces inaccuracies in the prediction. However, the $s-d$ model remains a very useful and pedagogical tool that provides qualitatively valuable results in the context of STT. The Hamiltonian of the total spin system is

$$\hat{H} = \hat{H}^{d} + \hat{H}^{sp} - J_{sd}\sum_{i} \hat{S}_i \cdot \hat{s}, \tag{4.15}$$

$$\hat{H}^{d} = g\mu_B \sum_{i} \hat{S}_i \cdot \boldsymbol{H}_{eff} \tag{4.16}$$

$$\hat{H}^{sp} = \frac{\hat{\boldsymbol{p}}^2}{2m} + U(\boldsymbol{r}) - \frac{\hbar}{4m^2c^2}(\boldsymbol{\nabla} U \times \hat{\boldsymbol{p}}) \cdot \hat{\boldsymbol{s}} \tag{4.17}$$

where $\hat{\boldsymbol{S}}_i(\hat{\boldsymbol{s}})$ is the dimensionless spin operator for the i-localized (itinerant) electron, $\boldsymbol{H}_{eff}$ is the effective magnetic field (including the anisotropy, dipolar, and exchange fields), which self-consistently depends on the local spin $\hat{\boldsymbol{S}}_i$.

Applying Ehrenfest's theorem, one obtains the local spin density continuity equation for a localized and an itinerant electron, respectively:

$$\frac{\partial\langle\hat{\boldsymbol{S}}_i\rangle}{\partial t} = \frac{g\mu_B}{i\hbar}\langle[\hat{\boldsymbol{S}}_i, \hat{\boldsymbol{S}}_i \cdot \boldsymbol{H}_{eff}]\rangle + \frac{J_{sd}}{\hbar}\langle\hat{\boldsymbol{S}}_i\rangle \times \langle\hat{\boldsymbol{s}}\rangle \tag{4.18}$$

$$\begin{aligned}\frac{\partial\langle\hat{\boldsymbol{s}}\rangle}{\partial t} = \boldsymbol{\nabla} J_s + \frac{1}{4m^2c^2}\langle(\boldsymbol{\nabla} U \times \hat{\boldsymbol{p}}) \times \hat{\boldsymbol{s}}\rangle - \\ \frac{J_{sd}}{\hbar}\sum_{i}\langle\hat{\boldsymbol{S}}_i\rangle \times \langle\hat{\boldsymbol{s}}\rangle\end{aligned} \tag{4.19}$$

where $\langle ... \rangle$ denotes quantum mechanical averaging on either the local or the itinerant electronic states with a nonequilibrium distribution function. $J_s = -\langle \hat{v} \otimes \hat{s} \rangle$ is the spin current tensor. $\gamma = g\mu_B/\hbar$ is the gyromagnetic ratio. In Eq. (4.18) the commutator $[\hat{\boldsymbol{S}}_i, \hat{\boldsymbol{S}}_i \cdot \boldsymbol{H}_{eff}]$ depends on the detailed dependence of $\boldsymbol{H}_{eff}$ on $\hat{S}_i$. One usually approximates it by the LandauLifshitz-Gilbert (LLG) equation, which includes a precessional term (i.e., takes $\boldsymbol{H}_{eff}$ as a c-number) and a damping term. There are a lot of studies of the microscopic nature of the Gilbert damping. Here we just treat it phenomenologically and focus on the torque coming from the interaction with the conduction electrons' spin and expressed by the last term in Eq. (4.18). The resulting LLG equation takes the form:

$$\frac{\partial \boldsymbol{M}}{\partial t} = -\gamma \boldsymbol{M} \times \boldsymbol{H}_{eff} + \frac{\alpha}{M_s} \boldsymbol{M} \times \frac{\partial \boldsymbol{M}}{\partial t} - \frac{J_{sd}}{2\hbar} \boldsymbol{M} \times \boldsymbol{m}, \tag{4.20}$$

where we have defined the magnetization densities for the local and itinerant electron spins $\boldsymbol{M}/M_s = -\langle \hat{\boldsymbol{S}}_i \rangle / S$ and $\boldsymbol{m} = -2\langle \hat{\boldsymbol{s}} \rangle$, M_s being the saturation magnetization, S is the localized spin magnitude. The first two terms are standard LLG terms and thus the only new term is due to the interaction between the magnetization $\boldsymbol{M}$ and the spin density $\boldsymbol{m}$, which is usually defined as the spin torque (ST) $\boldsymbol{T} = -\frac{J_{sd}}{2\hbar} \boldsymbol{M} \times \boldsymbol{m}$. To determine the spin density $\boldsymbol{m}$, a similar equation of motion for the itinerant spins is needed:

$$\frac{\partial \boldsymbol{m}}{\partial t} = -\boldsymbol{\nabla} J_s - \frac{\delta \boldsymbol{m}}{\tau_{sf}} + \frac{1}{4m^2c^2} \langle (\boldsymbol{\nabla} U \times \hat{\boldsymbol{p}}) \times \hat{\boldsymbol{m}} \rangle + \frac{J_{sd} S}{\hbar M_s} \boldsymbol{M} \times \boldsymbol{m}, \tag{4.21}$$

where we have phenomenologically introduced a spin relaxation time τ_{sf} to model the spin-flip processes by impurities and magnons, $\delta \boldsymbol{m} = \boldsymbol{m} - \boldsymbol{m}_0$ being the nonequilibrium spin density. $\delta \boldsymbol{m}$ is actually the quantity responsible for the current-driven torque since the equilibrium spin accumulation $\boldsymbol{m}_0$ gives rise to a zero-bias interlayer exchange coupling that is usually included in the effective field $\boldsymbol{H}_{eff}$, for the sake of simplicity. Therefore, the nonequilibrium ST has the form: $\boldsymbol{T} = -\frac{J_{sd}}{2\hbar}\boldsymbol{M} \times \delta\boldsymbol{m}$. The coupled equations Eq. (4.20) and Eq. (4.21) determine $\boldsymbol{M}$ and $\delta\boldsymbol{m}$ as long as one can relate the spin current J_s to the magnetization and one can properly evaluate the spin-orbit term. One immediately realizes that in the steady-state, $\partial\boldsymbol{m}/\partial t = 0$, and without the spin-orbit coupling and spin relaxation $1/\tau_{sf} = 0$, the previous equation reduces to $\boldsymbol{T} = -(M_s/2S)\nabla J_s$, that is, the ST can be viewed as the spin current transfer (the processes illustrated by Figs. 4.1 and 4.2 are equivalent).

4.4 Metallic spin valves

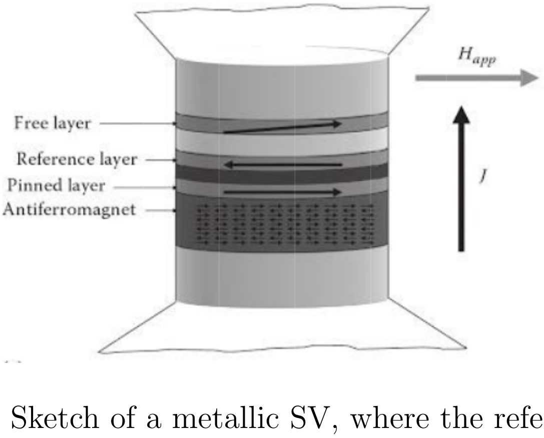

Figure 4.3: Sketch of a metallic SV, where the reference layer is antiferromagnetically coupled (usually through Ru) to a ferromagnetic layer pinned by an antiferromagnet (IrMn, PtMn, etc.). The spacer layer that separates the free layer from the reference layer is usually Cu, whereas the ferromagnetic layers can be Co, CoFe, NiFe, etc. Adopted from [19].

A metallic SV is composed of two ferromagnetic systems separated by a metallic spacer (see Fig. 4.3). Since the voltage drop across the metallic SV is rather small, on the order of only $1mV$ even for a current density as high as $10^8\ A/cm^2$, the linear response theory is sufficiently accurate for the calculation of the ST. Furthermore, the spin-orbit coupling is usually small compared to the $s-d$ interaction and thus Eq. (4.21) reduces to

$$\frac{\partial \boldsymbol{m}}{\partial t} = -\boldsymbol{\nabla} J_s - \frac{\delta \boldsymbol{m}}{\tau_{sf}} - \frac{2S}{M_s}\boldsymbol{T}. \tag{4.22}$$

In the steady-state $\partial \boldsymbol{m}/\partial t = 0$, the ST is thus $(2S/M_s)\boldsymbol{T} = -\boldsymbol{\nabla} J_s - \frac{\delta \boldsymbol{m}}{\tau_{sf}}$. In order to explicitly find the STT from the previous equation, one needs to relate the spin current tensor J_s to the non equilibrium spin accumulation $\delta \boldsymbol{m}$. In the ballistic transport $1/\tau_{sf} = 0$ however, the current and the spin accumulation are not directly related because the spin accumulation is not well defined. In this case, one simply has $(2S/M_s)\boldsymbol{T} = -\boldsymbol{\nabla} J_s$. If one integrates over the entire magnetic layer, the total STT on the layer $\boldsymbol{T} \propto -\int\limits_{in}^{out} d\Omega \boldsymbol{\nabla} J_s = J_{s,in} - J_{s,out}$, that is, the total STT is determined by the difference between the incoming and outgoing spin current at two sides of the layer.

The assumption of the ballistic transport is in fact a very poor approximation in the case of metallic SVs. It has been well established that diffusive spin-dependent transport is the proper description for metallic multilayers, as long as the layer thickness is large compared to the mean free path: diffusive scattering in the layers and at interfaces contributes to the spin current and magnetoresistance. For the noncollinear magnetization, the extension to the drift-diffusion model is straightforward as long as one replaces the spin up and down channels by the 2×2 spinor tensor. Specifically, one defines the spinor form of the current as

$$\hat{j} = \frac{1}{2}\boldsymbol{j}_c\hat{I} + \frac{1}{2}\hat{J}_s\hat{\boldsymbol{\sigma}}, \tag{4.23}$$

where $\boldsymbol{j}_c$ is a vector describing the charge current, $\hat{J}_s$ is a spin current tensor. $\hat{I}$ is the 2×2 unity matrix and $\hat{\boldsymbol{\sigma}}$ is the vector of Pauli spin matrices.

Within this formalism, in the presence of external electric field $\boldsymbol{E}$ and inhomogeneous (spin-dependent) electronic density $\hat{n}$, the spinor form of the current reads:

$$\hat{j} = \hat{C}\boldsymbol{E} - \hat{D}\boldsymbol{\nabla}\hat{n}, \tag{4.24}$$

where $\hat{C} = C_0(\hat{I} + \beta\hat{\boldsymbol{\sigma}}\boldsymbol{M}/M_s)$ is the generalized conductivity, $\hat{D} = D_0(\hat{I} + \beta'\hat{\boldsymbol{\sigma}}\boldsymbol{M}/M_s)$ is the generalized diffusion constant and $\hat{n} = n_0\hat{I} + \hat{\boldsymbol{\sigma}}\boldsymbol{m}$ is the generalized accumulation accounting for both charge $2n_0$ and spin $\boldsymbol{m}$ accumulations. β and β' are the spin asymmetries of the conductivity and diffusion constants, responsible for the spin polarization of the current. All these quantities are 2×2 matrices. The diffusion constant and the conductivity are related via the Einstein relation $\hat{C} = e^2\hat{N}(E_F)\hat{D}$, where $\hat{N}(E_F)$ is the density of states at the Fermi energy. The spinor form of Eq. (4.24) provides one scalar relation for j_c that must be completed with the steady-state charge density continuity equation $\boldsymbol{\nabla} j_c = 0$. From Eqs. (4.23) and (4.24) the spin current $J_s = \mathrm{Re}[\mathrm{Tr}(\hat{\boldsymbol{\sigma}}\hat{j})]$ can be explicitly expressed in terms of the charge current plus a diffusion term, that is i-th component in real space and k-th component in spin space of the tensor J_s takes the form

$$J_{s,ik} = \beta j_{c,i}\frac{\boldsymbol{M}_k}{M_s} - 2D_0\Big[\frac{\partial \boldsymbol{m}_k}{\partial \boldsymbol{r}_i} - \beta\beta'\frac{\boldsymbol{M}_k}{M_s^2}(\boldsymbol{M} \cdot \frac{\partial \boldsymbol{m}}{\partial \boldsymbol{r}_i})\Big], \tag{4.25}$$

By placing this spin current into the steady-state version of Eq. (4.22) and assuming that all quantities depend only on

x-coordinate perpendicular to the SV plane, we have

$$\frac{\boldsymbol{m}\times\boldsymbol{M}}{M_s\lambda_J^2}=\frac{d^2\boldsymbol{m}}{dx^2}-\beta\beta'\frac{\boldsymbol{M}}{M_s^2}(\boldsymbol{M}\cdot\frac{d^2\boldsymbol{m}}{dx^2})-\frac{\delta\boldsymbol{m}}{\lambda_{sf}^2},\qquad(4.26)$$

where $\lambda_{sf}=\sqrt{2D_0\tau_{sf}}$ and $\lambda_J=\sqrt{2\hbar D_0/SJ_{sd}}$.

We separate the spin accumulation into longitudinal (parallel to the local moment) and transverse (perpendicular to the local moment) modes. Eq. (4.26) can now be written as

$$\frac{d^2\boldsymbol{m}_\parallel}{dx^2}-\frac{\delta\boldsymbol{m}_\parallel}{\lambda_{sdl}^2}=0,\qquad(4.27)$$

$$\frac{d^2\boldsymbol{m}_\perp}{dx^2}-\frac{\delta\boldsymbol{m}_\perp}{\lambda_{sf}^2}-\frac{\delta\boldsymbol{m}_\perp\times\boldsymbol{M}}{M_s\lambda_J^2}=0,\qquad(4.28)$$

where $\lambda_{sdl}=\sqrt{1-\beta\beta'}\lambda_{sf}$.

Eqs. (4.26)-(4.28) is the generalization of the drift-diffusion model to the noncollinear magnetization configurations. While the longitudinal spin accumulation has a length scale determined by the spin-flip length λ_{sdl} which is on the order of 10 nm or longer for the transition ferromagnets, the transverse spin accumulation has much shorter length scale λ_J, ranging from a few angstroms to a few tens of angstroms.

In principle, the magnetization dynamics involves simultaneous time-dependent solutions for $\boldsymbol{M}(\boldsymbol{r},t)$ and $\boldsymbol{m}(\boldsymbol{r},t)$. However, the analysis of the timescale for $\boldsymbol{M}(\boldsymbol{r},t)$ and $\boldsymbol{m}(\boldsymbol{r},t)$ can reduce the problem to a steady-state condition for the conduction electrons, that is, $\partial\boldsymbol{m}/\partial t=0$. To see this, one notices that it only takes about 1 fs (transport relaxation time) to establish a steady-state charge current after one applies an electric field to any heterogeneous conducting system. To establish a steady-state spin density and spin current in a magnetic system, the time-scale would be $\tau_{sf}\sim l_{sf}/v_f\sim 10\ fs-1\ ps$. The time scale of $\boldsymbol{M}$ is on the order of nanoseconds, much longer than τ_{sf}. Therefore, as long as one is interested in the magnetization process of the local moments, one can always treat the spin accumulation in the limit of long times. The two dynamic equations [Eq. (4.20) for $\boldsymbol{M}(\boldsymbol{r},t)$ and Eq. (4.22) for $\boldsymbol{m}(\boldsymbol{r},t)$] are then simply decoupled: we first solve Eq. (4.22) with fixed local moments (independent of time) and take $\boldsymbol{m}(t)$ in the limit of long times when $\partial \boldsymbol{m}/\partial t = 0$. Once the spin accumulation is obtained, we substitute it into Eq. (4.20) to solve the dynamics of the local moments.

Let's denote the unit vectors in the directions of magnetizations of the two ferromagnets composing SV as $\boldsymbol{M}_1$ and $\boldsymbol{M}_2$. We consider the torque caused by $\boldsymbol{m}$ on $\boldsymbol{M}_1$ in the first ferromagnet. Going back to Eq. (4.20) we see that only the transverse to $\boldsymbol{M}_1$ component of $\boldsymbol{m}$ matters for the torque. Without loss of generality, we can write the two components of the accumulation $\boldsymbol{m}$ in the plane transverse to $\boldsymbol{M}_1$ as

$$(J_{sd}/2\hbar)\boldsymbol{m} = a\boldsymbol{M}_2 \times \boldsymbol{M}_1 + b(\boldsymbol{M}_1 \times \boldsymbol{M}_2) \times \boldsymbol{M}_1, \quad (4.29)$$

where a and b are determined by geometric details of the multilayer. The second term can be viewed as the current-dependent contribution to the effective field and the first contribution cannot be reduced to the effective field and often called the "spin transfer torque".

The field-like torque, expressed by the second term in Eq. (4.29), and the spin transfer torque (which is also often called "anti-damping torque"), expressed by the first term in Eq. (4.29), are shown in Fig. 4.4.

4.4.1 Magnetization dynamics in a metallic spin-valve

A useful tool to describe the dynamic properties of a magnetic layer under a spin-polarized current is the magnetic phase diagram that displays the magnetic stability regions of thespin-valve as a function of the external magnetic field and applied

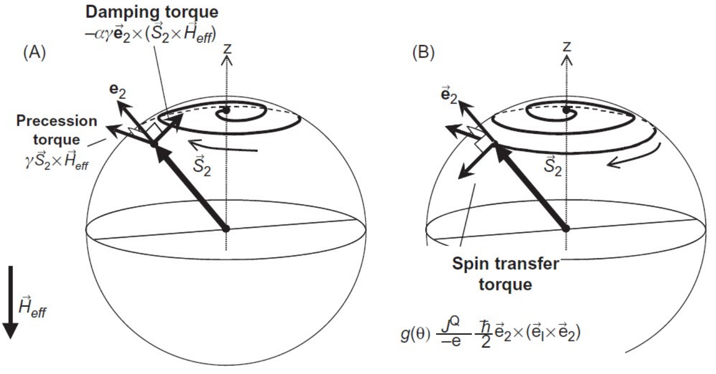

Figure 4.4: Adopted from [1].(a) Field-like torque, or precession torque. It makes the spin to precess around the field. The spiral shrinks to the field direction due to the damping torque. (b) Current induced spin transfer torque, which may act opposite to the damping torque and in this case is called anti-damping torque.

bias. The geometry of the system is displayed in Fig. 4.3. The SV consists of two ferromagnetic layers separated by a spacer. The system is a pillar along the z direction with an elliptic shape lying in the (x, y) plane. The bottom (reference) layer has a magnetization direction $\boldsymbol{P} = +x$ assumed to be fixed, and the top (free) layer has a magnetization direction $\boldsymbol{M}$, an easy axis is along the x-direction, and a demagnetizing field in the z direction.

To find the dynamics of $\boldsymbol{M}$ we need to solve the LLG equation Eq. (4.20). It requires the precise knowledge of the effective field $\boldsymbol{H}_{eff}$ and the torque $\boldsymbol{T}$. In principle, $\boldsymbol{H}_{eff}$ comprises the exchange field $\boldsymbol{H}_{ex}$, the anisotropy field $\boldsymbol{H}_{an} = KM_x/M_s\boldsymbol{e}_x$, the demagnetization field $\boldsymbol{H}_d = -4\pi M_z\boldsymbol{e}_z$, and the external applied field $\boldsymbol{H}_{ext}$. The current-induced effective field as well as the interlayer exchange coupling can also be included. The spatial variations of $\boldsymbol{M}$ are neglected so that the exchange field is disregarded. Then, the total effective field reduces to $\boldsymbol{H}_{eff} = \boldsymbol{H}_{ext} + \boldsymbol{H}_d + \boldsymbol{H}_{an}$. Since the perpendicular torque, the second term of Eq. (4.29), can be absorbed to the effective field, we should neglect this term and solely consider the STT given by the first term of Eq. (4.29). Then in spherical coordinates $\boldsymbol{M} = M_s(\cos\theta, \sin\theta\cos\phi, \sin\theta\sin\phi)$ the LLG equation (4.20) is reduced to

$$\frac{1+\alpha^2}{\gamma}\dot{\theta} = h_\phi + \alpha h_\theta, \tag{4.30}$$

$$\frac{1+\alpha^2}{\gamma}\sin\theta\dot{\phi} = \alpha h_\phi - h_\theta, \tag{4.31}$$

where h_ϕ and h_θ are functions of (θ, ϕ), that we do not write explicitly. The conventional method to obtain the stability conditions for the magnetization $\boldsymbol{M}$ is to study the stability of small deviations from the equilibrium $\delta\boldsymbol{M}$, under an applied current. The equilibrium magnetization direction $\boldsymbol{M}_0$ is defined as $h_{\theta,\phi}(\boldsymbol{M}_0) = 0$, with $a = 0$ at $j_e = 0$. In the case where the external field is $\boldsymbol{H}_{ext} = H_x\boldsymbol{e}_x$, $\boldsymbol{M}_0 = M_s(\pm 1, 0, 0)$. Inserting the perturbed magnetization $\boldsymbol{M} = \boldsymbol{M}_0 + \delta\boldsymbol{M}$ in Eqs. (4.30) and (4.31) and assuming that $\boldsymbol{M}^2 = M_s^2$, one obtains two differential equations for δM_y and δM_z that can be solved analytically. The resulting stability conditions for the parallel (P) and antiparallel (AP) states are:

$$J_e < \alpha\frac{H_x + K + H_d/2}{a}, \qquad H_x > -K, \quad (P) \tag{4.32}$$

$$J_e > -\alpha\frac{H_x - K - H_d/2}{a}, \qquad H_x < K. \quad (AP) \tag{4.33}$$

As long as conditions (4.32) and (4.33) are met, either P or AP or even both states are stable, as illustrated in Fig. 4.5. However, when these conditions are not met, the P and AP configurations become unstable: the magnetization jumps to new stable states (denoted E in Fig. 4.5). These novel states

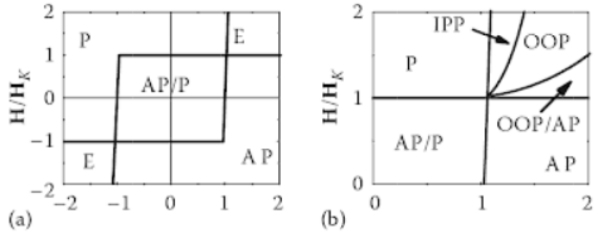

Figure 4.5: Stability diagrams for the free layer: (a) At zero temperature, (b) zoom of the zero temperature diagram for positive field and current, including IPP and OPP. Adopted from [19].

are unique characteristics of the ST. The ”E” regions out of the stability regions reveal a rich variety of magnetization regimes, including in plane precessions (IPP), out-of-plane precessions (OPP), and inhomogeneous magnetic excitations. The fact that the STT term a can be either positive or negative, depending on the current direction, allows reaching steady precessional states in which the damping is exactly compensated by the STT (they are called E-states because of the energy conservation).

The comparison between current-induced and field-induced magnetization reversal in nanopillars is shown in Fig. 4.6. During the current-induced dynamics the magnetic moment at first escapes from the one of potential minima under the influence of the antidamping torque and then goes to the other minimum due to the combined action of the Gilbert damping and current-induced torque, which is now also damping-like. During the field-induced dynamics there is only one potential minimum and the magnetic moment precesses around the field direction shrinking the spiral to the only stable state.

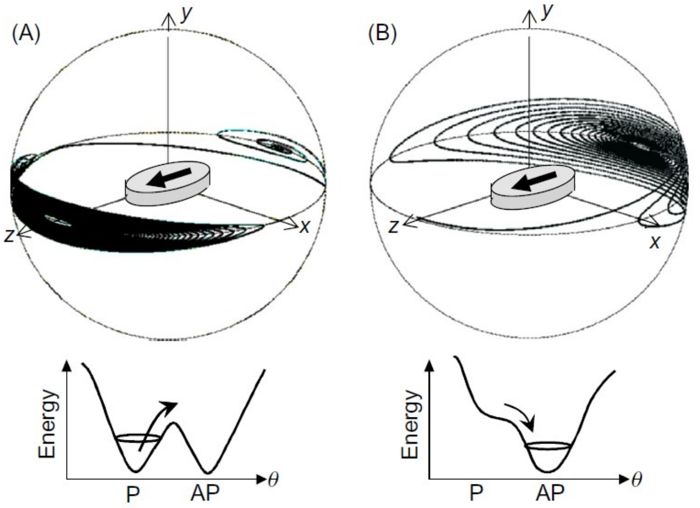

Figure 4.6: Adopted from [1].Comparison of the magnetization processes driven by (A) spin-transfer torque and (B) external magnetic field for in-plane magnetized nanopillars.

4.4.2 Experimental results on current-induced magnetization switching in spin valves.

Spin injection magnetization switching (SIMS) was first predicted theoretically and was then experimentally demonstrated for a Co/Cu/Co nanopillar with in-plane magnetization [20, 21]. Subsequently, SIMS was also observed in the case of MTJs with Al-O barriers [22] and MgO barriers [23, 24]. All those magnetic pillars had in-plane magnetization. And their cross sections were ellipses or rectangles. In 2006, SIMS was also observed in magnetic nanopillars with perpendicular magnetization [25]. They employed Co/Ni multilayers to give a perpendicular crystalline anisotropy to the film.

In Fig. 4.7, a typical structure of nanopillars from an MTJ (for research purposes) is shown. A hysteresis loop obtained

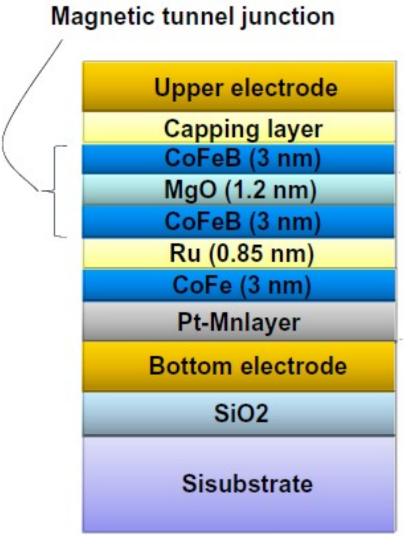

Figure 4.7: A typical structure of nanopillars from an MTJ [1].

for a magnetic nanopillar comprising a CoFeB/MgO/ CoFeB tunneling junction is shown in Fig. 4.8. The pillar has in-plane magnetization and elliptical cross section with the dimensions 100 nm × 3200 nm. A current was applied as a series of 100 ms wide pulses. In between the pulses, the sample resistance was measured to check the magnetization configuration. By this method, the effect of temperature increase during the application of the current on the resistance measurement could be eliminated. The hysteresis measurement started at a zero pulse height for the P state. An increase in the pulse height caused a jump from the P state to the AP state at 0.6 mA. Further increase in the pulse height followed by a reduction to zero current did not affect to the state. Subsequently, negative pulses were applied to the sample. At 0.35 mA, the sample switched its magnetization from the AP state to the P state.

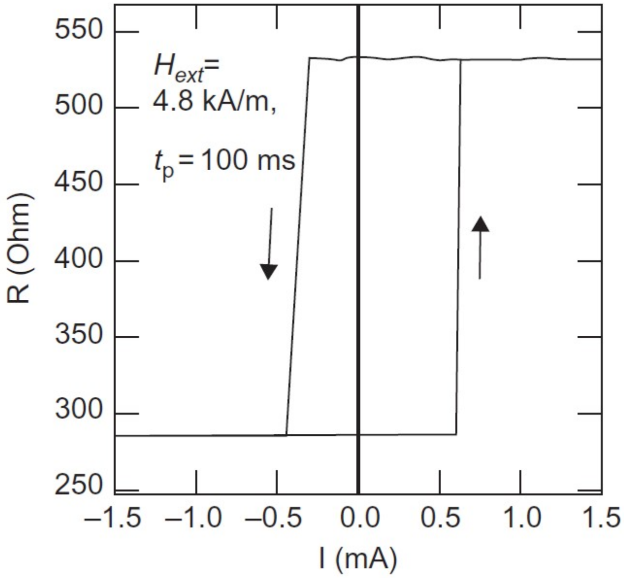

Figure 4.8: A typical SIMS hysteresis loop obtained for a CoFeB/MgO/CoFeB MTJ. Measurements were performed at room temperature using electric current pulses of 100 ms duration. The resistance of the junction was measured after each pulse to avoid the effect of the heating on the sample resistance. From Ref. [23].

4.5 Field-induced DW motion.

Let us consider a thin ferromagnetic film with a uniaxial anisotropy. In this case the full effective field takes the form

$$\boldsymbol{H}_{eff} = (1/M_s^2)(KM_x\boldsymbol{x} - K_\perp M_y\boldsymbol{y} + A_{ex}\nabla_x^2\boldsymbol{M}) + \boldsymbol{H}_{ext}, \quad (4.34)$$

where $K > 0$ and $K_\perp > 0$ are the anisotropy constants for the easy and hard axes, respectively. The demagnetization field for a thin film geometry is collected into the hard axis anisotropy and can be approximately taken as $\boldsymbol{H}_{dem} = -4\pi M_y\boldsymbol{y}$ if the film is in the (x, z)-plane. In this limiting case $K_\perp/M_s^2 = 4\pi$. $\boldsymbol{H}_{ext}$ is the externally applied magnetic field. We assume that the film is elongated along x-axis and the film magnetization depends only on x-coordinate.

Now we are ready to consider the behavior of a DW under the applied magnetic field $\boldsymbol{H}_{ext} = H_{ext}\boldsymbol{x}$. It is convenient to parametrize the magnetization as follows:

$$\boldsymbol{M} = M_s(\cos\theta, \sin\theta\cos\delta, \sin\theta\sin\delta), \tag{4.35}$$

where in general the both angles depend on (x, t). At zero applied current and at $\boldsymbol{H}_{ext} = 0$ the equilibrium shape of the DW is determined by the condition $\dot{M} = 0$ and from the LLG equation (4.48) we obtain that it results in the condition $\boldsymbol{M} \times \boldsymbol{H}^{eq}_{eff} = 0$. Making use of parametrization (4.35) we can express $\boldsymbol{H}_{eff}$ as

$$\begin{aligned}\boldsymbol{H}^{eq}_{eff} = (1/M_s)[(K\cos\theta - A_{ex}\theta''\sin\theta - A_{ex}\cos\theta(\theta')^2)\boldsymbol{x} +\\ (-K_\perp\sin\theta\cos\delta + A_{ex}\cos\delta(\theta''\cos\theta - \sin\theta(\theta')^2))\boldsymbol{y} +\\ A_{ex}\sin\delta(\theta''\cos\theta - \sin\theta(\theta')^2)\boldsymbol{z}].\end{aligned} \tag{4.36}$$

The solution of $\boldsymbol{M} \times \boldsymbol{H}^{eq}_{eff} = 0$ is given by $\delta = \pi/2$ and $\theta(x)$ obeying the equation

$$\theta'' - \frac{K}{A_{ex}}\cos\theta\sin\theta = 0. \tag{4.37}$$

The solution of Eq. (4.37) satisfying the appropriate asymptotic conditions takes the form

$$\cos\theta = \nu\tanh[(x - x_0)/d_w], \tag{4.38}$$

where $d_w = \sqrt{A_{ex}/K}$ is the DW width. The above ansatz corresponds to the head-to-head DW ($\nu = -1$) or tail-to-tail ($\nu = 1$), lying in the xz-plane (see Fig. 4.9).

Figure 4.9: Head-to-head domain wall.

First of of all, we consider the mechanism of the field-driven domain-wall motion qualitatively. When an external magnetic field is applied to the easy-axis [Fig. 4.10(a)], the magnetization in the wall tilts out the easy-axis plane due to the torque caused by the external field [Fig. 4.10(b)]. This tilting wall feels an effective magnetic field $B_\perp$ arising from the hard-axis anisotropy $K_\perp$, which leads to a rotation of the magnetization around the y-axis and thus the translational motion of the domain wall occurs [Fig. 4.10(c)].

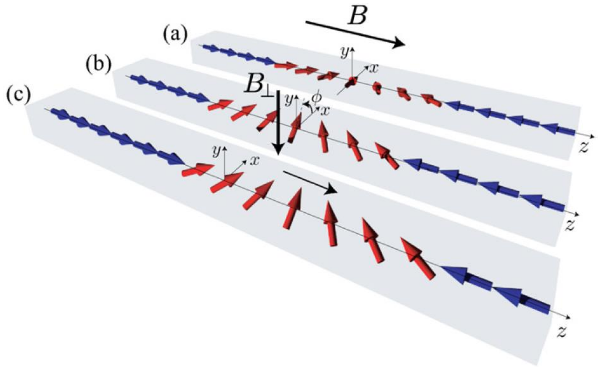

Figure 4.10: Qualitative illustration of a DW motion mechanism. Adopted from [26].

Now our goal is to find the DW velocity at small applied fields. We follow the Walker's procedure [27] by assuming that $\delta = \delta(t)$ and the DW is moving according to the time-dependent shift $x_0(t) = \int\limits_0^t v(t')dt'$ in the Eq.(4.38). We assume that the distortion of the wall is small during the wall motion, that is $\delta = \pi/2 + \delta_1$, where $|\delta_1| << 1$. In this case taking into account that $d_w \nabla_x \theta = -\nu \sin\theta$ for the DW we obtain

$$\partial_t \delta_1 = \nu \frac{\alpha v}{d_w} + \gamma H_{ext} \tag{4.39}$$

$$-(1+\alpha^2)\nu v = \frac{\gamma d_w K_\perp \delta_1}{M_s} + d_w \alpha \gamma H_{ext}. \tag{4.40}$$

In this case Eqs. (4.39) and (4.40) yield the following equation for $v(t)$:

$$\partial_t v + \frac{\gamma \alpha K_\perp}{M_s(1+\alpha^2)} v = -\nu \frac{d_w \gamma^2 K_\perp H_{ext}}{M_s(1+\alpha^2)}. \tag{4.41}$$

Taking into account the initial condition determined by the Eq. (4.40) $(1+\alpha^2)v(t=0) = -\nu d_w \alpha \gamma H_{ext}$, which follows from $\delta_1(t=0) = 0$ we determine the solution of Eq. (4.41) in the form:

$$v(t) = \frac{\nu d_w \gamma H_{ext}}{\alpha} \frac{e^{-t/t_d}}{(1+\alpha^2)} - \frac{\nu d_w \gamma H_{ext}}{\alpha}, \tag{4.42}$$

$$\delta(t) = \frac{\pi}{2} + \frac{t_d\left(1 - e^{-t/t_d}\right)}{1+\alpha^2} \gamma H_{ext}. \tag{4.43}$$

where $t_d = (1+\alpha^2)M/(\alpha\gamma K_\perp)$ is the characteristic time scale.

It is important that the applied magnetic field moves DWs of opposite types ($\nu = \pm 1$) to opposite directions. In other words, the field enlarges the energetically favorable domain and shrinks the energetically unfavorable domain.

The solution (4.42,4.43) is only valid for small enough fields applied to the system. If the field is large enough, the condition $|\delta_1| \ll 1$ is violated and Eqs. (4.39) and (4.40) are not valid. The DW can still be moved by the field, but it does not preserve its plane equilibrium shape Eq. (4.38) and the motion acquires a precessional character. The wall velocity as a function of the magnetic field is sketched in Fig. 4.11. The steady motion when the wall preserves its equilibrium plane shape is changed by the precessional motion at the field which is called by the "Walker breakdown" field.

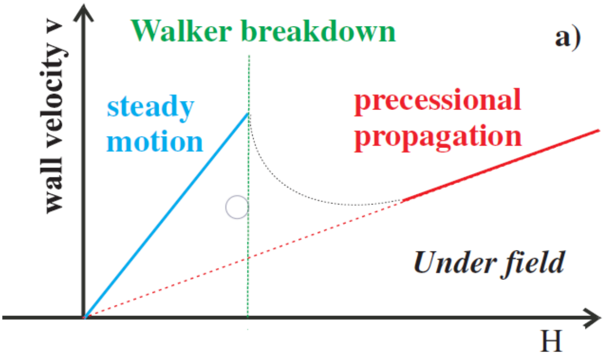

Figure 4.11: Sketch of a DW velocity as a function of the external magnetic field. Adopted from [28].

Getting rid of the linear approximation $\delta \approx \pi/2 + \delta_1$, where $\delta_1 \ll 1$, one can find the Walker's breakdown field $H_W = K_\perp \alpha/(2M_s)$. The frequency of a stationary precession above the Walker's breakdown field takes the form $\omega = \gamma\sqrt{H_{ext}^2 - H_W^2}/(1+\alpha^2)$. The average over the precession period velocity of the DW motion above the Walker's breakdown field is $\bar{v} = -(\nu d_w \gamma H_{ext}/\alpha)[1 - \sqrt{1 - H_W^2/H_{ext}^2}/(1+\alpha^2)]$. At $H_{ext} \gg H_W$ the above expression gives $\bar{v} = -\nu d_w \gamma H_{ext}\alpha/(1+\alpha^2)$. In a typical experimental situation $\alpha \lesssim 0.02$. In this case the ratio of the DW velocities below and above the Walker's breakdown is $v/\bar{v} = 1/\alpha^2$. Therefore, the DW velocity above the Walker's breakdown is greatly suppressed.

Experimental results on the field-driven DW motion are presented in Figs. 4.12, 4.13. Fig. 4.12 explains the measurement technique, while the results of the DW velocity as a function of the applied field are presented in Fig. 4.13.

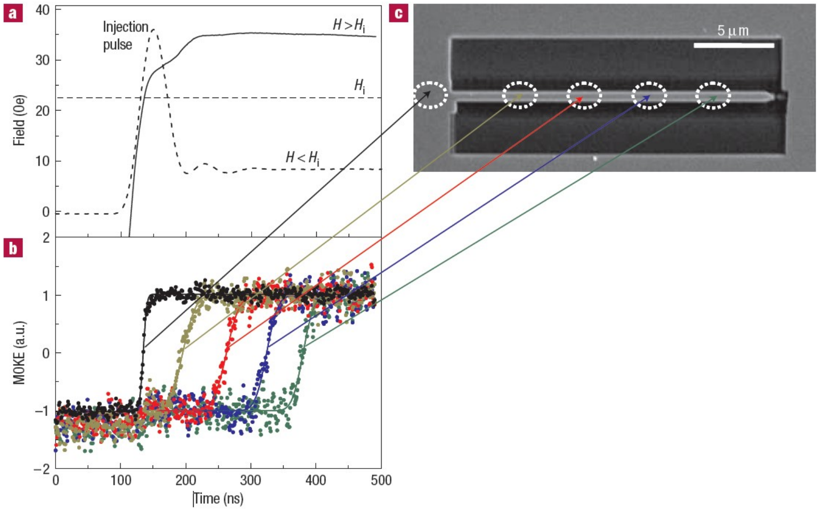

Figure 4.12: Field-driven magnetization reversal measurements. (a) Example drive-field waveforms used for fields above (solid line) and below (dashed line) the wall injection field, H_i. (b) Time-resolved magneto-optical Kerr effect (MOKE) signal (symbols) and fits to the error function (solid lines), in response to the 35 Oe field waveform of (a). The MOKE transients were measured at the nanowire locations indicated in (c). (c) The scanning electron micrograph; ellipses approximate the measured width of the laser spot. From [29].

4.6 Spin-transfer torque and current-induced DW motion in textured ferromagnets

4.6.1 Spin-transfer torque

As an electric current flows in a DW, the spin current, whose spin direction is varying along with the direction of the magne-

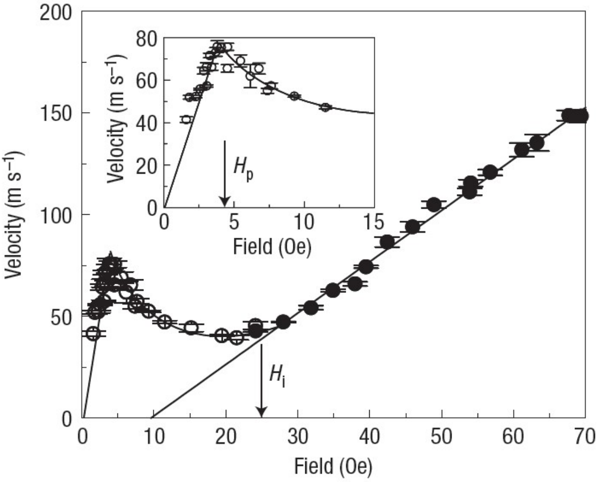

Figure 4.13: Average domain-wall velocity versus field step amplitude. Arrows mark the domain-wall injection field, H_i, and velocity peak, H_p. Straight solid lines are linear fits to the data below H_p and above H_i, respectively; the curved line is a visual guide. Filled symbols show velocities obtained for a square-wave drive field and open symbols those obtained using injection pulse waveforms, such as in Fig. 4.12(a). The inset shows the detail around the velocity peak. From [29].

tization $\boldsymbol{M}(r,t)$ is locally absorbed, producing an STT. Again, we use the diffusive transport model and separate the equilibrium and nonequilibrium parts of the spin density and the spin current

$$\boldsymbol{m}(\boldsymbol{r},t) = \boldsymbol{m}_0 \frac{\boldsymbol{M}(\boldsymbol{r},t)}{M_s} + \delta\boldsymbol{m}(\boldsymbol{r},t), \tag{4.44}$$

$$J_s = -\frac{P}{2eM_s}\boldsymbol{j}_e \otimes \boldsymbol{M}(\boldsymbol{r},t) + \delta J_s, \tag{4.45}$$

where $\delta\boldsymbol{m}$ and δJ_s are the nonadiabatic parts of spin density and spin current, $\boldsymbol{m}_0$ is the equilibrium itinerant spin density and P is the current polarization.

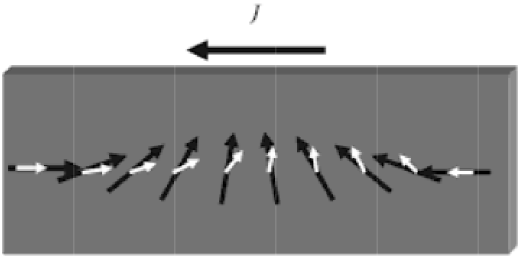

Figure 4.14: Schematics of spin transport through a magnetic transverse DW. Adopted from [19].

The semiclassical diffusive theory presented earlier relates the nonequilibrium current density to the nonequilibrium spin density [Eq.(4.25)]. By inserting Eq. (4.44) and Eq. (4.45) into Eq. (4.22), and discarding the time derivation of the magnetization and assuming a slow variation of the magnetization in the DW (that is, neglecting the second order coordinate derivatives) we have

$$\boldsymbol{T} = \frac{\gamma\hbar P}{eM_s}(\boldsymbol{j}_e\boldsymbol{\nabla})\boldsymbol{M} - \frac{2M_s\delta\boldsymbol{m}}{S\tau_{sf}}. \tag{4.46}$$

The nonadiabatic part of the electron magnetization $\delta\boldsymbol{m}$ is perpendicular to the local direction of $\boldsymbol{M}(\boldsymbol{r},t)$, that is can be written as $\delta\boldsymbol{m} = B_1(\boldsymbol{j}_e\boldsymbol{\nabla})\boldsymbol{M} + (B_2/M_s)\boldsymbol{M}\times(\boldsymbol{j}_e\boldsymbol{\nabla})\boldsymbol{M}$. Coefficients B_1 and B_2 can be found in the framework of a given microscopic model. The first term of this expression can be effectively included into the first term of Eq. (4.46), but the second term does not. Typically microscopic calculations indicate that $B_{1,2}/\tau_{sf}$ is considerably smaller than $\gamma\hbar P/2eM_s$. Neglecting the term proportional to B_1 (or effectively including it into the first term of the torque) we obtain

$$\boldsymbol{T} = \frac{\gamma\hbar P}{eM_s}\Big[(\boldsymbol{j}_e\boldsymbol{\nabla})\boldsymbol{M} - \frac{\beta}{M_s}\boldsymbol{M}\times(\boldsymbol{j}_e\boldsymbol{\nabla})\boldsymbol{M}\Big]. \tag{4.47}$$

These two terms are sometimes referred to as the adiabatic and nonadiabatic torques, respectively. Both torques vanish in the absence of DW, and interestingly, the nonadiabatic torque is proportional to the spin-flip scattering in this model. Then, in the absence of spin-flip scattering, the nonadiabatic torque vanishes and the DW only generates an adiabatic torque.

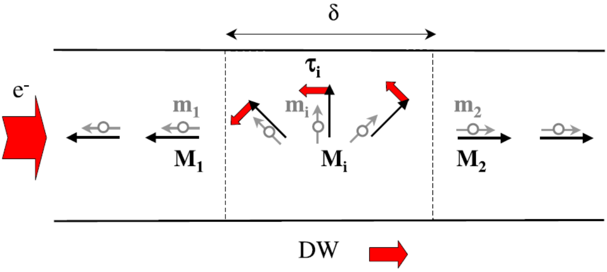

Figure 4.15: Adiabatic spin transfer torque. Adopted from [30].

4.6.2 Current-induced magnetization dynamics of domain walls

Now our goal is to investigate the magnetization dynamics of the domain wall in a ferromagnetic thin film under the action of the electric current. Our analysis is based on the LLG equation, which includes the current-induced torque terms discussed above. The LLG equation takes the form

$$\frac{\partial \boldsymbol{M}}{\partial t} = -\gamma \boldsymbol{M} \times \boldsymbol{H}_{eff} + \frac{\alpha}{M_s} \boldsymbol{M} \times \frac{\partial \boldsymbol{M}}{\partial t} + \boldsymbol{T}, \tag{4.48}$$

where the effective field takes the form

$$\boldsymbol{H}_{eff} = (1/M_s^2)(K M_x \boldsymbol{x} - K_\perp M_y \boldsymbol{y} + A_{ex} \nabla_x^2 \boldsymbol{M}), \tag{4.49}$$

where $K > 0$ and $K_\perp > 0$ are the anisotropy constants for the easy and hard axes, respectively. A_{ex} is the constant describing the inhomogeneous part of the exchange energy.

The torque $\boldsymbol{T}$ can be expressed as a sum of the adiabatic and nonadiabatic contributions

$$\boldsymbol{T} = b_J(\boldsymbol{j}_e\boldsymbol{\nabla})\boldsymbol{M} - \frac{c_J}{M_s}\boldsymbol{M} \times (\boldsymbol{j}_e\boldsymbol{\nabla})\boldsymbol{M}, \tag{4.50}$$

where $b_J = 2Pj_e\mu_B/eM_s$ and $c_J = \zeta b_J$, ζ - is the dimensionless phenomenological parameter describing the degree of nonadiabaticity the spin of conduction electrons and the local magnetization.

Now let us consider the behavior of the head-to head DW induced by the electric current applied along the x-axis. The solution for the DW velocity under the action of small applied current can be found exactly in the same way as for the case of applied field. Let us consider the same parametrization of the magnetization Eq. (4.35). Again we assume that $\delta = \delta(t) \approx \pi/2 + \delta_1$, where $|\delta_1| << 1$ and the DW is moving according to the time-dependent shift $x_0(t) = \int\limits_0^t v(t')dt'$ in the Eq.(4.38). Assuming that $\delta_1 \propto j$, in the linear order with respect to j we can obtain from the LLG equation:

$$\partial_t\delta_1 = \nu\frac{\alpha v}{d_w} + \frac{c_J j\nu}{d_w} \tag{4.51}$$

$$-\frac{\nu v}{d_w} = \frac{\gamma K_\perp \delta_1}{M_s} + \alpha\dot{\delta}_1 + \frac{b_J\nu j}{d_w}. \tag{4.52}$$

Eqs. (4.51) and (4.52) yield the following equation for $v(t)$:

$$\partial_t v + \frac{\gamma\alpha K_\perp}{M_s(1+\alpha^2)}v = -\frac{\gamma K_\perp c_J j}{M_s(1+\alpha^2)}. \tag{4.53}$$

The solution of the above equation satisfying the initial condition $v(0) = -(b_J + \alpha c_J)j/(1+\alpha^2)$ takes the form

$$v = -\frac{c_J j}{\alpha} + e^{-t/t_d}\Big(\frac{c_J j}{\alpha} - \frac{(b_J + \alpha c_J)j}{1+\alpha^2}\Big). \tag{4.54}$$

Then $\delta_1(t)$ can also be found from Eqs. (4.51) and (4.52):

$$\delta_1 = -\frac{\nu M_s}{d_w \gamma K_\perp}\Big[(1+\alpha^2)v + (b_J + \alpha c_J)j\Big]. \tag{4.55}$$

It is seen that the adiabatic torque by itself does not cause the steady DW motion in the regime of small applied current, it just shifts the wall center from its initial position. However, it does move the DW at $j_e > j_{e,th}$. In this regime of large applied currents higher than the threshold current $j_{e,th}$ the plane equilibrium shape of the DW is not preserved and the DW motion is precessional similar to the field-induced DW motion above the Walker breakdown. In the regime of small applied currents $j_e < j_{e,th}$ the wall can be only moved by the non-adiabatic STT or by the spin-orbit torque (is considered later in the notes).

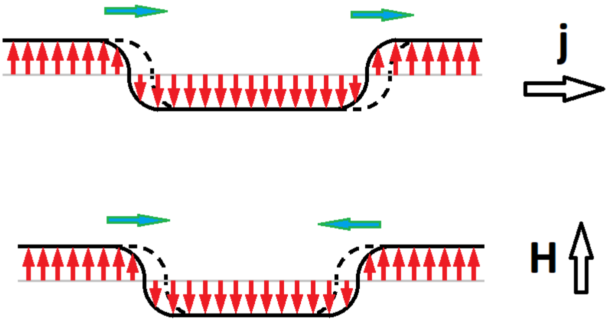

Figure 4.16: Difference between the field-induced and the current-induced DW motion.

The important difference between the field-induced and current induced DW motions is that the field moves the opposite DWs to opposite directions, as it was shown above, while the current by itself (as the adiabatic torque, so as the nonadiabatic torque) moves the DWs of the both types in one and the same direction. Therefore, we can move a "train" of DWs by current and it results in a lot of important applications (racetrack memory, spintronic memristors). For a more detailed information on the racetrack memory see Ref. [31].

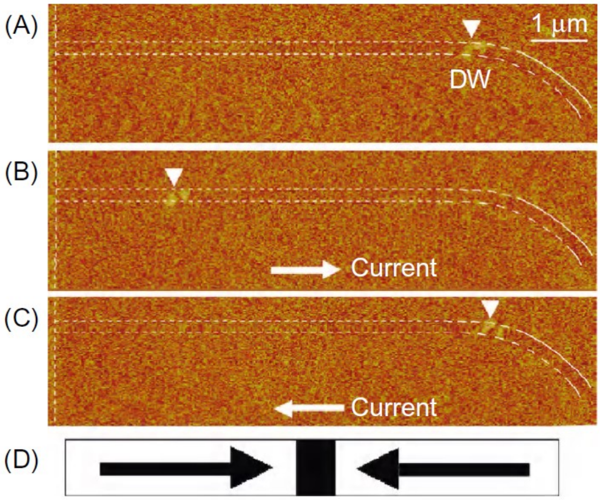

Figure 4.17: MFM image of the head-to-head DW displacement under the applied pulse current [32].

The experimental data [32] on the direct MFM imaging of the current-induced DW motion are presented in Figs. 4.17-4.19. Fig. 4.17 represents the head-to-head DW displacement under the current pulse. At $t = 0$ the position of the DW is shown in Fig. 4.17(a). After that a pulsed current was applied through the wire. The current density and the pulse duration were $7 \times 10^{11} A/m^2$ and $5 \mu s$, respectively. Fig. 4.17(b) shows the MFM image after an application of the pulsed current from left to right. The DW, which had been in the vicinity of the corner, was displaced from right to left by the application of

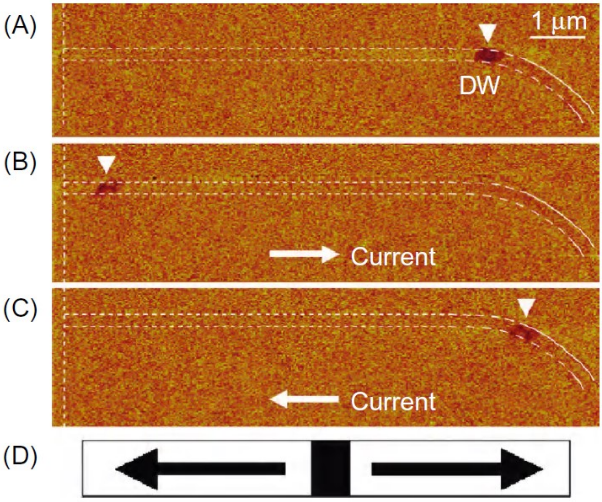

Figure 4.18: MFM image of the tail-to-tail DW displacement under the applied pulse current [32].

the pulsed current. Thus, the direction of the DW motion is opposite to the current direction. Furthermore, the direction of the DW motion can be reversed by switching the current polarity as shown in Fig. 4.17(c). These results are consistent with the spin-transfer mechanism. The same experiments for a DW with different polarities, a tail-to-tail DW, were also performed. The tail-to-tail DW is imaged as a dark contrast in Fig. 4.18. Figs. 4.18(a)-(c) show that the direction of the tail-to-tail DW displacement is also opposite to the current direction.

The average DW displacement per one pulse as a function of the pulse duration under the condition of constant current density of $7 \times 10^{11} A/m^2$ is shown in Fig. 4.19. The average DW displacement is proportional to the pulse duration, which indicates that the DW has a constant velocity of $3.0 m/s$. It was also confirmed that the DW velocity increases with the

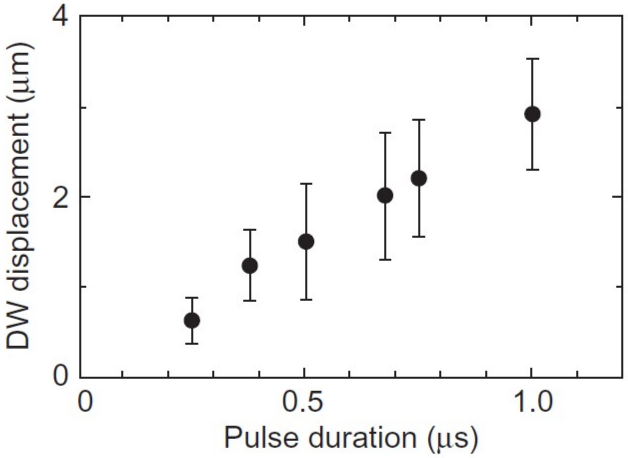

Figure 4.19: Average DW displacement per one pulse as a function of the pulse duration under a condition of constant current density [32].

current density.

Chapter 5

Spin-orbit interaction.

Spin-orbit interaction is caused by the coupling of a moving electron's spin to an effective magnetic field due to an electric field in the solid. The electric field could be either microscopic (as in an atom due to the charged nucleus) or macroscopic (due to a global electric field caused by doping in a semiconductor or band structure modulation). Either type will make a moving electron experience an effective magnetic field. The magnetic field will not appear in the laboratory frame, but will appear in the rest frame of the electron due to Lorentz transformation of the electric field.

Spin-orbit interaction is at the heart of many spin-based devices. There are essentially two types of spin-orbit interaction that we need to discuss. One is microscopic or intrinsic (as in an atom) and the other is macroscopic or extrinsic (as in a solid). The latter is usually controllable by external agents and forms the basis of many spintronic devices, but we will start by discussing microscopic spin-orbit interaction first.

5.1 Microscopic (or intrinsic) spin-orbit interaction in an atom.

5.1.1 Heuristic derivation of spin-orbit interaction.

While orbiting around the nucleus, an electron in an atom feels the electric field due to the nucleus. As a result, a magnetic field that did not exist in the laboratory frame will appear in the rest frame of the electron through a Lorentz transformation:

$$\boldsymbol{B}' = \frac{\boldsymbol{E} \times \boldsymbol{v}}{c^2\sqrt{1-(v/c)^2}} \approx \frac{\boldsymbol{E} \times \boldsymbol{v}}{c^2}, \tag{5.1}$$

where $\boldsymbol{E}$ is the electric field seen by the electron, $\boldsymbol{v}$ is its orbital velocity, and c is the speed of light in vacuum. We mark all the quantities related to the electron rest frame by prime.

The above equation is actually not entirely correct. Thomas, in a paper published in Nature in 1926, had pointed out that the Lorentz transformation that we normally use to connect the electrons rest frame to the laboratory frame is inexact. If there is a component of the electric field in a direction perpendicular to the instantaneous velocity, the electron will be accelerating perpendicular to the velocity. Therefore, it is not enough to transform the laboratory frame to the rest frame using the electrons instantaneous velocity.

Now our goal is to find heuristically the correct expression for $\boldsymbol{B}'$. Let us choose the velocity to be in the x-direction, the electric field in the y-direction and $\boldsymbol{B}'$ in the z-direction. Let us force the electron to move along a straight line (when standard Lorentz transformation will be valid) by adding a magnetic field $\boldsymbol{B} = B_z\boldsymbol{e}_z$ in the laboratory frame so that the resulting Lorentz force will balance the force due to the electric field. This results in $E_y = v_xB_z$. If the combination of the added magnetic field and the electric field are Lorentz transformed into the (non-rotating) rest frame of the electron, it results in a magnetic field

$$B'_z = \frac{B_z - E_y v_x/c^2}{\sqrt{1-(v/c)^2}}. \tag{5.2}$$

Expanding the above result in a binomial series, we get

$$B'_z = B_z + B_z\frac{v_x^2}{2c^2} - E_y\frac{v_x}{c^2} = B_z - E_y\frac{v_x}{2c^2}. \tag{5.3}$$

Generalizing to the vector form, the preceding result can be written as

$$\boldsymbol{B}' = \boldsymbol{B} + \frac{\boldsymbol{E}\times\boldsymbol{v}}{2c^2}. \tag{5.4}$$

The above magnetic field $\boldsymbol{B}'$ is the one experienced by the moving electron. If we then remove the added magnetic field $\boldsymbol{B}$ needed to convert the rotating frame to a non-rotating frame, what remains is the magnetic field experienced in a rotating frame. Therefore, we get

$$\boldsymbol{B}' = \frac{\boldsymbol{E}\times\boldsymbol{v}}{2c^2}. \tag{5.5}$$

where the Thomas's factor of 2 correction has appeared.

If we write the magnetic moment of the electron as μ_e, then the energy of its interaction with $\boldsymbol{B}'$ is

$$E_{so} = -\boldsymbol{\mu}_e\boldsymbol{B}' = -g_0\mu_B\boldsymbol{s}\boldsymbol{B}', \tag{5.6}$$

where g_0 is the gyromagnetic ratio for an electron and $\boldsymbol{s}$ is its spin.

Using Eq. (5.5), the above equation can be re-cast as

$$E_{so} = -g_0\mu_B\frac{(\boldsymbol{E}\times\boldsymbol{v})\cdot\boldsymbol{s}}{2c^2} \tag{5.7}$$

In order to derive the quantum-mechanical operator for spin-orbit interaction, we should replace $\boldsymbol{s}$ with the corresponding operator $(1/2)\boldsymbol{\sigma}$ to get

$$H_{so} = -\frac{g_0}{2}\frac{e\hbar}{2m}\frac{(\boldsymbol{E}\times\boldsymbol{v})\cdot\boldsymbol{\sigma}}{2c^2}, \tag{5.8}$$

where we have used the vector $\boldsymbol{\sigma} = (\sigma_x, \sigma_y, \sigma_z)$ composed of Pauli matrices. Since Dirac had shown that $g_0 = 2$ for a free electron in vacuum, the spin orbit interaction Hamiltonian for an atom in vacuum can also be written as:

$$H_{so} = \frac{e\hbar}{4m^2c^2}(\boldsymbol{\nabla}V\times\boldsymbol{p})\boldsymbol{\sigma}, \tag{5.9}$$

where the electric field is related to the electric potential V as $\boldsymbol{E} = -\boldsymbol{\nabla}V$.

Note that Eq. (5.5) can be written as

$$\boldsymbol{B}' = \frac{Ze\hbar\boldsymbol{l}}{8\pi\varepsilon_0 mc^2r^3}, \tag{5.10}$$

where the nuclear charge is Ze, r is the orbit radius and $\hbar\boldsymbol{l} = m\boldsymbol{r}\times\boldsymbol{v}$ is the orbital angular momentum. Substituting the above expression in Eq. (5.6), we get

$$E_{so} = -g_0\mu_B\hbar\frac{Ze}{8\pi\varepsilon_0 mc^2r^3}\boldsymbol{l}\boldsymbol{s}. \tag{5.11}$$

Finally, in the Bohr atomic model, the orbital radius of the n-th orbit is given by

$$r_n = \frac{4\pi\varepsilon_0\hbar^2n^2}{mZe^2}. \tag{5.12}$$

Substituting this in the preceding equation, we obtain

$$E_{so} = -\frac{g_0}{4}\frac{Z^4e^8m}{n^6\hbar^4c^2(4\pi\varepsilon_0)^4}\boldsymbol{l}\boldsymbol{s}. \tag{5.13}$$

The above energy depends on the scalar product $\boldsymbol{ls}$, hence the name "spin orbit interaction". Eq. (5.13) is only valid for a one-electron atom. The general form of the spin-orbit interaction energy is still given by Eq. (5.7). Note that the intrinsic spin-orbit interaction strength is proportional to the fourth power of the atomic number Z. That means electrons in atoms of lighter elements will experience weaker spin-orbit interaction. Organic semiconductors, consisting mainly of hydrocarbons, are made of light elements, and hence have weak intrinsic spin-orbit interaction. As a result, they should have large relaxation times. This has led to immense interest in "organic spintronics", which is the field of spin phenomena in organic semiconductors.

5.1.2 Strict derivation of spin-orbit interaction from the Dirac equation.

Our starting point is the Dirac equation for four-component spinors, where we assume $\boldsymbol{A} = 0$

$$i\hbar\frac{\partial\hat{\Psi}}{\partial t} = \left\{c\hat{\boldsymbol{\alpha}}\boldsymbol{p} + \hat{\beta}mc^2 + V(\boldsymbol{r})\right\}\hat{\Psi}, \tag{5.14}$$

where

$$\hat{\boldsymbol{\alpha}} = \begin{pmatrix} 0 & \boldsymbol{\sigma} \\ \boldsymbol{\sigma} & 0 \end{pmatrix}, \quad \hat{\beta} = \begin{pmatrix} I & 0 \\ 0 & -I \end{pmatrix}. \tag{5.15}$$

The relativistic energy of the particle includes also its rest energy mc^2. It should be excluded in arriving at the non-relativistic approximation: $\hat{\Psi} = \hat{\Psi}' e^{-imc^2 t/\hbar}$. In this case the Dirac equation can be written in the form:

$$\begin{gathered}[E' - V(\boldsymbol{r})]\hat{\varphi} = c(\boldsymbol{\sigma}\cdot\hat{\boldsymbol{p}})\hat{\chi} \\ \left[2mc^2 + E' - V(\boldsymbol{r})\right]\hat{\chi} = c(\boldsymbol{\sigma}\cdot\hat{\boldsymbol{p}})\hat{\varphi},\end{gathered} \tag{5.16}$$

where $E' = E - mc^2$, $\hat{\varphi}$ and $\hat{\chi}$ are two-component parts of the four-component spinor $\hat{\Psi}' = (\hat{\varphi}, \hat{\chi})$ and $\hat{\boldsymbol{p}}$ is the momentum operator.

Our goal now is to expand Eq. (5.16) up to the first order in v^2/c^2. The derivation closely follows [33]. Then from the second of Eq. (5.16) up to the first order in $(E' - V)/2mc^2$ we obtain

$$\hat{\chi} = \Big(1 - \frac{E' - V}{2mc^2}\Big)\frac{\boldsymbol{\sigma} \cdot \hat{\boldsymbol{p}}}{2mc}\hat{\varphi} \tag{5.17}$$

Substituting the above equation into Eq. (5.16) we find the separate equation for $\hat{\varphi}$:

$$[E' - V(\boldsymbol{r})]\hat{\varphi} = \frac{(\boldsymbol{\sigma} \cdot \hat{\boldsymbol{p}})}{2m}\Big(1 - \frac{E' - V}{2mc^2}\Big)(\boldsymbol{\sigma} \cdot \hat{\boldsymbol{p}})\hat{\varphi}. \tag{5.18}$$

This equation can be transformed as follows

$$\begin{gathered} E'\hat{\varphi} = H'\hat{\varphi} \\ H' = (1 - \frac{E' - V}{2mc^2}\Big)\frac{\hat{p}^2}{2m} + V + \\ \frac{\hbar\boldsymbol{\sigma}}{4m^2c^2}\big[\boldsymbol{\nabla}V \times \hat{\boldsymbol{p}}\big] - \frac{i\hbar}{4m^2c^2}\boldsymbol{\nabla}V \cdot \hat{\boldsymbol{p}}. \end{gathered} \tag{5.19}$$

In order to systematically account for all the terms of the order of v^2/c^2 we should remember that due to the four-component structure of the Dirac spinor $\hat{\varphi}$ is normalized as follows:

$$\int \rho d\tau = \int (\hat{\varphi}^\dagger\hat{\varphi} + \hat{\chi}^\dagger\hat{\chi})d\tau = \int \hat{\varphi}^\dagger\Big(1 + \frac{\hat{p}^2}{4m^2c^2}\Big)\hat{\varphi}d\tau = 1. \tag{5.20}$$

Further we use $\hat{\psi} = \hat{g}\hat{\varphi}$ instead of $\hat{\varphi}$ defined by the condition

$$\int \hat{\psi}^\dagger\hat{\psi}d\tau = \int (\hat{g}\hat{\varphi})^\dagger\hat{g}\hat{\varphi}d\tau = 1, \tag{5.21}$$

where $\hat{g} \approx 1 + \hat{p}^2/(8m^2c^2)$. Then multiplying the Schrodinger equation (5.19) by $\hat{g}$ from the left we obtain $\hat{H}\hat{\psi} = E'\psi$ with

$$H = (1 - \frac{\hat{p}^2}{4m^2c^2})\left[\hat{g}H'\hat{g}^{-1} + \frac{E'}{4m^2c^2}\hat{p}^2\right] = \frac{\hat{p}^2}{2m} + V(\boldsymbol{r}) - \frac{\hat{p}^4}{8m^3c^2} + \frac{\hbar\boldsymbol{\sigma}}{4m^2c^2}\left[\boldsymbol{\nabla}V \times \hat{\boldsymbol{p}}\right] + \frac{\hbar^2}{8m^2c^2}\nabla^2 V(\boldsymbol{r}). \qquad (5.22)$$

In Eq. (5.22) the terms in the second line represent the relativistic corrections of the order of v^2/c^2. It can be easily seen if we take into account that $\hbar\nabla V \sim \hbar V/a \sim Vp$ and $\hbar\nabla^2 V \sim \hbar^2 V/a^2 \sim p^2 V$, where a is the characteristic size of the system. The second term in the second line corresponds to the spin-orbit interaction and coincides with Eq. (5.9).

5.2 Macroscopic (or extrinsic) spin-orbit interaction in a solid.

In a solid, a quasi-free electron does not experience the strong nuclear attraction that it would have experienced in an isolated atom because the nuclear electric field is strongly screened by other electrons. Therefore, the intrinsic (or microscopic) spin-orbit interaction of the type discussed in the preceding sections should be relatively weak in a solid. This is even more true for electrons in the conduction band of direct gap semiconductors. In direct-bandgap semiconductors (e.g., GaAs, InSb, etc.) the lowest conduction band valley is at the Brillouin zone center (-valley) where the electron orbitals are nearly $|S>$-type for which $l = 0$. Hence, the $\boldsymbol{l} \cdot \boldsymbol{s}$ coupling nearly vanishes and the intrinsic spin-orbit interaction will be very weak in the conduction band. The wavefunctions of holes in the valence band are, however, more $|P>$-type orbitals for which $l \neq 0$. Hence, there is much stronger intrinsic spin-orbit interaction in the valence band of direct-bandgap semiconductors than in the conduction band.

Electrons in the conduction bands of indirect-bandgap semiconductors like silicon and germanium can experience stronger intrinsic spin-orbit interaction since the conduction band minima are at Brillouin zone edges and not at the zone center. Zone-edge electron orbital wavefunctions are not $|S>$-type, so $\boldsymbol{l} \cdot \boldsymbol{s} \neq 0$. Electrons in the conduction band of silicon, however, experience much weaker intrinsic spin-orbit interaction than those in the conduction band of germanium since silicon is the lighter element and the intrinsic spin-orbit interaction strength is proportional to the fourth power of the atomic number.

Although electrons in a solid do not experience the strong localized nuclear electric field owing to screening, they may still see a macroscopic (delocalized) electric field (or potential gradient) due to internal effects. Such an electric field could arise from an internal potential gradient (see Fig. 5.1 for an example) or because of an externally applied electric field. This electric field will cause spin-orbit interaction. This problem was examined by E. I. Rashba in 1961. The associated spin-orbit interaction bears his name (Rashba interaction) and is also some times referred to as spin-orbit interaction due to structural inversion asymmetry (SIA) since an external or internal electric field that causes this interaction breaks inversion symmetry. Another type of internal electric field may arise in a solid due to crystallographic inversion asymmetry in a crystal. This also causes spin-orbit interaction. This latter problem was examined by G. Dresselhaus in 1954 and the associated spin-orbit interaction is called by Dresselhaus interaction. It is sometimes referred to as spin-orbit interaction due to bulk inversion asymmetry (BIA) since it is caused by the lack of crystallographic inversion symmetry through the bulk of the crystal (see Fig. 5.3 for an example of the crystal structure). These two effects are sometimes called symmetry-dependent spin-orbit interactions since they require broken inversion symmetry, while the intrinsic atomic type spin-orbit interaction is called symmetry-independent spin-orbit interaction since it does not require broken inversion symmetry.

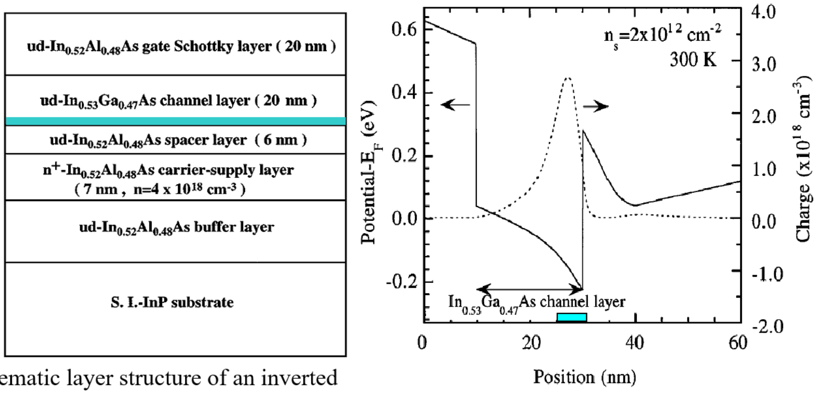

Schematic layer structure of an inverted $In_{0.53}Ga_{0.47}As$ / $In_{0.52}Al_{0.48}As$ heterostructure.
(Nitta *et al.* Phys. Rev. Lett.**78,** 1355(1997))

Calculated conduction band diagram (solid line) and electron distribution (dash line).
(Nitta *et al.* Physica E, **2,** 527(1998))

Figure 5.1: Sketch of a semiconductor heterostructure and the corresponding asymmetric confined potential (adopted from the presentation by C. S. Chu)

It is easy to see from simple symmetry considerations why in crystals with broken inversion symmetry the spin-orbit coupling is allowed by symmetry. Indeed, in a system without internal or external magnetic field time-reversal symmetry holds, i.e. changing the direction of the arrow of time will not alter the properties of the system. The transformation $t \to -t$ exchanges a particle moving with momentum $\boldsymbol{k}$ with a particle moving in $-\boldsymbol{k}$. Time reversal will also invert the precessional motion of the electron and, therefore, its spin. As a consequence, the energy of a right-moving spin-up particle will equal the energy of a left moving spin-down particle $\varepsilon(\boldsymbol{k},\uparrow) = \varepsilon(-\boldsymbol{k},\downarrow)$.

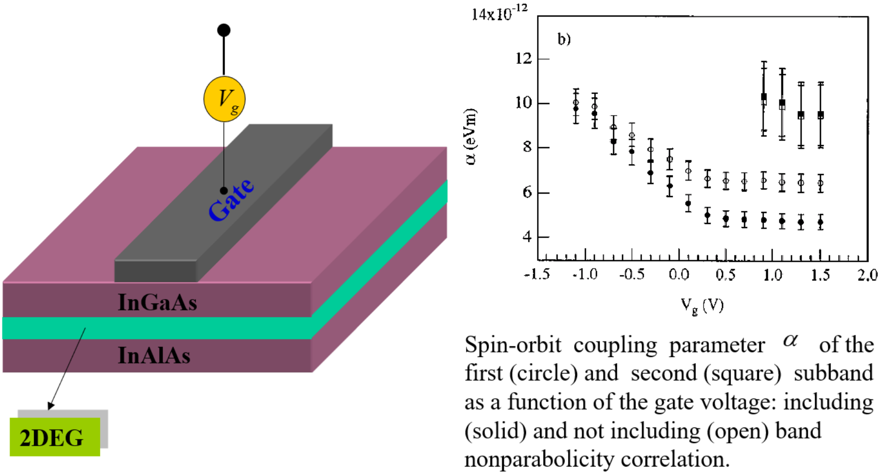

Spin-orbit coupling parameter α of the first (circle) and second (square) subband as a function of the gate voltage: including (solid) and not including (open) band nonparabolicity correlation.

(Nitta. *et al.* Phys.Rev.B **60**,7736(1999))

Figure 5.2: Tuning of the Rashba spin-orbit coupling parameter by an external electric field (adopted from the presentation by C. S. Chu)

In a crystal with inversion symmetry, additionally $\varepsilon(\boldsymbol{k}) = \varepsilon(-\boldsymbol{k})$ holds, both for spin-up and spin-down electrons. This means, that the bandstructure is symmetric around the center of the Brillouin-zone, $k = 0$, and all bands are doubly degenerate. In contrast, in crystals without inversion symmetry (for example GaAs) $\varepsilon(\boldsymbol{k}) \neq \varepsilon(-\boldsymbol{k})$ and only $\varepsilon(\boldsymbol{k},\uparrow) = \varepsilon(-\boldsymbol{k},\downarrow)$ holds. This leads to $\varepsilon(\boldsymbol{k},\uparrow) \neq \varepsilon(\boldsymbol{k},\downarrow)$, therefore the degeneracy of the bands can be lifted. This can be understood if we realize that a lack of inversion symmetry, $V(\boldsymbol{r}) \neq V(-\boldsymbol{r})$, will result in a non-vanishing potential gradient or electric field, $\boldsymbol{E}(\boldsymbol{r})$.

5.2.1 Rashba spin-orbit interaction.

As it was mentioned earlier, the Rashba-type spin-orbit interaction is due to the structural inversion asymmetry (SIA). SIA

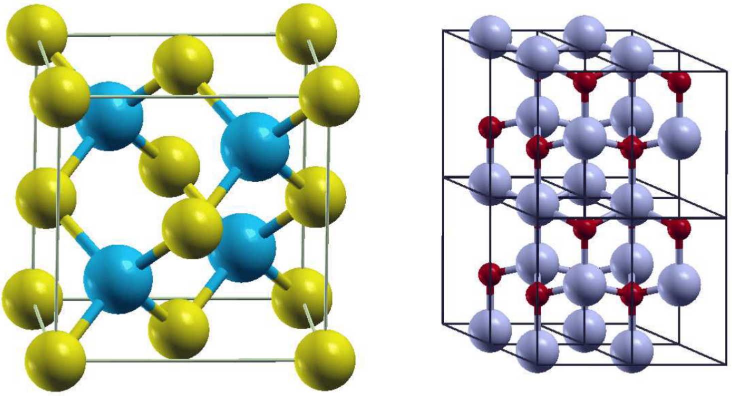

Figure 5.3: Crystal structure of GaAs (zinc blende, left) and ZnO (wurzite, right). Both structures possess no center of inversion.

typically arises at the surfaces or interfaces. An important realization of a system with Rashba-type spin-orbit coupling is a 2D electron gas (2DEG) in doped semiconductor heterostuctures, that support an electron gas at the interface between two materials, see Fig. 5.1. Another possibility to study the Rashba-effect in 2DEG are surfaces which support a surface state, e.g. in Au(111): the electrons of the surface state move in a potential gradient that is provided by the surface itself. The "bulk Rashba-effect" is also possible. In the right panel of Fig. 5.3 we can see from the ZnO lattice that it consists of bi-layers different atoms that locally create electric fields in z-direction, analogously to the situation on surfaces.

If we neglect bandstructure effects, then the Rashba interaction Hamiltonian can be obtained from Eq. (5.9) by direct analogy

$$H_R = \frac{e\hbar}{4m^{*2}c^2}(\boldsymbol{\sigma} \times \boldsymbol{p}) \cdot \boldsymbol{E} = \alpha_R \hat{c}(\boldsymbol{\sigma} \times \boldsymbol{p}), \tag{5.23}$$

where $\alpha_R = e\hbar E/(4m^{*2}c^2)$, $\boldsymbol{E}$ is the electric field and $\hat{c} =$

$\boldsymbol{E}/E$. However, band structure effects will inevitably play a role in a crystalline solid. Accounting for them results in more complex physics. For example, for A_3B_5 (GaAs,InAs,GaP,InP,...) semiconducting heterostructures the following expression for α_R was obtained [34]:

$$\alpha_R = \frac{e\hbar}{m^*}\frac{\pi\Delta_s(2E_g+\Delta_s)}{E_g(E_g+\Delta_s)(3E_g+2\Delta_s)} \tag{5.24}$$

where E_g is the band gap of the semiconductor and Δ_s is the spin-orbit splitting in the valence band.

The Rashba interaction plays an extremely important role in spintronics since this interaction can be tuned by an external electric field E (see Fig. 5.2). Therefore, it is the basis of many spintronic devices, such as the Spin Field Effect Transistor.

The Rashba spin-orbit constant can be determined experimentally, for example by Shubnikov - de Haas oscillations [35]. Fig. 5.4 represents the experimental results for Shubnikov-de Haas oscillations of the conductivity in 2DEG formed in $InP/In_{0.77}Ga_{0.23}As/InP$ quantum well. The concentration for each of the electron subbands can be found from the oscillation period according to

$$n_{2DEG} = \frac{e}{h}\frac{1}{\Delta(1/B)}, \tag{5.25}$$

where B is the perperdicular magnetic field applied to the structure and $\Delta(1/B)$ is the oscillation period in the inverse magnetic field. The $1/B$ Fourier transform of the resistance, shown in Fig. 5.5, clearly resolves a double-peak structure. The Rashba spin-orbit constant can be found from these data as $\alpha_R = (\hbar\Delta n/m^*)\sqrt{\pi/(2(n-\Delta n))}$. The results for the Rashba constant are presented in Fig. 5.6.

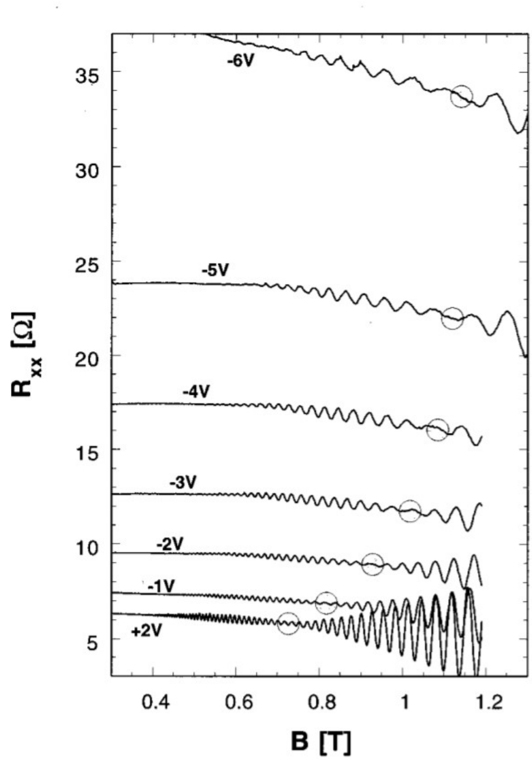

Figure 5.4: Shubnikovde Haas oscillations at a temperature of 0.3 K with the gate voltage changed as a parameter. Data are taken from [35].

5.2.2 Dresselhaus spin-orbit interaction.

The Dresselhaus type of spin-orbit interaction arises due to crystallographic inversion asymmetry in a crystal that results in an effective electric field. This interaction will be absent in a centro-symmetric crystal like silicon or germanium, which do not have crystallographic inversion asymmetry in any direction. That is why the Dresselhaus interaction is sometimes referred to as spin-orbit interaction due to bulk inversion asymmetry (BIA).

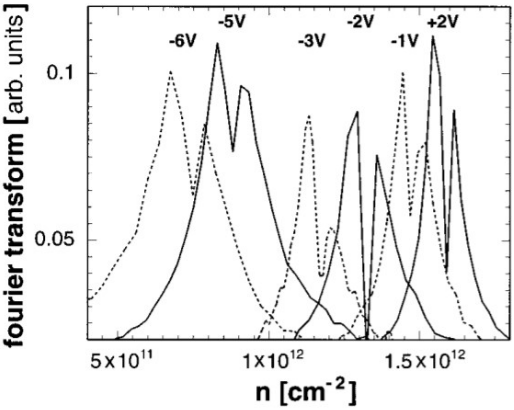

Figure 5.5: Fourier transform taken from the SdH oscillations of Fig. 5.4. Data are taken from [35].

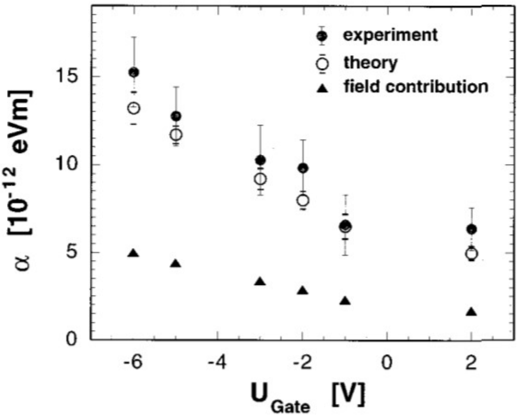

Figure 5.6: Values of the spin-orbit coupling parameter α_R given by experiment and theory. Data are taken from [35].

It was shown that for zincblende $A_{III}B_V$ lattice the spin-orbit contribution to the hamiltonian takes the form:

$$H_D = D\boldsymbol{\Omega}(\boldsymbol{k})\boldsymbol{\sigma},$$
$$\boldsymbol{\Omega} = (k_x(k_y^2 - k_z^2), k_y(k_z^2 - k_x^2), k_z(k_x^2 - k_y^2)) \tag{5.26}$$

If we consider (001) surface(interface) of $A_{III}B_V$ semiconductor, than $\langle k_z \rangle = 0$, $\langle k_z^2 \rangle \sim 1/d^2$ and

$$\langle \boldsymbol{\Omega} \rangle = (\underbrace{k_x k_y^2}_{cubic \to 0} - k_x \langle k_z^2 \rangle, k_y \langle k_z^2 \rangle - \underbrace{k_y k_x^2}_{cubic \to 0}, 0) =$$
$$\langle k_z^2 \rangle (-k_x, k_y, 0). \tag{5.27}$$

Therefore,

$$H_D = \beta(k_y \sigma_y - k_x \sigma_x). \tag{5.28}$$

5.3 Magneto-electric subbands

Consider a two-dimensional electron gas (2-DEG) such as the one encountered at the interface of a heterostructure or a quantum well. Fig. 5.1 shows such a system. We will assume that there is a symmetry-breaking electric field E_y along the y-axis that induces a Rashba spin-orbit interaction. This electric field could be caused by the structural asymmetry, or could be applied from outside by attaching a gate electrode. In addition to the Rashba interaction, there is also the Dresselhaus interaction accruing from bulk (or crystallographic) inversion asymmetry. Finally, there is also an external magnetic field inducing the Zeeman interaction. Our intention is to derive the dispersion relation (relation between electron kinetic energy and wavevector) in this two-dimensional system. We will also derive the eigenspinors (or spin eigenstates) at any given wavevector in a given subband. Since the boundaries of the quantum confined structure restrict motion in the direction perpendicular to the boundary, and the external magnetic field also constrains the electrons motion by forcing it into closed Landau orbits, the electron experiences both electrostatic and magnetostatic confinement. This discretizes the allowed energies, breaking it up into discrete subbands. They are called magneto-electric subbands since they are due to the combined effect of electrostatic and magnetostatic confinements.

5.3.1 In-plane magnetic field

Let us consider the situation when there is a magnetic field in the plane of the 2-DEG. In this case, the magnetic flux density is given by $\boldsymbol{B} = B_x\hat{x} + B_z\hat{z}$ since the 2-DEG is in the (x, z)-plane. We choose the gauge $\boldsymbol{A} = y(-B_z\hat{x}+B_x\hat{z})$. The effective mass Hamiltonian describing the 2-DEG can be written in the form

$$H_{2-DEG} = \frac{1}{2m^*}\Big[(p_x - eB_zy)^2 + p_y^2 + (p_z + eB_xy)^2\Big] + V(y) - \frac{g}{2}\mu_B(B_x\sigma_x + B_z\sigma_z) + \alpha_R\Big[(p_x - eB_zy)\sigma_z - (p_z + eB_xy)\sigma_x\Big] + \beta\Big[(p_x - eB_zy)\sigma_x - (p_z + eB_xy)\sigma_z\Big], \quad (5.29)$$

where $V(y)$ is the confining potential in the y-direction (including the effect of the y-directed electric field causing the Rashba interaction). The terms in the second and third line are spin dependent terms since they involve the Pauli spin matrices. Note that the first of these spin-dependent terms is the Zeeman interaction, the second is the Rashba interaction, and the last is the Dresselhaus interaction. To find the energy dispersion relations in this 2-DEG and the 2-component wavefunction for the spin eigenstates, we have to solve the equation

$$H_{2-DEG}\psi_{2-DEG}(x, y, z) = E\psi_{2-DEG}(x, y, z). \quad (5.30)$$

Since the Hamiltonian is invariant in x and z, the wavevectors k_x, and k_z are good quantum numbers and we can write the

2-component wavefunction as

$$\psi_{2-DEG}(x,y,z) = \frac{1}{\sqrt{L_x L_z}} e^{ik_x x} e^{ik_z z} \lambda_0^n(y) \begin{pmatrix} \kappa_1 \\ \kappa_2 \end{pmatrix}, \quad (5.31)$$

where $(1/L_x L_z) \int \int dxdz = 1$. We assume that the width of the 2-DEG is so narrow that the subbands are well separated in energy. As a result, we can ignore subband mixing. Then the Schrodinger equation (after multiplying by $\lambda_0^{n*}(y)$, integrating over y and assuming $\langle y \rangle = \int dy \lambda_0^{n*}(y) y \lambda_0^n(y) = 0$) takes the form (below we assume $\hbar = 1$):

$$\Big\{ \epsilon_n + \frac{(k_x^2 + k_z^2)}{2m^*} - \frac{g}{2}\mu_B(B_x\sigma_x + B_z\sigma_z) + \alpha_R \Big[k_x\sigma_z - k_z\sigma_x \Big] + \beta \Big[k_x\sigma_x - k_z\sigma_z \Big] \Big\} \begin{pmatrix} \kappa_1 \\ \kappa_2 \end{pmatrix} = E_n \begin{pmatrix} \kappa_1 \\ \kappa_2 \end{pmatrix}, \quad (5.32)$$

where ϵ_n is the energy of the n-th quantized transverse mode, which is to be found from

$$\Big[-\frac{1}{2m^*}\frac{\partial^2}{\partial_y^2} + \frac{e^2 y^2 (B_x^2 + B_z^2)}{2m^*} + V(y) \Big] \lambda_0^n(y) = \epsilon_n \lambda_0^n(y) \quad (5.33)$$

In order to find the spin-dependent energy eigenstates E_n (as a function of k_x, and k_z) for the n-th magneto-electric subband, as well as the corresponding eigenspinors, we have to diagonalize the Hamiltonian Eq. (5.32), meaning that we must find its eigenvalues and eigenfunctions. Since we have a 2×2 matrix, there are two eigenvalues and two corresponding eigenfunctions. The two eigenvalues are the spin-dependent eigenenergies, and the two eigenfunctions are the eigenspinors. We find that the eigenvalues in the n-th subband are

$$E_n^{\pm} = \frac{k_x^2 + k_z^2}{2m^*} + \epsilon_n \pm \sqrt{(\frac{g}{2}\mu_B B_z - \alpha_R k_x + \beta k_z)^2 + (\frac{g}{2}\mu_B B_x + \alpha_R k_z - \beta k_x)^2}. \quad (5.34)$$

The corresponding eigenspinors are:

$$\psi^{+} = \begin{pmatrix} \kappa_1^{+} \\ \kappa_2^{+} \end{pmatrix} = \begin{pmatrix} -\sin\theta_k \\ \cos\theta_k \end{pmatrix} \tag{5.35}$$

and

$$\psi^{-} = \begin{pmatrix} \kappa_1^{-} \\ \kappa_2^{-} \end{pmatrix} = \begin{pmatrix} \cos\theta_k \\ \sin\theta_k \end{pmatrix}, \tag{5.36}$$

where

$$\theta_k = \frac{1}{2}\arctan\left[\frac{(g/2)\mu_B B_x + \alpha_R k_z - \beta k_x}{(g/2)\mu_B B_z - \alpha_R k_x + \beta k_z}\right]. \tag{5.37}$$

Note that at any given wavevector state (k_x, k_z), the two eigenspinors are orthogonal, which means that the corresponding spins are anti-parallel. The angle θ_k, however, depends on the wavevector components k_x and k_z, and is independent of the subband index n. Because of the wavevector dependence of the eigenspinors, neither spin-split level whose energy dispersion relation is given by Eq. (5.34) has a fixed spin quantization axis. The spin quantization axis, or the spin polarization in any level, changes with changing wavevector. We can find this spin quantization axis (spin polarization) easily. Let S_n be the component of spin polarization along the n-axis. Then

$$S_n^{\pm} = \frac{1}{2}\psi^{\pm\dagger}(\boldsymbol{\sigma}\boldsymbol{n})\psi^{\pm}. \tag{5.38}$$

Therefore, the spin of the electron with wave vector $\boldsymbol{k} = (k_x, 0, k_z)$, which is in the eigen states Eqs. (5.35)-(5.36) lies in (x, z)-plane and makes the angle $\varphi = 2\theta_k + \pi$ ($\varphi = 2\theta_k$) with the z-axis.

In Fig. 5.7 we plot the energy versus wavevector relations for the lowest magneto-electric subband ($n = 1$). Each magneto-electric subband is spin-split into two levels. The lower one has inflections along lines $k_x = 0$ and $k_z = 0$, whereas the upper one is nearly a paraboloid.

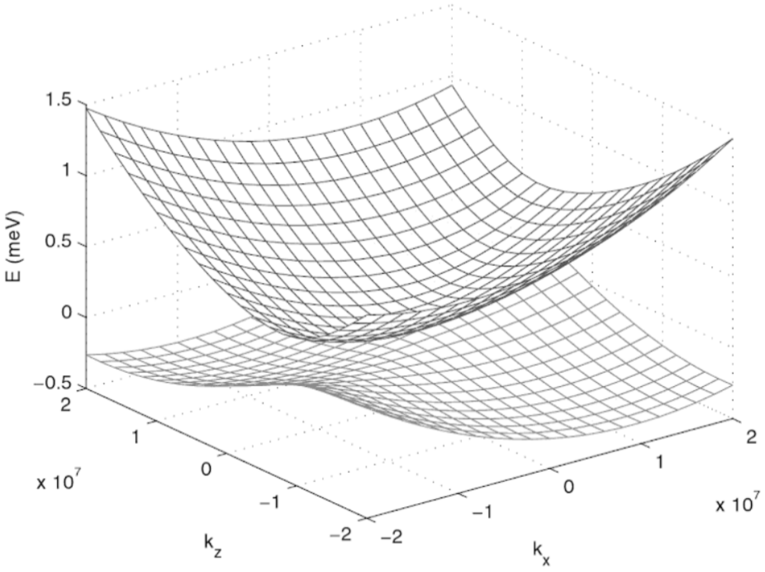

Figure 5.7: Energy dispersion relation of spin-split levels in the lowest subband in a two dimensional electron gas subjected to a magnetic field in the plane of the gas. We assumed $m^* = 0.05m_0$, $g = 4$, $B = 1$ Tesla, $\alpha_R = 10^{11}$ eV-m, $\beta = 2\alpha_R$. The wavevectors are in units of cm^{-1}. (adopted from [15])

5.3.2 Special case: no magnetic field, no Dresselhaus SO interaction.

This is a situation that arises in the discussion of the intrinsic spin Hall effect visited later. For this case, $\tan 2\theta_k = -k_z/k_x$, so that $\sin 2\theta_k = -k_z/k$ and $\cos 2\theta_k = k_x/k$, where $k = \sqrt{k_x^2 + k_z^2}$. It can be easily seen that the spin of the eigen states makes the right angle with its momentum. The energies of the spin-split levels and the corresponding spin polarizations at the Fermi surface are presented in Fig. 5.8

In more general case when the both Rashba and Dressel-

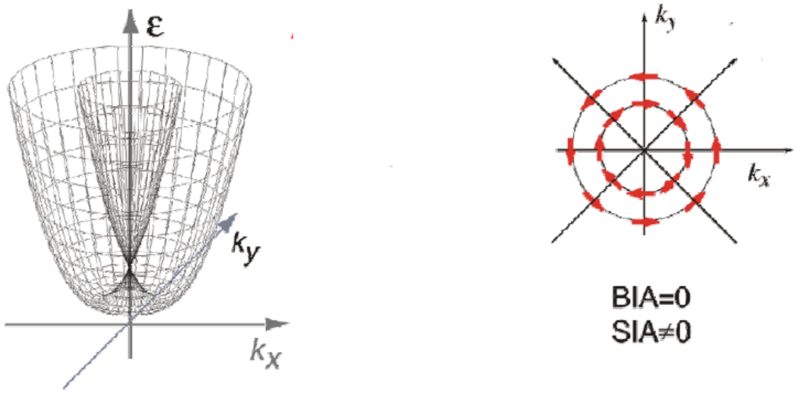

Figure 5.8: Left: spin-split subbands at zero magnetic field for the case of Rashba SO coupling. Right: spin structure of the eigen states at the Fermi level $\varepsilon = \varepsilon_F$ (adopted from the presentation by D. Weiss).

haus spin-orbit interactions are present in the system, the corresponding energies of the spin-split levels and spin polarizations at the Fermi surface are presented in Fig. 5.9.

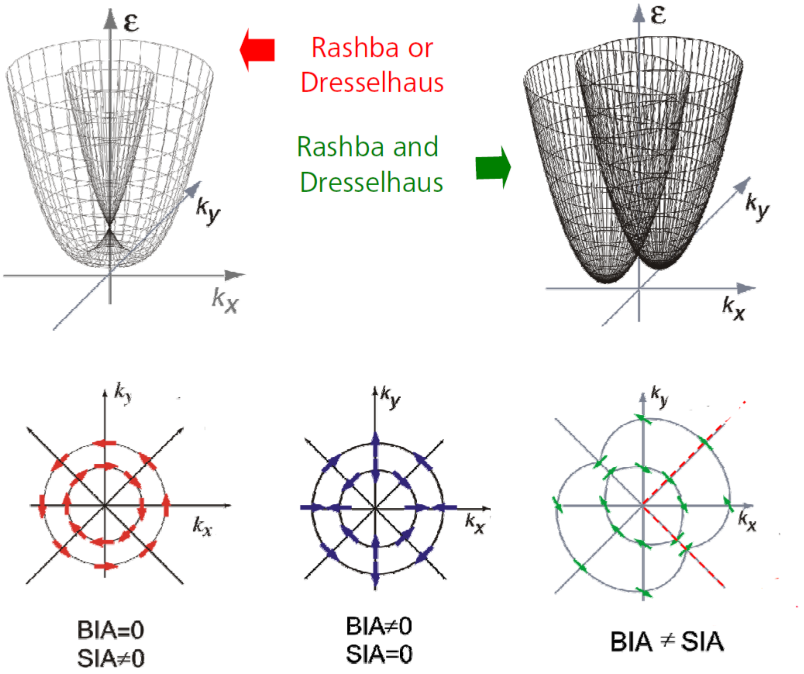

Figure 5.9: Upper row: spin-split subbands at zero magnetic field. Bottom row: spin structure of the eigen states at the Fermi level $\varepsilon = \varepsilon_F$ (adopted from the presentation by D. Weiss).

Chapter 6

Some SO-related spin phenomena.

6.1 The spin Hall effect.

With the advent of spintronics, a plethora of Hall effects have come to the fore, which we discuss next.

Normal Hall effect. The normal Hall effect considers a solid structure subjected to a magnetic field in the z-direction. An electric field is applied in the x-direction that causes an electron in the solid to accelerate in the x-direction. However, scattering causes a frictional force, proportional to the electron velocity, which opposes the force due to the electric field. When the two forces balance, the electron reaches a constant velocity known as the drift velocity. In the steady state, the electron drifts along the x-direction with this constant velocity v_{drift}. The z-directed magnetic field exerts a Lorentz force on the electron which pushes it in either the $+y$-direction or y-direction depending on the direction of the magnetic field. If the sample has boundaries in the y direction, then electrons will pile up at one edge, causing a charge imbalance between this edge and the opposite edge. This charge imbalance will cause an associated potential difference. This is the Hall voltage and this effect is the celebrated Hall effect predicted by Edwin Hall in 1879. It is routinely used today in semiconductor characterization to ascertain carrier concentration in a sample or its polarity (p-type or n-type). The sign of the Hall voltage depends on the polarity of charge carriers (whether they are electrons or holes). Its magnitude is inversely proportional to the carrier concentration and directly proportional to the magnetic field.

Anomalous Hall effect. In a ferromagnet, there can be an additional contribution to the Hall voltage that arises without any external magnetic field. Because of spin-dependent band structure or spin-dependent scattering events due to spin-orbit coupling, electrons whose spins are polarized in the, say, $+z$-direction, are scattered to one edge of the sample and electrons whose spins are polarized in the $-z$-direction are scattered to the other edge. Since the material is a ferromagnet, there are majority and minority spins, meaning that there can be more electrons with $+z$-polarized spins than $-z$-polarized spins. In that case, more electrons are scattered towards one edge than the other, leading once again to a charge imbalance between these two edges and a resulting Hall voltage. This Hall voltage does not require a magnetic field to be produced. This is the so-called anomalous Hall effect, whose existence is often used as proof of ferromagnetism in materials. Note that, not only a charge imbalance exist between the two edges, but a spin imbalance exists as well. Therefore, both a charge current and a spin current can flow between the two edges.

Quantum Hall effect. The quantum Hall effect is a well-known phenomenon in a two-dimensional electron gas subjected to a transverse magnetic field at low temperatures. The longitudinal resistance of the electron gas vanishes and the transverse resistance (or Hall resistance) exhibits plateaus at certain values of the magnetic feld, the plateau resistance being quantized to h/e^2. This happens due to the formation of well-defined Landau levels and edge states that carry current.

Quantum anomalous Hall effect. A similar phenomenon can occur without a magnetic field in a two-dimensional ferromagnetic insulator. In the limit of vanishing spin-orbit coupling (that couples the majority and minority spins) and large enough exchange splitting that separates the majority and minority spin bands in a ferromagnet, the majority spin band will be completeley full and the minority spin band completely empty at low temperatures. When the exchange splitting is gradually reduced, the two bands intersect each other in wavevector space, leading to band inversion. The energy degeneracy at the intersection point can be removed by turning on the spin-orbit coupling, leading to the formation of an energy gap. When the Fermi level is in this gap, the 2-DEG is insulating since the density of states at the Fermi level is zero. Such an insulator, also known as a Chern insulator, should exhibit a quantized anomalous Hall resistance of h/e^2 and zero longitudinal resistance when the Fermi level is placed within the gap. The quantized anomalous Hall effect was experimentally demonstrated in the magnetic topological insulator Cr-doped (Bi,Sb)2Te3 whose surface behaves like a two-dimensional ferromagnet. The longitudinal and anomalous Hall resistances were measured in the absence of any magnetic field. The Fermi level was varied by applying a potential to the topological insulator with a gate terminal. At certain values of the gate voltage (which corresponded to placing the Fermi level in the gap), the longitudinal resistance nearly vanished and the anomalous Hall resistance exhibited a plateau quantized to h/e^2, indicating the formation of the quantum anomalous Hall state.

Therefore, all the known manifestation of the Hall effect can be classified as normal (including quantum Hall effect),

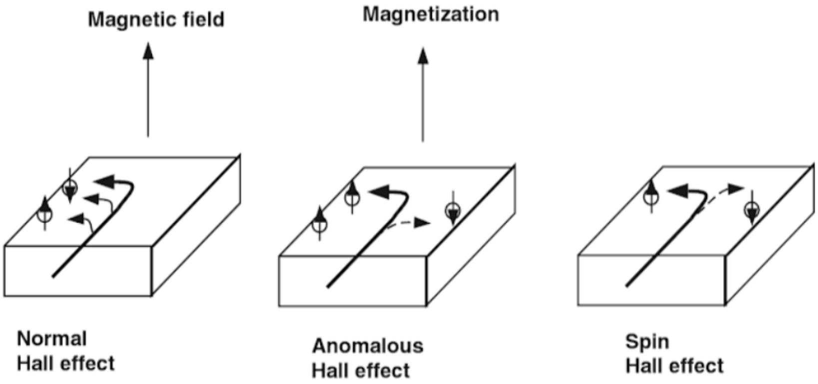

Figure 6.1: Different types of the Hall effect (not quantum version). Adopted from [15].

anomalous (including quantum anomalous) and spin (including quantum spin Hall effect) Hall effects. Their physical essence is demonstrated pictorically in Fig. 6.1.

6.1.1 Extrinsic spin Hall effect.

There are two types of Spin Hall effect: extrinsic and intrinsic. The extrinsic effect arises from spin-dependent scattering, much like the anomalous Hall effect. A spin-unpolarized current flowing into a paramagnetic semiconductor slab in the absence of any magnetic field will inject electrons into the slab with spins pointing up and down with respect to the slabs plane, as shown in the far right figure of Fig. 6.1. Spin dependent scattering will deflect spin-up electrons to one side of the slab and spin-down electrons to the other side, resulting in a spin imbalance between the right and left edges of the slab. Therefore, a spin current will flow between the two edges just as in the case of the anomalous Hall effect. However, since the material is not a ferromagnet and the current injected is not spin-polarized, there are equal numbers of spin-up and spin-down electrons in the slab. The result is that the number of spin-up electrons piling up at one edge is equal to the number of spin-down electrons piling up at the other edge. Therefore, there is no charge imbalance between the two edges and hence no charge current flows, unlike in the case of the anomalous Hall effect.

If one assumes that the elastic scatterers in the paramagnet are spinless and described by a scattering potential of the form

$$V = V_c(\boldsymbol{r}) + V_s(\boldsymbol{r})\boldsymbol{\sigma}\boldsymbol{L}, \tag{6.1}$$

where $\boldsymbol{\sigma}$ and $\boldsymbol{L}$ are the spin and orbital angular momentum operators of an electron scattered by the scatterer, the scattered beam will be spin-polarized with a polarization vector given by [36]

$$\boldsymbol{S} = \frac{fg^* + gf^*}{|f|^2 + |g|^2}\hat{n}, \tag{6.2}$$

where $\hat{n}$ is a unit vector perpendicular to the scattering plane defined by the initial and final wavevectors of the electron (before and after scattering), while f and g are the spin-independent and spin-dependent parts of the scattering amplitude.

The Spin Hall voltage generated due to spin-up electrons can be written in analogy to the anomalous Hall effect:

$$V_{\uparrow,\downarrow} = R_s W J_x n_{\uparrow,\downarrow} \mu_B, \tag{6.3}$$

where W is the width of the slab, J_x is the magnitude of the (x-directed) current density flowing through the slab, $n_{\uparrow,\downarrow}$ is the density of spin-up (spin-down) electrons, and μ_B is the Bohr magneton. In Fig.6.1, spin-up electrons will be flowing to the left and spin-down electrons to the right. These two spin current components add and hence the total Spin Hall voltage will be [37]

$$V_{SH} = R_s W J_x (n_\uparrow + n_\downarrow)\mu_B = R_s W J_x n \mu_B. \tag{6.4}$$

If we connect the two edges of the sample by a transverse metal strip the spin current is given by $J_\uparrow + J_\downarrow = V_{SH}/\rho W$, where ρ is the resistivity of the sample per spin subband. The ratio of the spin current to the charge current (sometimes referred to as the Spin Hall angle) is therefore

$$\theta_{SH} = \frac{J_{spin}}{J_{charge}} = \frac{J_\uparrow + J_\downarrow}{J_x} = \frac{R_s n \mu_B}{\rho}. \tag{6.5}$$

Note that the spin current is dissipationless. The electric field $\boldsymbol{E}$ causing the charge current injection must be collinear with the charge current and is hence perpendicular to the spin current $\boldsymbol{J}_{spin}$. As a result, $\boldsymbol{J}_{spin} \cdot \boldsymbol{E} = 0$, so the spin current does not dissipate any energy. The Spin Hall voltage of course cannot be measured with a voltmeter since there is no voltage difference between the two sides. The electrochemical potentials of the spin-up electrons at the two edges are different as are the electrochemical potentials for the spin-down electrons, but the total electrochemical potentials at the two edges are the same. However, if we connect the two edges with a conductor of width w to allow spin-up electrons to flow to the left and spin-down electrons to flow to the right, then something remarkable happens.

The same spin-dependent scatterers will deflect the left-flowing spin-up electrons toward one side and right-flowing spin-down electrons to the same side. In other words, electrons accumulate on one side and deplete on the other. Therefore, a charge imbalance will build up at the two edges of the conductor, as shown in Fig. 6.2, and the resulting potential drop can be measured with a voltmeter! These voltages have

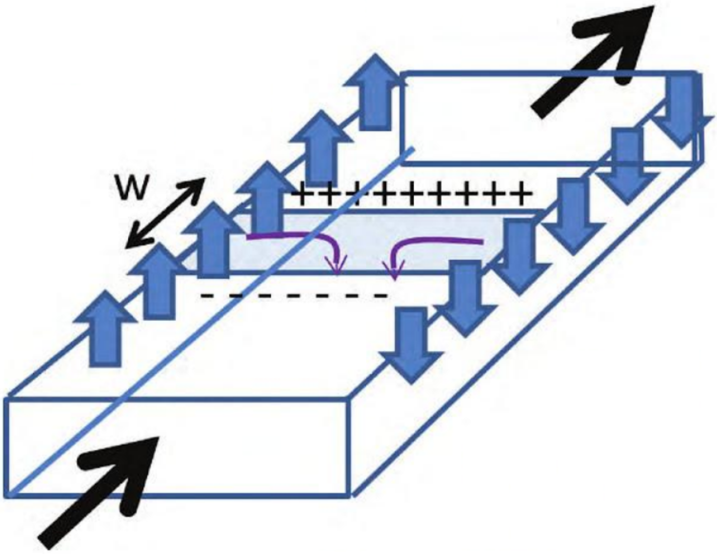

Figure 6.2: Inverse spin Hall effect. Adopted from [15].

been experimentally measured. This effect is called the inverse Spin Hall effect. The electric field associated with the potential drop is given by [37]

$$\boldsymbol{E}_{ISH} = \theta_{SH}\rho[\boldsymbol{J}_{spin} \times \boldsymbol{\nu}], \tag{6.6}$$

where $\boldsymbol{\nu}$ is the unit vector directed along the spin polarization of the spin current $\boldsymbol{J}_{spin}$.

6.1.2 Intrinsic spin Hall effect.

The intrinsic Spin Hall effect is an intriguing phenomenon that takes place in a two-dimensional electron gas in ballistic transport (no scattering, whether spin-dependent or spin-independent), provided there is spin-orbit interaction, such as the Rashba effect, which can exist in the 2-DEG. To an observer, there is no difference between the extrinsic and intrinsic

Spin Hall effect; when a charge current is injected in the plane of the 2-DEG, a dissipationless spin current (consisting of spins polarized perpendicular to the plane of the 2-DEG) flows in the plane of the 2-DEG in a direction perpendicular to the charge current. However, it is not caused by spin-dependent scattering deflecting opposite spins to opposite sides. Instead, it is caused by the Rashba spin-orbit interaction.

Our consideration closely follows [38]. Let's consider a 2D electron gas in the (x, y)-plane. The hamiltonian of the system takes the form

$$H = \frac{\hat{p}^2}{2m} + V(\boldsymbol{r}) + \alpha_R \hat{z}[\boldsymbol{\sigma} \times \hat{\boldsymbol{p}}], \tag{6.7}$$

where $\hat{\boldsymbol{p}} = \hat{p}_x \hat{x} + \hat{p}_y \hat{y}$.

We can operate with the Rashba SO interaction in terms of the so-called spin-dependent Rashba effective magnetic field

$$\boldsymbol{B}_R = \frac{2\alpha_R}{g\mu_B}[\hat{\boldsymbol{p}} \times \hat{z}]. \tag{6.8}$$

The dynamics of an averaged electon spin is described by

$$\frac{d\boldsymbol{S}}{dt} = \frac{g\mu_B \boldsymbol{B}_R}{\hbar} \times \boldsymbol{S} \tag{6.9}$$

or equating each component separately

$$\frac{dS_x}{dt} = \frac{g\mu_B B_{Ry}}{\hbar} S_z = -2\alpha_R k_x S_z \tag{6.10}$$

$$\frac{dS_y}{dt} = -\frac{g\mu_B B_{Rx}}{\hbar} S_z = -2\alpha_R k_y S_z \tag{6.11}$$

$$\frac{dS_z}{dt} = \frac{g\mu_B}{\hbar}(B_{Rx} S_y - B_{Ry} S_x) = 2\alpha_R(k_x S_x + k_y S_y) \tag{6.12}$$

From Eq. (6.8) we see that the magnetic field in our 2-DEG lies entirely in the plane of the 2-DEG and has no z-component. Since in the presence of dissipation the electron spins must align parallel or anti-parallel to the magnetic field, we conclude that the electron spins in the 2-DEG will have no z-component and $S_z = 0$. Consider now the situation when an electric field E_x is applied in the positive x-direction at time $t = 0$. This field will induce a drift of electrons in the x-direction. We will show that three things result from this drift: (1) the spins develop a z-component; (2) $+z$-polarized and $-z$-polarized spins accumulate at opposite edges of the 2-DEG, causing a spin imbalance between the edges and hence a spin-current flow along the y-direction; and (3) the ratio of the spin current density to the electric field (i.e., the spin-Hall conductivity) is a universal constant. This is the intrinsic Spin Hall effect.

Let us focus on an electron with initial wavevector $\boldsymbol{k}_0$ at time $t = 0$ and define a new set of coordinate axes (the primed coordinates) such that the y'-axis coincides with $\boldsymbol{k}_0$. Let the y'-axis subtend an angle ϕ with the y-axis. At $t = 0$, $\boldsymbol{B}_R(t = 0)$ is along the x' direction, since it is perpendicular to $\boldsymbol{k}_0$ and $\hat{z}$. Since $B_{Rx'} \neq 0$ and $B_{Ry'} = 0$, $S_{x'} = \mp\hbar/2$ in the lower (upper) spin subband, while $S_{y'} = S_z = 0$. The application of the electric field along the x-direction will change $\boldsymbol{B}_R$ since it will accelerate the electron and change $\boldsymbol{k}$. We will assume that the electric field is weak and find solution of Eqs. (6.12) to the linear order in the electric field. Assuming that $dS_z/dt = 0$ we obtain:

$$S_{x'} \approx \pm\frac{\hbar}{2} \tag{6.13}$$

$$S_{y'} = \pm\frac{\hbar}{2}\frac{B_{Ry'}}{B_{Rx'}}, \tag{6.14}$$

$$S_z(t = +0) = \mp\frac{\hbar}{g\mu_B}\frac{1}{B_{Rx'}}\frac{d(B_{Ry'}/B_{Rx'})}{dt}\bigg|_{t=+0}\frac{\hbar}{2}. \tag{6.15}$$

Now recall that at $B_{Ry'}/B_{Rx'} = -k_{x'}/k_{y'}$. Therefore from

Eq. (6.15) it follows

$$S_z(t) = \pm\frac{\hbar^2}{2g\mu_B B_{Rx'}}\frac{k_y}{k^2}\frac{dk_x}{dt}\bigg|_{t=+0} = \pm\frac{e\hbar}{2g\mu_B B_{Rx'}}\frac{k_y}{k^2}E_x. \quad (6.16)$$

In the last equation we have used the Newton's law $d(\hbar k_x)/dt = -eE_x$. Expressing $B_{Rx'} \approx B_R$ via α_R we obtain:

$$S_z(t=+0) = \pm\frac{\hbar e}{4\alpha_R}\frac{k_y}{k^3}E_x. \quad (6.17)$$

As $k_y(t) = const = k_{y,0}$ if the electric field is applied along the x-axis and $\dot{k} \propto E$, we indeed have $dS_z/dt = 0$ up to the linear order in E.

Eq. (6.17) is instructive. Note that even though there would have been no z-component of the spin in the 2-DEG in the absence of the electric field (because $\boldsymbol{B}_R$ would have been entirely in the x-y plane), a z-component develops when the electric field is present and it is directly proportional to the strength of the field. It is also inversely proportional to the strength of the spin-orbit interaction. A stronger spin-orbit interaction would have resulted in a stronger $\boldsymbol{B}_R$ in the plane of the 2-DEG, tending to keep the spin polarization constrained to the plane of the 2-DEG and decreasing the z-component of spin. That is the physics. Let us now examine if there is any y-directed spin current density $J_{sy}(t)$ due to the z-component of the spins at temperature $T \to 0$.

The operator for the y-component of the z-polarized spin current density is

$$\hat{j}^z_{sy} = \frac{1}{2}\{\hat{\sigma}_z, \hat{v}_y\} = \frac{1}{2}\{\hat{\sigma}_z, \frac{\partial \hat{H}}{\partial p_y}\} = \frac{p_y}{m^*}\hat{\sigma}_z. \quad (6.18)$$

Consequently, the contribution to the y-component of the z-polarized spin current density from a wavevector state $\boldsymbol{k}$ in either spin-split band is $J^z_{sy\pm}(\boldsymbol{k}) = S^{\pm}_z(\boldsymbol{k})(\hbar k_y/m^*)$. Therefore, the y-directed spin current density due to z-polarized spin at time $t = \tau$ is

$$J_{sy}^{z}(\tau) = J_{sy}^{z+} + J_{sy}^{z-}, \tag{6.19}$$

where J_{sy}^{z+} and J_{sy}^{z-} are the upper and lower spin subband current densities, which are to be calculated as:

$$J_{sy}^{z\pm} = \frac{1}{4\pi^2} \int_0^{2\pi} \int_0^{k_{F\pm}} d\phi k dk \frac{\hbar k_y}{m^*} S_z^{\pm}(\boldsymbol{k}) = \pm \frac{e\hbar}{16\pi m^* \alpha^R} E_x k_{F\pm}. \tag{6.20}$$

Therefore

$$J_{sy}^{z}(\tau) = \frac{e}{8\pi} E_x. \tag{6.21}$$

This result shows that a spin-current due to z-polarized spins flowing in the y-direction exists, which means that $+z$ and $-z$-polarized spins accumulate at opposite edges of the sample due to the combined actions of the spin-orbit interaction and the electric field causing drift (or the charge current resulting from this drift). This is the intrinsic spin-Hall effect, which does not require spin-dependent scattering at all, unlike the extrinsic spin-Hall effect. The spin Hall conductivity is:

$$\sigma_{SH} = \frac{J_{sy}}{E_x} = \frac{e}{8\pi}. \tag{6.22}$$

Note that the Spin Hall conductivity depends only on the universal constant e, which is the charge of the electron. Hence the name "universal" intrinsic Spin Hall effect.

In fact, further it was demonstrated [39] that the universal spin Hall conductivity vanishes in a finite system due to the nonequilibrium spin accumulation arising in the system with spin-orbit coupling simultaneously with the described effect. The universal value of the spin Hall conductivity obtained here is restored under the ac applied electric field in the limit of large frequencies when the spin accumulation is effectively averaged over time.

6.2 The spin galvanic effect.

In a spin polarized two-dimensional electron gas (2-DEG), spin relaxing scattering can cause strange effects in the presence of spin-orbit interaction. One example is the Spin Galvanic effect (inverse magnetoelectric effect, inverse Edelstein effect), where an electric current can flow without a battery. Electric current is usually generated by (i) electric and/or magnetic fields (drift current), or (ii) a spatial gradient of carrier concentration (diffusion current) or (iii) temperature (thermogalvanic current). In an electron gas with nonequilibrium spin distribution, an electric current can be generated without any electric/magnetic fields or without a concentration and thermal gradients. This is the Spin Galvanic effect.

Assume that the spin polarization is created in the material by optical or electrical means. Microscopically this net spin polarization is provided by the nonequilibrium spin-imbalance population in the spin-split subbands. An example of such a spin imbalance is demonstrated in Fig. 6.3(b), which represents the dispersion relations for (110)-grown zinc-blende quantum well. In this case each of the parabolas has a fixed spin direction. For the case of Rashba spin-orbit coupling the dispersion parabolas have no fixed quantization axis, but the general statement that the spin polarization is provided by the spin imbalance is still valid.

For (110)-grown zinc-blende presented in Fig. 6.3 as long as the carrier distribution is symmetric around the minima of

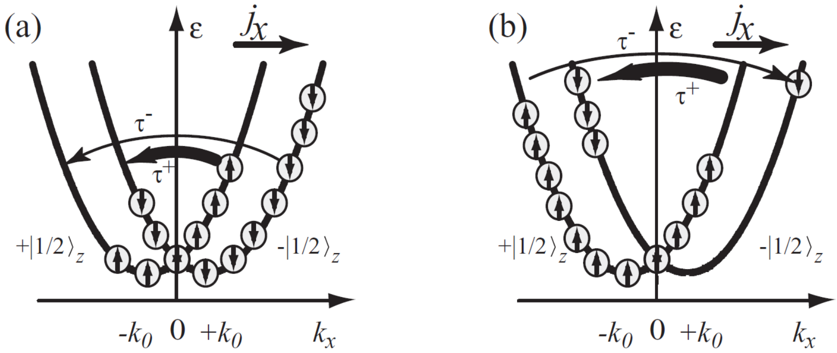

Figure 6.3: (a) Direct magnetoelectric effect; (b) inverse magnetoelectric effect (spin galvanic effect). Adopted from [40].

each of the subbands, no current flows. The current flow is caused by k-dependent spin-flip relaxation processes. Spins from the overpopulated subband are scattered along k_x to the less filled spin subband (see Fig. 6.3(b)). We only consider elastic processes here, but the same picture is also valid for inelastic relaxation processes. The spin flip scattering could be caused by a charged magnetic impurity that interacts with an electron via Coulomb interaction. The probability of that scattering is proportional to $1/(\Delta k_x)^2$, if we neglect screening, that is the spin-flip scattering rate depends on the values of the wavevectors of the initial and the final states. Four quantitatively different spin-flip scattering events exist. Two of them preserve the symmetric distribution of carriers in the subbands and, thus, do not yield a current. While the other two sketched in Fig. 6.3(b) by bent arrows, are inequivalent and generate an asymmetric carrier distribution around the subband minima in both subbands. This asymmetric population results in a current flow along the x-direction. Within this model of elastic scattering the current is not spin polarized since the same number of spin-up and spin-down electrons move in the same direction with the same velocity. For a Rashba material the spin galvanic effect also possible without spin-flip scattering because the spin polarization along the z-direction is provided by the spin imbalance, which is by itself asymmetric in each of the subbands.

6.3 The direct magnetoelectric (Edelstein) effect.

The direct magnetoelectric effect is just inverse to the spin galvanic one. The mechanism is shown in Fig. 6.3(a). At first, let the dispersion be spin-degenerated (no spin-orbit coupling). In equilibrium, the spin degenerated states are symmetrically occupied up to the Fermi energy. If an external electric field is applied, the charge carriers drift in the direction of the resulting force. The carriers are accelerated by the electric field and gain kinetic energy until they are scattered. A stationary state forms where the energy gain and the relaxation are balanced resulting in a nonsymmetric distribution of carriers in k-space yielding an electric current. As long as spin-up and spin-down states are degenerated in k-space the energy bands remain equally populated and a current is not accompanied by spin orientation. If the bands are split by spin-orbit coupling and have no fixed quantization axis, their nonsymmetric population (with respect to the band minimum) can result in the spin polarization, as for the case of Rashba material [41], see Fig. 6.4.

Or, if the spin-orbit split subbands have a fixed quantization axis, as for the case (110)-grown zinc-blende presented in Fig. 6.3(a), the applied electric current by itself is not enough for the polarization arising, because the spin-up and spin-down subbands are populated equally. Here the nonequal spin population of nonsymmetric in k-space subbands is again created

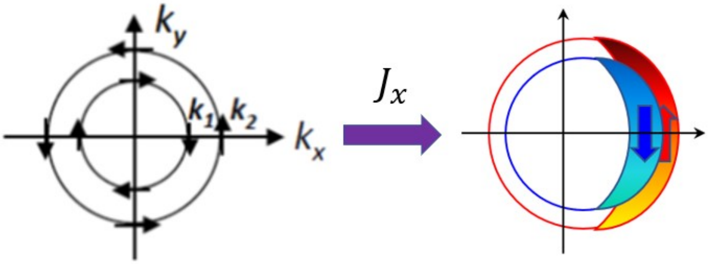

Figure 6.4: Direct magnetoelectric effect in 2D Rashba material. Under the applied electric current the Fermi surfaces are shifted in k-space. It results in the non-zero total spin $S_\pm$ carried by the conduction electrons in each of the subbands. The induced spins are opposite for the both Rashba bands. But due to the different k_F for the both subbands $|S_+| \neq |S_-|$ resulting in the nonzero net spin polarization $S = S_+ - S_-$.

by spin-flip scattering processes of different scattering rate, just as for the case of spin-galvanic effect.

6.4 Direct magnetoelectric effect in 3D topological insulators.

Topological insulators (TIs) form a new quantum phase of matter distinct from the classic dichotomy of metals and semiconductors. Whereas the bulk states form a bandgap, the surface states form a Dirac cone similar to graphene, see Fig. 6.5 and are topologically protected against disorder scattering. In marked contrast with the spin-degenerate bands of graphene, TI surface states are spin polarized. Examples of TI materials include $Bi_{1x}Sb_x$, Bi_2Se_3, Bi_2Te_3 and Sb_2Te_3. One of the most striking properties is spin-momentum locking; the spin of the TI Dirac surface state lies in-plane, and is locked at right

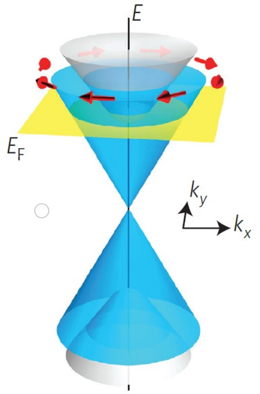

Figure 6.5: Dirac cone of the TI surface states (blue), with the spin at right angles to the momentum at each point. The bulk conduction and valence bands are shown in grey. Adopted from [42].

angles to the carrier momentum.

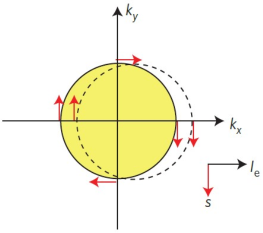

Figure 6.6: Top view of a Fermi-surface in the (k_x, k_y)-plane. An applied voltage produces a net momentum along k_x and spin-momentum locking gives rise to a net spin polarization oriented in-plane and at right angles to the current. Adopted from [42].

An unpolarized charge current should thus create a net spin polarization, the amplitude and orientation of which are controlled by the charge current. A top view of a cross-section of the surface-state bands taken above the Dirac point is approximately circular (with slight hexagonal warping), with the spin tangential at all points, as shown by the solid line in Fig. 6.6. A net momentum along the k_x direction (represented by a displacement of this circular cross-section along k_x, indicated by the dashed circle) produced by an electric field results in an electron current I_e along x. Owing to spin-momentum locking, this simultaneously induces a spin polarization oriented along $-y$. Thus, an unpolarized surface-state charge current creates a net spin polarization, with amplitude and orientation determined by the amplitude and direction of the charge current.

Quantitative result for the current-induced spin polarization can be obtained from the hamiltonian of the 3D TI surface states, which takes the form:

$$\hat{H} = v_F(\hat{z} \times \hat{\boldsymbol{\sigma}})\hat{\boldsymbol{p}}. \tag{6.23}$$

It can be shown that in the system described by hamiltonian (6.23) the electron spin polarization generated by the electric current is

$$\langle \boldsymbol{s} \rangle = -\frac{1}{2ev_F}[\boldsymbol{e}_z \times \boldsymbol{j}]. \tag{6.24}$$

The current-induced spin polarization has been directly measured as a voltage on a ferromagnetic metal tunnel barrier surface contact [42]. The magnetization of the contact determines the spin detection axis, and the voltage measured at this contact is proportional to the projection of the TI spin polarization onto this axis. An unpolarized bias current is applied between two non-magnetic contacts, see Fig. 6.7. When the charge current is orthogonal to the magnetization of the ferromagnetic detector contact, the TI spin is parallel (or antiparallel) to the magnetization and a spin-related signal is

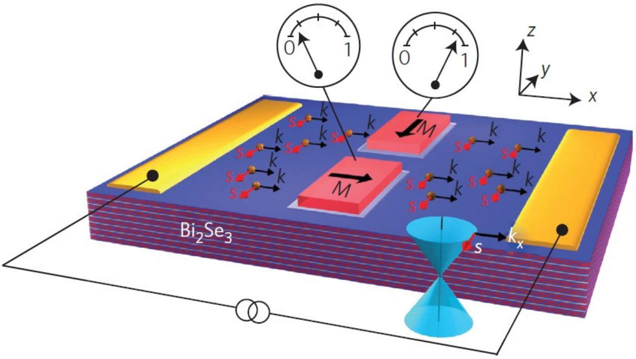

Figure 6.7: Sketch of the transport experiment. The voltage measured at the ferromagnetic detector is proportional to the projection of the current-induced TI spin polarization onto the contact magnetization. Adopted from [42].

detected at the ferromagnetic contact proportional to the magnitude of the charge current. When the direction of the charge current is reversed, the measured voltage changes sign. When the contact magnetization is rotated in-plane 90° so that the charge current is parallel to the magnetization, no spin voltage is detected, because the TI spin polarization is now orthogonal to the contact magnetization.

Chapter 7

Spin relaxation

When an electron is introduced in a solid, interaction with the environment can affect its spin orientation. The environment may give rise to an effective magnetic field which interacts with the spin and causes it to alter its state, thereby changing the orientation. The effective magnetic field can arise from a multitude of sources, e.g., the spins of other electrons and holes in the solid, nuclear spins, phonons that give rise to a time varying magnetic field in some circumstances, and, the most important, spin-orbit interactions in the solid that act like an effective magnetic field. Below we consider different mechanisms of the spin relaxation.

7.1 Elliott-Yafet mechanism.

The Schrodinger equation governing an electron motion in a crystal is

$$\left[-\frac{\hbar^2\nabla^2}{2m}+V_L(\boldsymbol{r})+H_{so}\right]\hat{\Psi}=E\hat{\Psi}, \tag{7.1}$$

where $V_L(\boldsymbol{r})$ is the periodic lattice potential. The solution of the unperturbed hamiltonian in the absence of the spin-orbit coupling $\hat{\Psi}_0(\boldsymbol{r})$ is given by the Bloch theorem $\hat{\Psi}_0(\boldsymbol{r}) = e^{i\boldsymbol{kr}}u_{\boldsymbol{k}}(\boldsymbol{r})$. The spin-orbit interaction mixes up the up-spin and down-spin Bloch functions so that

$$\hat{\Psi}_{k\uparrow} = e^{i\boldsymbol{kr}}\left\{a_{\boldsymbol{k}}\begin{pmatrix}1\\0\end{pmatrix} + b_{\boldsymbol{k}}\begin{pmatrix}0\\1\end{pmatrix}\right\} \tag{7.2}$$

$$\hat{\Psi}_{k\downarrow} = e^{i\boldsymbol{kr}}\left\{a^*_{-\boldsymbol{k}}\begin{pmatrix}0\\1\end{pmatrix} + b^*_{-\boldsymbol{k}}\begin{pmatrix}1\\0\end{pmatrix}\right\}. \tag{7.3}$$

According to the perturbation theory $|b| \approx \lambda_{so}/\Delta E$, where ΔE is the energy distance between the band state in question and the state (of the same momentum) in the nearest band, and λ_{so} is the amplitude of the matrix element of H_{so} between the two states.

The spin state of a nearly up-spin electron at a wavevector state k and that of a nearly down-spin electron at a different wavevector state k' are not strictly orthogonal, since they are not strictly anti-parallel (see Fig. 7.1). Thus, any collision with a non-magnetic scatterer that changes the wavevector of an electron from an initial state k to a state k' can also couple the nearly down-spin state at k to the nearly up-spin state at k'. This coupling can flip an electrons spin from nearly up to nearly down.

The spin relaxation time can be estimated as

$$\frac{1}{\tau_s} \sim \left|\langle\hat{\Psi}_{\boldsymbol{k}\uparrow}|V_i|\hat{\Psi}_{\boldsymbol{k}'\downarrow}\rangle\right|^2 \sim |b|^2\left|\langle\hat{\Psi}_{\boldsymbol{k}\uparrow}|V_i|\hat{\Psi}_{\boldsymbol{k}'\uparrow}\rangle\right|^2 \sim |b|^2\frac{1}{\tau}, \tag{7.4}$$

where V_i is the impurity potential and τ is the momentum relaxation time. Note that this kind of spin relaxation is always accompanied by some degree of momentum relaxation since the wavevector must change in order to change the spin. Therefore, the Elliot-Yafet spin relaxation is *caused by the momentum relaxation.*

The Elliott-Yafet mechanism is often the primary spin relaxation mechanism in ordinary metals and low mobility materials, such as organics, where momentum relaxing scattering

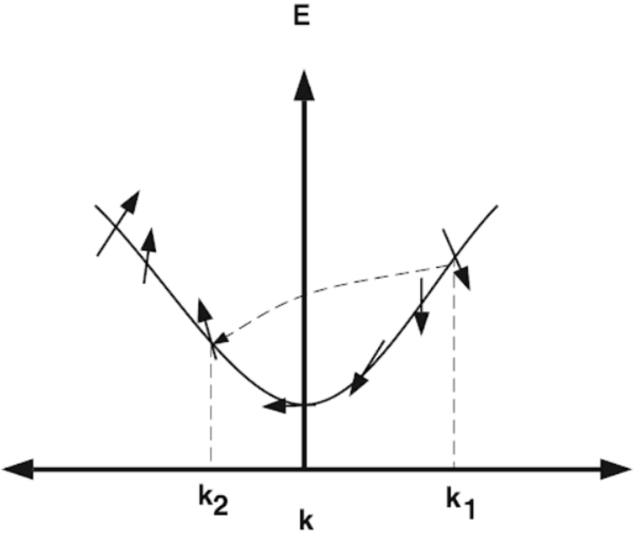

Figure 7.1: Energy dispersion relation showing the spin polarizations at different wavevector states. Each wavevector state has two possible mutually anti-parallel spin polarizations, one of which is shown by the arrowheads. A momentum changing collision event, which changes the wavevector state from k_1 to k_2, also changes the spin orientation since the eigenspin polarizations at k_1 and k_2 are generally not parallel. Adopted from [15].

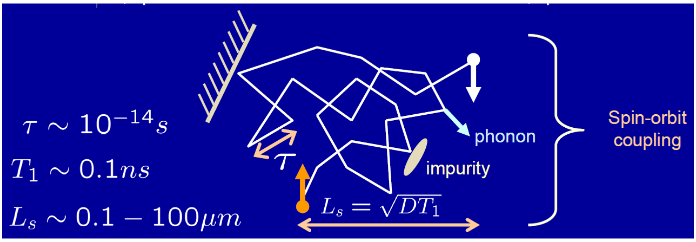

Figure 7.2: Elliot-Yafet mechanism of spin relaxation. Adopted from the presentation by Y. Fabian.

events are frequent. In high mobility semiconductors, the primary spin relaxation mechanism is usually the Dyakonov-Perel mechanism, which we discuss next.

7.2 Dyakonov-Perel mechanism.

It is an efficient mechanism of spin relaxation due to spin-orbit coupling in systems lacking inversion symmetry. The spin-orbit interaction lifts the degeneracy between the spin-up and spin-down states of the same wave-vector, giving rise to the effective magnetic field, which depends on the electron momentum. The effective magnetic field causes an electrons spin to undergo Larmor precession. The precession axis is collinear with the magnetic field and the precession frequency is $\Omega(\boldsymbol{p}) = g\mu_B B(\boldsymbol{p})/\hbar$. Now consider an ensemble of electrons drifting and diffusing in a solid. If $\boldsymbol{p}$ is distributed randomly because of scattering, then different electrons would have precessed by different angles after a certain time. Thus, if all electrons are injected with the same spin polarization, their spin polarizations gradually go out of phase with each other. After a sufficiently long time, the magnitude of the ensemble averaged spin will decay to zero. This is the basis of Dyakonov Perel (D-P) spin relaxation.

In the regime of $\Omega < 1/\tau$ the process can be considered as a spin precession about a fluctuating magnetic field. The electron spin rotates about the intrinsic field at an angle $\delta\phi \approx \Omega\tau$ before experiencing another field and starting to rotate with a different speed and in a different direction. As a result, the spin phase follows a random walk: after time t, which amounts to t/τ steps of the random walk, the phase progresses by $\phi(t) = \delta\phi\sqrt{t/\tau}$. By the order of magnitude τ_s is the time at which $\phi(t) = 1$, what gives us $1/\tau_s = \Omega^2\tau$.

The D-P spin relaxation is an ensemble phenomenon that can only be understood in a many particle picture. A single electron can not experience D-P relaxation. Its spin will coherently precess about the effective magnetic field caused by spin-orbit interaction, even when that field is changing randomly in time and space because of velocity randomizing collisions. However, in an ensemble of many electrons, different electrons are precessing about different magnetic fields simultaneously. Since all these precessions are not synchronous (the scattering histories of the different electrons are independent), the precessions go out of phase with each other. Hence the ensemble average spin decays in time and space.

7.3 Bir-Aronov-Pikus mechanism.

The Bir-Aronov-Pikus mechanism is a source of spin relaxation of electrons in semiconductors where there is a significant concentration of both electrons and holes. In that case, an electron will usually be in close proximity to a hole, so that their wavefunctions will overlap, which will cause an exchange interaction between them.

The exchange interaction between electrons and holes is governed by the Hamiltonian

$$H = A\boldsymbol{S} \cdot \boldsymbol{J}\delta(\boldsymbol{r}), \tag{7.5}$$

where A is proportional to the exchange integral between the conduction and valence states, $\boldsymbol{J}$ is the angular momentum operator for holes, $\boldsymbol{S}$ is the electron-spin operator, and $\boldsymbol{r}$ is the relative position of electrons and holes. A general trend is that the Bir-Aronov-Pikus dominates in heavily doped samples at small temperatures.

One can learn more about the considered spin relaxation mechanisms and to find a good list of the corresponding original papers in review [18].

7.4 Hyperfine interactions with nuclear spins

The hyperfine interaction, which is the magnetic interaction between the magnetic moments of electrons and nuclei, provides an important mechanism for single-spin decoherence of localized electrons, such as those confined in quantum dots or bound on donors. This interaction is too weak to cause effective spin relaxation of free electrons in metals or in bulk semiconductors.

In a solid, the nuclear spins generate a magnetic field which interacts with the electron spins via hyperfine contact interaction and can cause spin relaxation. The Hamiltonian describing this interaction is given by

$$H_{nuclear} = \boldsymbol{S} \sum_i A_i \boldsymbol{I}_i, \tag{7.6}$$

where $\boldsymbol{I}_i$ is the spin of the i-th nucleus, A is a constant and A_i is the corresponding coupling coefficient. The quantity A_i is given by $A_i = A|\psi_i(\boldsymbol{r}_i)|^2$, where $\psi(\boldsymbol{r}_i)$ is the electron envelope wavefunction at the nuclear site $\boldsymbol{r}_i$.

The spin flip rates have been calculated in different types of quantum dots at various temperatures. These rates are very small, typically less than $10^5 s^{-1}$ in GaAs quantum dots under reasonable conditions. Experimentally the spin relaxation times of the order of $50 \mu s$ up to several ms and even up to $1s$ were reported [15].

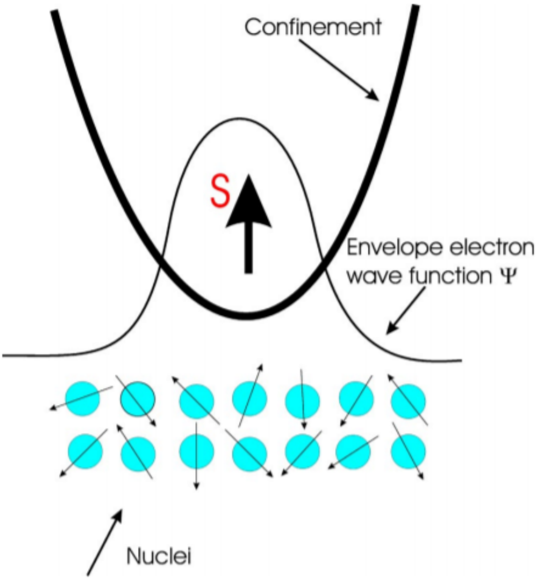

Figure 7.3: The sketch of the system consisting of a single spin in a quantum dot interacting with nuclear spins. Adopted from [43].

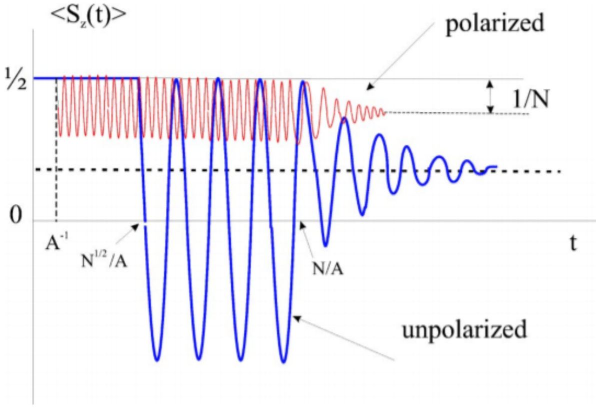

Figure 7.4: Dependence of $\langle S_z \rangle$ on time. Adopted from [43].

Chapter 8

Spin caloritronics.

It is well known that except for the electric field and the concentration gradient, which are combined into the gradient of the electrochemical potential, there exists another driving force for the charge current, which is the temperature difference ΔT between the two electrodes. The temperature difference is the source of thermoelectric effects including Seebeck effect and Pertier effect. The temperature difference naturally produces a flow of heat Q, or thermal conduction. Thus, ΔT produces both electrical and thermal currents. Similarly, $\Delta\mu$ produces thermal current as well as an electrical current. These effects are simply expressed in the coupled equation:

$$\begin{pmatrix} \boldsymbol{j}_c \\ \boldsymbol{j}_q \end{pmatrix} = \begin{pmatrix} L_{11} & L_{12} \\ L_{21} & L_{22} \end{pmatrix} \begin{pmatrix} \boldsymbol{\nabla}\mu \\ -\boldsymbol{\nabla}T/T \end{pmatrix}. \tag{8.1}$$

When two different metals with different chemical potentials come in contact, electrons transfer from one metal to the other so as to make the chemical potential equal, and consequently an equilibrium state is realized. In magnetic metals, up and down-spin states are in contact with each other, and therefore the up-spin chemical potential $\mu_\uparrow$ equals the down-spin chemical potential $\mu_\downarrow$. The state with nonzero spin imbalance $\mu_s = \mu_\uparrow - \mu_\downarrow \neq 0$ survives, however, when the nonequilibrium state is stabilized, such as by the spin injection or spin Hall current driven by an external current, as explained in the previous section. As we have already known $\boldsymbol{\nabla}\mu_s$ is a driving force of the spin current. Now we have three driving forces (surely they are not real forces) $\boldsymbol{\nabla}\mu$, $\boldsymbol{\nabla}m_s$ and $\boldsymbol{\nabla}T$, that produce charge current $\boldsymbol{j}_c$, spin current $\boldsymbol{j}_s$, and thermal current $\boldsymbol{j}_Q$. These three quantities are related to each other and give the following generalized relationship

$$\begin{pmatrix} \boldsymbol{j}_c \\ \boldsymbol{j}_s \\ \boldsymbol{j}_q \end{pmatrix} = \begin{pmatrix} L_{11} & L_{12} & L_{13} \\ L_{21} & L_{22} & L_{23} \\ L_{31} & L_{32} & L_{33} \end{pmatrix} \begin{pmatrix} \boldsymbol{\nabla}\mu \\ \boldsymbol{\nabla}\mu_s/2 \\ -\boldsymbol{\nabla}T/T \end{pmatrix}. \qquad (8.2)$$

The equation above shows that the spin and heat current couple with each other. This is the basic idea behind spin caloritronics. Below, we derive the corresponding coefficients L_{ij} in the framework of two-spin current model of ferromagnetic metals. As it follows from Eqs. (2.5) and (2.10), $L_{11} = L_{22} = \sigma$, $L_{12} = L_{21} = \sigma P_\sigma$. The equality $L_{ij} = L_{ji}$ is valid for all the coefficients L_{ij} and is known as as Onsagers reciprocity relationship.

Now our goal is to derive the other coefficients, which describe thermoelectric effects. The change in heat δQ is related to a change in the internal energy and particle number as $\delta Q = TdS = dE - \mu dn$. Then $\boldsymbol{j}_q = \boldsymbol{j}_E - \mu\boldsymbol{j}$, where $\boldsymbol{j}_E$ is the energy current and $\boldsymbol{j}$ is the particle current. The currents for each of the spin subbands can be expressed via the sum of separate electron contributions:

$$\boldsymbol{j}_{E,\sigma} = \int \boldsymbol{v}_\sigma \varepsilon_\sigma(\boldsymbol{k}) f_\sigma(\boldsymbol{k}) \frac{d^3k}{(2\pi)^3}, \tag{8.3}$$

$$\boldsymbol{j}_\sigma = \int \boldsymbol{v}_\sigma f_\sigma(\boldsymbol{k}) \frac{d^3k}{(2\pi)^3}, \tag{8.4}$$

$$\boldsymbol{j}_{q,\sigma} = \int \boldsymbol{v}_\sigma (\varepsilon_\sigma(\boldsymbol{k}) - \mu_\sigma) f_\sigma(\boldsymbol{k}) \frac{d^3k}{(2\pi)^3}. \tag{8.5}$$

$$\tag{8.6}$$

The distribution function f can be found from the Boltzman equation, which takes the form

$$\Big(\frac{\partial}{\partial t} + \boldsymbol{v}\boldsymbol{\nabla}_{\boldsymbol{r}} + \frac{e\boldsymbol{E}}{\hbar}\boldsymbol{\nabla}_{\boldsymbol{k}}\Big) f(\boldsymbol{r}, \boldsymbol{k}, t) = -\frac{f - f_0}{\tau}. \tag{8.7}$$

Taking into account that $\boldsymbol{\nabla}_{\boldsymbol{r}} f = (\partial f/\partial T)\boldsymbol{\nabla}_{\boldsymbol{r}} T = -(\varepsilon - \mu)/T(\partial f/\partial\varepsilon)\nabla_{\boldsymbol{r}} T$, to the linear order with respect to driving forces we obtain

$$f(\boldsymbol{k}) \approx f_0(\boldsymbol{k}) - \frac{e}{\hbar}\tau \boldsymbol{E}\boldsymbol{\nabla}_{\boldsymbol{k}} f_0(\boldsymbol{k}) + \tau\boldsymbol{v}\frac{\varepsilon - \mu}{T}\frac{\partial f_0}{\partial\varepsilon}\nabla_{\boldsymbol{r}} T. \tag{8.8}$$

Substituting Eq. (8.8) (taken for each of the subbands separately) into Eqs. (8.6), we obtain:

$$\boldsymbol{j}_\sigma = e\int \boldsymbol{v}_\sigma\Big[-e\tau_\sigma\frac{\partial f_0}{\partial\varepsilon}(\boldsymbol{v}_\sigma\boldsymbol{E}) + \tau_\sigma\frac{\varepsilon - \mu_\sigma}{T}\frac{\partial f_0}{\partial\varepsilon}(\boldsymbol{v}_\sigma\boldsymbol{\nabla}T)\Big]\frac{d^3k}{(2\pi)^3} = e^2 M_0 \boldsymbol{E} - eM_1\frac{\nabla T}{T}, \tag{8.9}$$

where

$$M_n = \int \frac{d^3k}{(2\pi)^3} v_{\sigma,x}^2 \tau_\sigma (\varepsilon - \mu_\sigma)^n \Big(-\frac{\partial f_0}{\partial\varepsilon}\Big) = \frac{1}{3}\int_{-\infty}^{\infty} N_\sigma(\varepsilon) v_\sigma^2 \tau_\sigma (\varepsilon - \mu_\sigma)^n \Big(-\frac{\partial f_0}{\partial\varepsilon}\Big) d\varepsilon. \tag{8.10}$$

The above integrals are examples of the so-called Sommerfeld integrals

$$\int\limits_{-\infty}^{\infty} K(\varepsilon)(-\frac{\partial f_0}{\partial \varepsilon})d\varepsilon = K(\mu) + \sum_{n=1}^{\infty} a_n (kT)^{2n} K^{(2n)}(\varepsilon)\big|_{\varepsilon=\mu},$$

$$a_n = (2 - \frac{1}{2^{2(n-1)}})\zeta(2n). \qquad (8.11)$$

The derivation of the above result can be found in [44]. In our case

$$K_0 = \frac{1}{3}N_\sigma(\varepsilon)v_\sigma^2\tau_\sigma \quad \Rightarrow$$

$$M_0 = \frac{1}{3}N_\sigma(\varepsilon)v_\sigma^2\tau_\sigma\big|_{\varepsilon=\mu} = \frac{\sigma_\sigma(\mu_\sigma)}{e^2}, \qquad (8.12)$$

$$K_1 = \frac{1}{3}N_\sigma(\varepsilon)v_\sigma^2\tau_\sigma(\varepsilon-\mu_\sigma) \quad \Rightarrow$$

$$M_1 = \frac{\pi^2}{3}(kT)^2\frac{\sigma'_\sigma(\mu_\sigma)}{e^2}. \qquad (8.13)$$

The electric current (2.5) can be rewritten as follows

$$\boldsymbol{j}_\sigma = \sigma_\sigma \boldsymbol{E} - \sigma_\sigma S_\sigma \boldsymbol{\nabla} T, \qquad (8.14)$$

where $S_\sigma = eM_1/(T\sigma_\sigma) = -L_0|e|T\sigma'_\sigma/\sigma_\sigma$ is the Seebeck coefficient for a given spin subband and $L_0 = \pi^2k^2/3e^2$ is the Lorentz number. Introducing the spin-independent Seebeck coefficient $S = (S_\uparrow\sigma_\uparrow + S_\downarrow\sigma_\downarrow)/\sigma$, the kinetic coefficients L_{ij} can be written as

$$L_{13} = L_{31} = \sigma S T, \qquad (8.15)$$

$$L_{23} = L_{32} = P' S T, \qquad (8.16)$$

where $P' = \partial(P_\sigma\sigma)/\partial\varepsilon|_{\varepsilon=\mu}$.

According to Eqs. (8.2) and (8.16), not only an applied voltage but also a temperature gradient drives a spin current in a conducting ferromagnet. Conservation of charge and spin currents at a contact between the ferromagnet and a normal metal then implies spin current injection into the normal metal under a temperature bias.

8.1 The spin-dependent Seebeck effect.

The generation of an electrical voltage by placing a conductor in a thermal gradient is the well-known Seebeck effect. In the framework of the linear response theory the induced voltage is proportional to the temperature gradient as $\Delta V = S\Delta T$, where the Seebeck coefficient S depends on the particular material parameters. From Eq. (8.15) it is seen that the Seebeck coefficient is determined by the derivative of the conductivity with respect to energy, therefore it is typically small in metals. But it can considerably larger in semiconductors.

The generation of a spin imbalance by placing a sample in a thermal gradient is the spin-dependent Seebeck effect. A spin-dependent Seebeck effect has been demonstrated in lateral spin-valve structures [45]. Here a temperature gradient is generated over an interface by resistive heating of a ferromagnet (FM1 in Fig. 8.1(a)). In the absence of the charge injection to the normal metal the spin imbalance is generated. Fig. 8.1(b) shows the spin-dependent electrochemical potentials. The induced spin imbalance is detected by means of the voltage difference V with respect to an analysing ferromagnetic contact FM2.

The spin-dependent Seebeck effect has also been measured in metallic ferromagnets [47]. The effect is illustrated in Fig. 8.2.

The thermally induced spin current can be also carried by magnons, not conduction electrons. In this case it is not

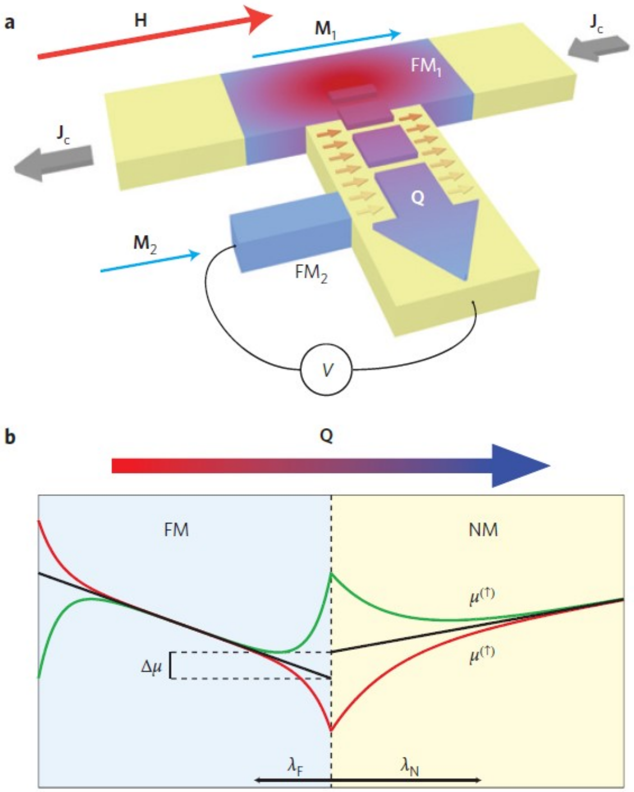

Figure 8.1: (a) Sketch of the measuring device. (b) Schematics of thermal spin injection by the spin-dependent Seebeck effect across an FM—NM interface. Adopted from [46].

accompanied by electric current and can be observed at interfaces with ferromagnetic insulators as well. It is often called "spin Seebeck effect".

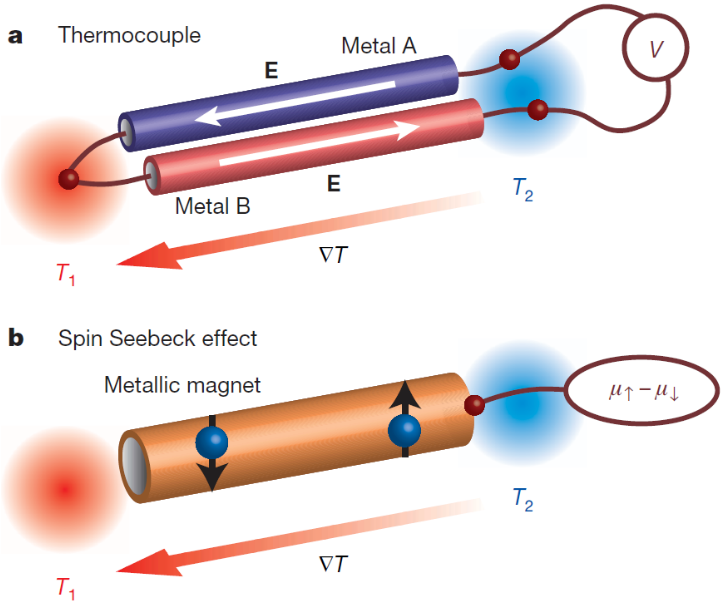

Figure 8.2: (a) A thermocouple consists of two conductors (metals A and B) connected to each other. They have different Seebeck coefficients and, thus, the voltage V between the output terminals is proportional to the temperature difference $T_1 - T_2$ between the ends of the couple. (b) Illustration of the spin Seebeck effect. In a metallic magnet, spin-up and spin-down conduction electrons have different Seebeck coefficients. When a temperature gradient is applied, a spin voltage $\mu_\uparrow - \mu_\downarrow$ proportional to the temperature difference appears; a magnet functions just like a thermocouple, but in the spin sector. Adopted from [47].

8.2 The Spin Peltier effect.

The Spin Peltier effect is the Onsager reciprocal of the Spin Seebeck effect. It is the generation of a magnon heat current in a magnetic insulator by the flow of a spin current through the

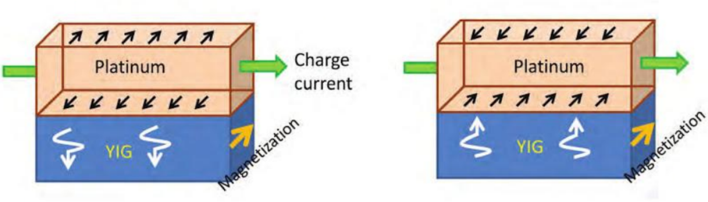

Figure 8.3: The spin Peltier effect. Adopted from [15].

interface with the metallic contact. This phenomenon has been demonstrated experimentally in a Pt-YIG (platinum yttrium-iron-garnet) heterostructure [48]. Consider Fig. 8.3. A charge current through the platinum induces a transverse spin current through a magnetized YIG layer due to the Spin Hall effect. When the spin magnetic moments of electrons at the interface between Pt and YIG are anti-parallel to the magnetization of the YIG, the spin torque transfers energy and momentum from the electrons in the Pt to the magnons in the YIG, thereby cooling the electrons and heating the magnons. This raises the magnon temperature over the electron temperature. When the spin magnetic moments of electrons are parallel to the magnetization (right panel), the spin torque transfers energy and momentum from the magnons in the YIG to the electrons in the Pt, thereby cooling the magnons and heating the electrons.

8.3 Giant spin-dependent Seebeck effect in superconducting heterostructures.

8.3.1 Giant spin-dependent Seebeck effect.

As it was already mentioned, from Eq. (8.15) it is seen that the Seebeck coefficient is determined by the derivative of the conductivity with respect to energy, therefore it is typically small in metals because $\sigma'/\sigma \propto 1/\varepsilon_F$ and the resulting Seebeck coefficient $\sim T/\varepsilon_F$, what does not exceed $\sim 10^{-2}$ even at room temperatures. The physical reason of this small factor is the weakness of the electron-hole asymmetry at the Fermi level in metals, see Figs. 8.4(a)-(b). If the conductivity would be fully particle-hole symmetric with respect to the Fermi surface, as in Fig. 8.4(a), thermally excited quasiparticles would consist of equal number of electrons and holes and, therefore, the resulting thermally-generated electric current is zero. The non-zero electric current is only due to small electron-hole asymmetry resulting in non-zero difference between the electron and hole currents, see Fig. 8.4(b).

Now let us consider a superconductor. It has a gap in the density of states (DOS) at the Fermi level, see Fig. 8.4(d), resulting in the strong dependence of the DOS on the quasiparticle energy in the vicinity of the Fermi level. The DOS is still symmetric with respect to the Fermi energy, therefore there are no any gain in the Seebeck coefficient with respect to the normal metal. For simplicity we neglect the weak electron-hole asymmetry of the normal metal in Fig. 8.4(b). However, if we somehow shift the middle of the gap with respect to the Fermi level, we will have the giant electron-hole asymmetry in vicinity of the Fermi level due to the strong energy dependence of the superconducting DOS.

The plan can be realized by applying a Zeeman field to the superconductor (via external parallel magnetic field or as an internal effect in a hybrid S/F structure.) Then the DOS becomes spin-split and the middle of the gaps are shifted in opposite directions with respect to the Fermi level, see Fig. 8.4(e). Then in each of the spin subbands the thermally-induced electric current is created. One of them is carried by electrons and the other one by holes, therefore they exactly compensate each other. However, the both quasiparticle flows carry the same spin current (the spin of the hole quasiparticle in the spin-down subband is up and vice versa). Therefore, the spin-split supercondutor in the presence of thermal gradient sustains pure quasiparticle spin current. The value of this spin current is giant as compared to nonsuperconducting ferromagnetic metals because due to the presence of the spin-split gap practically all possible quasiparticles carry spin in the same direction and the reducing factor T/ε_F is absent. This effect is called giant thermospin effect.

It allows for injection of a thermally-induced spin current via a superconductor/normal metal interface. Moreover, if the interface barrier is spin-filtering, that is the spin-up and spin-down conductances of the barrier are different, the spin current is accompanied by the thermally-induced electric current. This is because the thermally excited quasiparticles from the spin-up subband (electrons) and from the spin-down subband (holes) have different tunnel probablities and, therefore, the electron and hole currents are not exactly compensated. It is called giant thermoelectric effect. This effect has been predicted theoretically [49, 50] and observed experimentally [51, 52].

Fig. 8.5 demonstrates the sketch of the measurement configuration. The spin-split DOS was created in the superconducting Al by applying the external parallel magnetic field. The spin-filtering barrier is made of Fe. It is heated by applying the current I_{heat}. The Seebeck voltage is measured between the superconducting Al and normal Cu electrodes. Seebeck coefficients of the order of 0.3mV/K were measured, which is comparable to the thermopower measured in magnetic semiconductors at much higher temperatures and is much larger than the thermoelectric effects in metals, where the Seebeck coefficient is typically of the order of a few $\mu V/K$ at room temperature and vanishing at low temperature.

8.3.2 Thermally-induced DW motion in S/F bilayers.

The giant thermospin effect can cause highly efficient DW motion in thin film S/F bilayers. Thermally induced quasiparticles both electron- and hole-like move from the hot to the cold end. In the bulk of both domains the magnetic moments of the quasiparticles are polarized along the corresponding magnetization. Therefore, the spin current (opposite to the magnetization current) in the bulk of both domains is directed away from the DW. In the left (hotter) domain the direction of the majority spin flow is opposite to the spin current direction, while in the right (colder) domain they coincide. Therefore, the spin current flowing in both domains, pumps majority spins of the hotter domain into the DW region. This leads to the expansion of the hotter domain and, consequently, the DW moves from the hot to the cold end. The estimated ratios of the DW velocities to the tapplied emperature gradients $v_{DW}/\nabla T \gtrsim 10 - 10^2$ mm^2/Ks for the S/F system, which is about three order of magnitude larger than the values $\sim 10^{-2} - 10^{-1}$ mm^2/Ks reported for thermally induced domain wall motion in ferromagnetic materials.

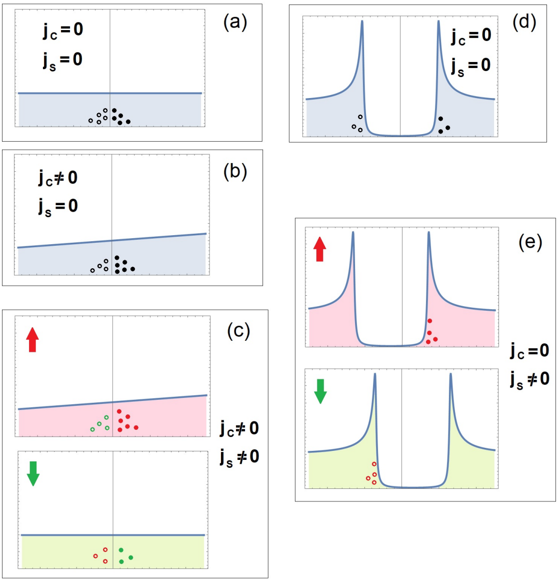

Figure 8.4: Each of the panels represent the DOS as a function of energy measured from the chemical potential, filled by electron-like quasiparticles (filled circles) and hole-like quasiparticles (open circles) at the hot end of the sample. (a) Fully electron-hole symmetric normal state DOS; (b) Asymmetric normal state DOS. Due to the asymmetry of the DOS the number of electron-like quasiparticles exceeds the number of hole-like quasiparticles and, therefore, the total electric current is non-zero; (c) Two different spin subbands in metal ferromagnet. Spin-up quasiparticles are colored in red and spin-down quasiparticles are colored in green. Here the total numbers of spin-up and spin-down quasiparticles are different and, therefore, the electric current is accompanied by the spin current. (d) Superconducting DOS in the absence of spin splitting. The gap is opened at the Fermi surface. (e) Spin-split superconducting DOS. It is seen that because of the gap there are hole-like quasiparticles in the spin-up subband and there are no electron-like quasiparticles in the spin-down subband. All the quasiparticles carry the same spin.

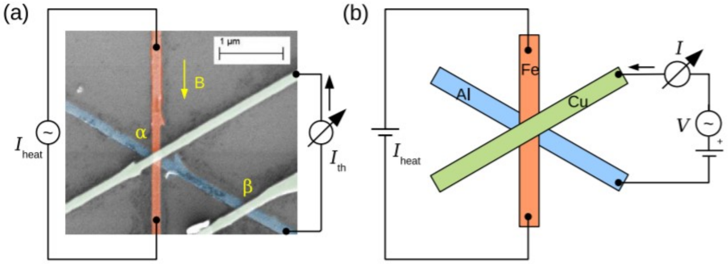

Figure 8.5: Measurement scheme of the giant thermoelectric effect. (a) False-color scanning electron microscopy image of the sample with the measurement configuration for the thermoelectric measurements. (b) Sketch of the measurement configuration. Adopted from [51].

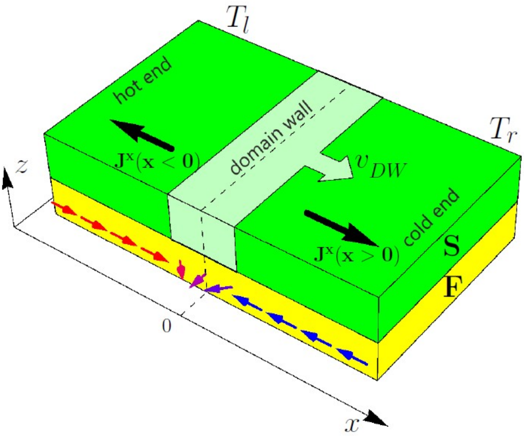

Figure 8.6: Sketch of the bilayer S/F system. The magnetization of the ferromagnet F has a form of a head-to-head domain wall (DW) and is indicated by arrows. The picture on the top surface illustrates the process of thermally induced spin pumping into the DW region.

Chapter 9

Magnonics.

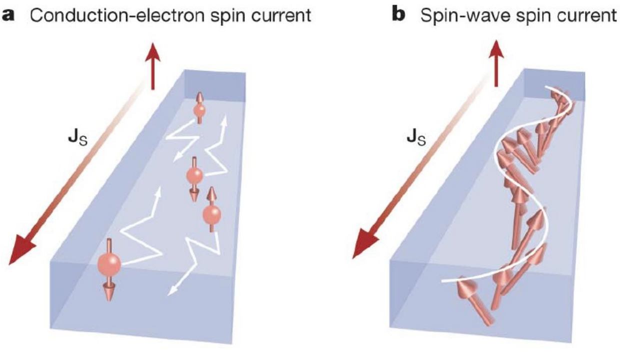

Figure 9.1: (a) A schematic illustration of a conduction-electron spin current: spin angular momentum $\boldsymbol{J}_s$ carried by electron diffusion. (b) A schematic illustration of a spin-wave spin current: spin angular momentum carried by collective magnetic-moment precession. Adopted from [53].

As we have already know, a flow of spin angular momentum is called a spin current. In solids, there are two types of carriers for non-equilibrium spin currents. One is a conduction electron. The other is collective motion of magnetic moments

- spin waves, see Fig. 9.1. Here we call a spin current carried by spin waves a "spin-wave spin current". Extensive studies of conduction-electron spin currents in metals and semiconductors have clarified that the currents have a critical problem; they disappear within a very short distance, typically hundreds of nanometres. In contrast, it has been shown that a spin wave spin current may persist for much greater distances because it is carried by the collective motion of spins coupled by exchange interaction. Significantly, a spin-wave spin current exists even in magnetic insulators, in which its decay is typically suppressed. This is because the decay is caused mainly by conduction electrons, which are absent in insulators. For instance, in the magnetic insulator $Y_3Fe_5O_{12}$, the spin-wave decay length can be several centimetres and thus the waves are propagated over a relatively long distance; $Y_3Fe_5O_{12}$ is an ideal conductor for spin-wave spin currents even though it is an insulator for electric currents.

9.1 Magnonic spectrum and magnonic spin current.

In a ferromagnetic metal (F), both charge and spin currents flow by application of bias voltage, since the spins of conduction electrons are spontaneously polarized. In a nonmagnetic metal (N), spin current is created by spin injection from a ferromagnet attached to N or by the spin Hall effect in N, in which up-spin and down-spin electrons flow in the opposite directions without charge current, resulting in the so-called pure spin current. In this way, the spin current is able to flow in metallic conductors. Ferromagnetic insulators, on the other hand, have different properties that they are electrically inactive with frozen charge degrees of freedom, but magnetically active due to the spins of localized electrons. The low-lying magnetic excitations are spin waves whose propagation carries spin angular momentum. The low-lying magnetic excitation of spin waves is described by the Landau-Lifshitz- Gilbert equation

$$\frac{\partial \boldsymbol{M}(\boldsymbol{r},t)}{\partial t} = \gamma \boldsymbol{H}_i \times \boldsymbol{M} - \frac{D}{\hbar M_s}\boldsymbol{M} \times \nabla^2 \boldsymbol{M} + \frac{\alpha}{M_s}\boldsymbol{M} \times \frac{\partial \boldsymbol{M}(\boldsymbol{r},t)}{\partial t} \quad (9.1)$$

where $\boldsymbol{H}_i = (0, 0, H_i)$ is an internal anisotropy field along the z direction, $D = \gamma A$ is the exchange stiffness, α is the Gilbert damping constant. Let us find solution of Eq. (9.1) as $\boldsymbol{M} = M_s \boldsymbol{e}_z + \delta \boldsymbol{M}$. Then from $\boldsymbol{M}^2 = M_s^2$ it follows that to the first order $\delta \boldsymbol{M} = (\delta M_x, \delta M_y, 0)$. The solution of Eq. (9.1) takes the form

$$\delta \boldsymbol{M}_+(\boldsymbol{r},t) = \delta \boldsymbol{M}_0 e^{i\boldsymbol{q}\boldsymbol{r}+i\omega_q t} e^{-\alpha\omega_q t}, \quad (9.2)$$

where $\hbar\omega_q = \hbar\gamma H_i + Dq^2$ is the magnon dispersion. In the following, the Gilbert damping term is disregarded for simplicity. Then, Eq. (9.1) can be rewritten as

$$\frac{\partial \boldsymbol{M}(\boldsymbol{r},t)}{\partial t} = \gamma \boldsymbol{H}_i \times \boldsymbol{M} - \boldsymbol{\nabla} \boldsymbol{J}^M(\boldsymbol{r},t), \quad (9.3)$$

where $\boldsymbol{J}^M(\boldsymbol{r},t)$ is the magnetization current, which we call the spin-wave spin current, whose components are

$$J_j^{M_\alpha} = \frac{D}{\hbar M_s}[\boldsymbol{M} \times \nabla_j \boldsymbol{M}]_\alpha. \quad (9.4)$$

Note that the z-component of equation Eq. (9.3) gives the conservation $\partial_t M_z + \boldsymbol{\nabla} \boldsymbol{J}^{M_z} = 0$ in case of $\alpha = 0$. By introducing $\psi(\boldsymbol{r},t) = M_x + iM_y$ and its conjugate complex $\psi^*(\boldsymbol{r},t)$, the z-component of the spin-wave spin current is written as

$$\boldsymbol{J}_j^{M_z} = \frac{1}{2i}\frac{D}{\hbar M_s}[\psi^*(\boldsymbol{r},t)\boldsymbol{\nabla}\psi(\boldsymbol{r},t) - \psi(\boldsymbol{r},t)\boldsymbol{\nabla}\psi^*(\boldsymbol{r},t)]. \quad (9.5)$$

Using the creation and annihilation operators $(b_q, b_q^\dagger)$ of spin-wave excitations with energy ω_q and momentum q by the transformations $\psi = \sqrt{2\hbar\gamma M_s}\sum_q b_q e^{i\boldsymbol{qr}}$ and $\psi^* = \sqrt{2\hbar\gamma M_s}\sum_q b_q^\dagger e^{-i\boldsymbol{qr}}$, the spin-wave spin current is expressed in the second-quantized form, whose expectation value is

$$\boldsymbol{J}_j^{M_z} = \hbar\gamma \sum_q \boldsymbol{v}_q n_q, \tag{9.6}$$

where $\boldsymbol{v}_q = \partial\omega_q/\partial_{\boldsymbol{q}} = 2(D/\hbar)\boldsymbol{q}$ the spin-wave velocity and $n_q = \langle b_q^\dagger b_q \rangle$ is the distribution function of spin-waves. Eq. (9.6) indicates that, when the population of spin waves is different between $\boldsymbol{q}$ and $-\boldsymbol{q}$ in the wave-vector space, the spin waves carry the spin-wave spin current.

9.2 Electron spin current - magnon spin current interconversion

To make use of the spin-wave spin currents in insulators, it is necessary to find methods for getting a d.c. spin current into and out of the insulators. It can be done by using spin pumping and spin-transfer torque (STT) [53]. Here, spin pumping refers to the transfer of spin angular momentum from magnetization precession to conduction-electron spin, a phenomenon which allows generation of a spin current from magnetization motion. STT is, in contrast, the reverse process of this spin pumping, that is, the transfer of angular momentum from conduction-electron spin to magnetization: the magnetization receives torque by absorbing a spin current. These two phenomena enable the mutual conversion of angular momentum between conduction-electron spin and magnetization.

Let us now consider the spin-pumping process. At the interface of a normal metal and a ferromagnetic insulator, conduction electrons in N interact with magnetic moments of FI through the s-d exchange interaction

$$\hat{H}_{sd} = -J_{sd} \sum_i \hat{\boldsymbol{S}}_i \hat{\boldsymbol{s}}_i \tag{9.7}$$

where $\hat{\boldsymbol{s}}_i$ and $\hat{\boldsymbol{S}}_i$ are the conduction-electron spin and the localized spin at site i at the interface, and J_{sd} is the exchange coupling strength between them. In the presence of microwave field, we assume a uniform precession of aligned localized spins, in which case $\hat{\boldsymbol{S}}_i$ is replaced by the magnetization $\boldsymbol{M}$ using the relation $\hat{\boldsymbol{S}}_i/S = \boldsymbol{M}/M_s$, and rewrite equation Eq. (9.7) as

$$\hat{H}_{sd} = -J_{ex} \int dx \boldsymbol{M}(t) a_{eff} \delta(x) \boldsymbol{m}_N(x,t) \tag{9.8}$$

where $J_{ex} = J_{sd}S/\hbar\gamma M_s$, $a_{eff} = v_e/a_s^2$ is the effective interaction range, v_e is the volume per conduction electron, a_s is the lattice constant. of localized spins at the interface, $\boldsymbol{m}_N(x,t)$ is the magnetization of conduction electrons. Eq. (9.8) indicates that $(\boldsymbol{M}/M_s)a_{eff}\delta(x)$ plays a role of the interface magnetization, which exerts the exchange spin torque on $\boldsymbol{m}_N(x,t)$

$$[\frac{d\boldsymbol{m}_N}{dt}]_{exchange} = -\gamma J_{ex} \boldsymbol{m}_N(x,t) \times \boldsymbol{M}(t) a_{eff} \delta(x) \tag{9.9}$$

through the exchange interaction at the interface. The magnetization of conduction electrons is written as $\boldsymbol{m}_N(x,t) = m_0 a_{eff}\delta(x) + \delta\boldsymbol{m}_N(x,t)$, where $\boldsymbol{m}_0 = \chi_N J_{ex} \boldsymbol{M}$ is the local equilibrium spin density, $\chi_N = \mu_B^2 N_F$ is the spin susceptibility of conduction electrons, and $\delta\boldsymbol{m}_N$ is the spin accumulation. By taking into account the exchange spin torque as well as the spin diffusion, the Bloch equation for $\boldsymbol{m}_N$ is given by

$$\begin{aligned} \frac{\partial \boldsymbol{m}_N(x,t)}{\partial t} &= -\gamma J_{ex} \boldsymbol{m}_N(x,t) \times \boldsymbol{M}(t) a_{eff} \delta(x) \\ &\quad - \frac{\delta \boldsymbol{m}_N}{\tau_{sf}} + D_N \nabla^2 \boldsymbol{m}_N(x,t), \end{aligned} \tag{9.10}$$

where τ_{sf} is the spin-flip relaxation time and D_N is the diffusion constant. By requiring that the precession frequency ($\sim GHz$) is much smaller than the spin-flip relaxation rate $\tau_{sf}^{-1} \sim 10^{12}s^{-1}$ and neglecting the small terms $M_{x,y}\delta m_N^z$, we obtain the solutions of Eq. (9.10) for the transverse spin accumulation $\delta m_N^+(x,t) = \delta m_N^x(x,t) + i\delta m_N^y(x,t)$, which are used to calculate the longitudinal spin accumulation $\delta m_N^z(x) = (1/\Gamma)\mathrm{Im}[\delta m_N^+(0,t)M_-/M_z]e^{-x/\lambda_N}$ and the spin current $j_s^z = -(e/\mu_B)D_N\nabla_x\delta m_N^z$, which yields the pumped spin current

$$j_s^z = -\frac{\hbar\omega}{4e}\frac{\sigma_N}{\lambda_N}\frac{1}{1+\Gamma^2}\left(\frac{M_+M_-}{M_z^2}\right)e^{-x/\lambda_N}, \tag{9.11}$$

where ω is the precession frequency, $M_\pm = M_x \pm iM_{x,y}$, $\lambda_N = \sqrt{D_N\tau_{sf}}$ is the spin-diffusion length, $\Gamma = (\tau_{ex}/\tau_{sf})(\lambda_N/a_{eff})$ and $\tau_{ex} = \hbar/(SJ_{sd})$. The factor (λ_N/a_{eff}) appears in Γ due to the exchange interaction restricted at the interface. Thus, the spin current strongly depends on the magnitude of the exchange coupling through . For $\Gamma \ll 1$ the spin current is independent of the exchange coupling. For $\Gamma \gg 1$, the spin current is proportional to the square of the exchange coupling. In in ordinary ferromagnets $(\tau_{ex}/\tau_{sf}) \ll 1$, whereas $(\lambda_N/a_{eff}) \gg 1$.

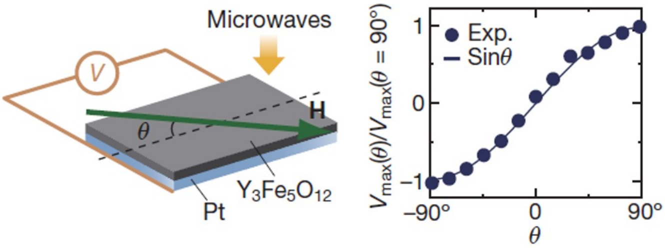

Figure 9.2: Sketch of the experimental setup (left) and *theta*-dependence of the maximum peak values of the ISHE voltage in the $V_{ISHE}(H)$ curves measured with application of microwaves. Adopted from [53].

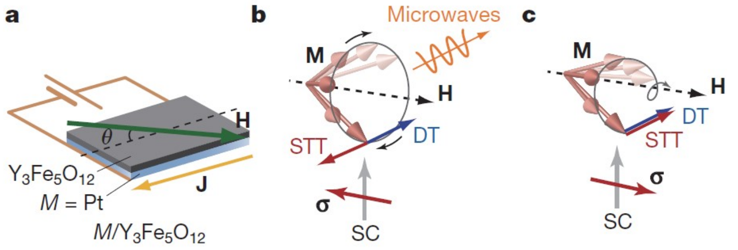

Figure 9.3: (a) Experimental setup; (b-c) schematic illustrations of the directions of spin-transfer torque acting on the magnetization and the magnetization-damping torque (DT) of the $Y_3Fe_5O_{12}$ layer at $\theta = 90°$ when $J > 0$ (b) and $J < 0$ (c). Adopted from [53].

The spin pumping and STT have been demonstrated experimentally [53]. Fig. 9.2 shows results of the spin pumping measurement. The observation of the spin pumping in $Pt/Y_3Fe_5O_{12}$ suggests the possibility of the reverse process: STT acting on the insulator $Y_3Fe_5O_{12}$. It has also been demonstrated experimentally. The schematic representation of the experiment is shown in Fig. 9.3.

The electric-signal transmission (via spin current) in the insulator $Y_3Fe_5O_{12}$ film can be achieved by making use of these phenomena together. Fig. 9.4 is a schematic illustration of the experimental setup.

9.3 Field of magnonics.

Magnon spintronics is the field of spintronics concerned with structures, devices and circuits that use spin currents carried by magnons [54]. It is a very rapidly developing field. It embraces a lot of interesting phenomena and provides a lot of benefits. Here is a short review of only few directions:

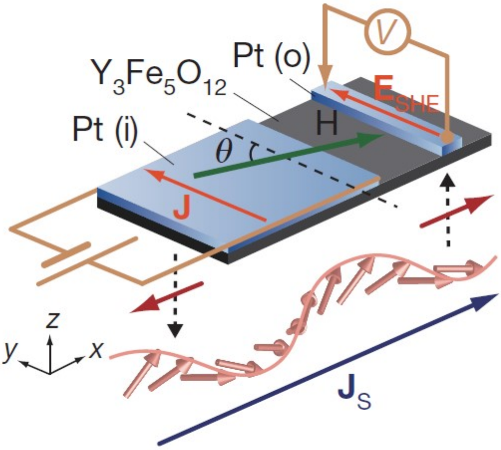

Figure 9.4: Experimental setup for the electron spin interconversion to magnon spin current and transmission of electric signals via the ferromagnetic insulator. The distance between input and output Pt electrodes is $1mm$. Adopted from [53].

Insulator-based spintronics. A magnon current has advantages as compared to a conventional spin-polarized electron current. It does not involve the motion of electrons and, thus, it is free of Joule heat dissipation. In low-damping magnetic dielectrics magnons can propagate over centimetre distances, whereas an electron-carried spin current is limited by the spin diffusing length, which does not exceed one micrometre.

Wide frequency range from GHz to THz. The wave frequency defines the maximum clock rate of a computing device. The magnon spectrum covers the GHz frequency range used nowadays in communication, and it reaches into the very promising THz range. For example, the edge of the first magnonic Brillouin zone in YIG lies at about 7 THz.

Macroscopic quantum phenomena. Magnons are bosons and can form a BoseEinstein condensate - a spontaneous coherent ground state established independently of the magnon excitation mechanism even at room temperature. A magnon supercurrent, a collective motion of condensed magnons driven by a phase gradient of a condensate wavefunction, can be used for low-loss information transfer.

Bibliography

[1] Nanomagnetism and spintronics, edited by Teruya Shinjo, Second Edition, Elsevier, 2014.

[2] A. Fert , I.A. Cambell, J. Phys. F: Metal Phys **6**, 849 (1976).

[3] Grunberg P, Schreiber R, Pang Y, Brodsky MB, Sowers H. Phys. Rev. Lett. **57**, 2442 (1986).

[4] Baibich MN, Broto JM, Fert A, Nguyen Van Dau F, Petroff F, Etienna P, et al. Phys. Rev. Lett. **61**, 2472 (1988).

[5] Parkin SSP, Mauri D. Phys. Rev. B **44**, 7131 (1991).

[6] Shinjo T, Yamamoto H. J. Phys. Soc. Jpn **59**, 3061 (1990).

[7] Gijs MAM, Lenczowski SKJ, Giesbers JB. Phys. Rev. Lett. **70**, 3343 (1993).

[8] Miyazaki T, Tezuka N. J. Magn. Magn. Mater. **151**, 403 (1995).

[9] Garcia N, Munoz M, Zhao Y-W. Phys. Rev. Lett. **82**, 2923 (1999).

[10] Ono T, Ooka Y, Miyajima H, Otani Y. Appl. Phys. Lett. **75**, 1622 (1999).

[11] Imamura H, Kobayashi N, Takahashi S, Maekawa S. Phys. Rev. Lett. **84**, 1003 (2000).

[12] M. Getzlaff, Fundamentals of magnetism, Springer-Verlag, Berlin Heidelberg, 2008.

[13] B.R. Coles, Spin disoder effects in the electrical resisitivities of metals and alloys, Adv. Phys. **7**, 40 (1958).

[14] Y. Xu, D.D. Awschalom, and J. Nitta, Handbook of Spintronics, Springer (2016).

[15] S. Bandyopadhyay, M. Cahay, Introduction to Spintronics, Second Edition, CRC Press, 2016

[16] Jedema FJ, Heersche HB, Filip AT, Baselmans JJA, van Wees BJ. Nature bf 410, 345 (2001); Nature **416**, 713 (2002).

[17] S. Datta and B. Das, Electronic analog of electro-optic modulator, Appl. Phys. Lett. **56**, 665 (1990).

[18] I. Zutic, J. Fabian, and S. Das Sarma, ”Spintronics: Fundamentals and applications”, Rev. Mod. Phys. **76**, 323 (2004).

[19] ”Hand book of spin transport and magnetism”, ed. by E.Y. Tsymbal and I.Zutic, CRC Press, 2012.

[20] Myers EB, Ralph DC, Katine JA, Louie RN, Buhrman RA. Science **285**, 867 (1999).

[21] Katine JA, Albert FJ, Buhrman RA, Myers EB, Ralph DC. Phys. Rev. Lett. **84**, 3149 (2000).

[22] Huai Y, Albert F, Nguyen P, Pakala M, Valet T. Appl Phys Lett **84**, 3118 (2004).

[23] Kubota H, Fukushima A, Ootani Y, Yuasa S, Ando K, Maehara H, et al. Jpn J Appl Phys **44**, L1237 (2005).

[24] Diao Z, Apalkov D, Pakala M, Ding Y, Panchula A, Huai Y. Appl Phys Lett **87**, 232502 (2005).

[25] Mangin S, Ravelosona D, Katine JA, Carey MJ, Terris BD, Fullerton EE. Nat Mater **5**, 210 (2006).

[26] J. Shibata, G. Tatara and H. Kohno, "A brief review of field- and current-driven domain-wall motion", J. Phys. D: Appl. Phys. **44** 384004 (2011).

[27] N.L. Schryer and L.R. Walker, J. Appl. Phys. **45**, 5406 (1974).

[28] A. Mougin, M. Cormier, J. P. Adam, P. J. Metaxas and J. Ferre, Europhys. Lett. **78**, 57007 (2007).

[29] G. S. D. Beach, C. Nistor, C. Knutson, M. Tsoi, and J. L. Erskine, Nature Mat. **4**, 741 (2005).

[30] J. Grollier, A. Chanthbouala, R. Matsumoto, A. Anane, V. Cros, F. Nguyen van Dau, and A. Fert, C. R. Physique **12**, 309 (2011).

[31] S. Parkin and S.-H. Yang, Nature Nanotech. **10**, 195 (2015).

[32] Yamaguchi A, Ono T, Nasu S, Miyake K, Mibu K, Shinjo T. Phys. Rev. Lett. **92** 077205 (2004); Phys. Rev. Lett. **96** 179904(E) (2006).

[33] Landau and Lifshitz "Course of theoretical physics, volume 4: V.B. Berestetskiii, E.M. Lifshitz, and L.P.

Pitaevskii, Quantum electrodynamics", Butterworth-Heinemann; 2 edition (1982).

[34] F. G. Pikus and G. E. Pikus, Conduction band spin splitting and negative magnetoresistance in A3B5 heterostructures, Phys. Rev. B **51**, 16928 (1995).

[35] G. Engels, J. Lange, Th. Schapers, and H. Luth, "Experimental and theoretical approach to spin splitting in modulation-doped $In_xGa_{1-x}As/InP$ quantum wells for $B \to 0$", Phys. Rev. B **55**, R1958 (1997).

[36] Landau and Lifshitz "Course of theoretical physics, volume 3: L.D. Landau and E.M. Lifshitz, Quantum mechanics", Butterworth-Heinemann; 3 edition (1981).

[37] J. E. Hirsch, "Spin Hall effect", Phys. Rev. Lett. **83**, 1834 (1999).

[38] J. Sinova, D. Culcer, Q. Niu, N. A. Sinitsyn, T. Jungwirth and A. H. MacDonald, Universal intrinsic Spin Hall Effect, Phys. Rev. Lett. **92**, 126603 (2004).

[39] E. G. Mishchenko, A.V. Shytov, and B. I. Halperin, Phys. Rev. Lett. **93**, 226602 (2004).

[40] S. D. Ganichev, M. Trushin, J. Schliemann, "Spin polarization by current", in Handbook of Spin Transport and Magnetism, 2nd ed. edited by E.Y. Tsymbal and I. Zutic (Chapman and Hall, 2016)

[41] V. M. Edelstein, Solid State Commun. **73**, 233 (1990).

[42] C. H. Li, O. M. J. vant Erve, J. T. Robinson, Y. Liu, L. Li and B. T. Jonker, Nature Nanotech. **9**, 218 (2014).

[43] A. Khaetskii, D. Loss, and L. Glazman, "Electron spin evolution induced by interaction with nuclei in a quantum dot", Phys. Rev. B **67**, 195329 (2003).

[44] Ashcroft, N. W. Mermin, N. D. Solid State Physics (Saunders, 1976).

[45] Slachter, A., Bakker, F. L., Adam, J. P. van Wees, B. J. Thermally driven spin injection from a ferromagnet into a non-magnetic metal. Nature Phys. **6**, 879882 (2010).

[46] G. E. W. Bauer, E. Saitoh and B. J. van Wees, Spin caloritronics, Nature Mat. **11**, 391 (2012).

[47] K. Uchida, S. Takahashi, K. Harii, J. Ieda, W. Koshibae, K. Ando, S. Maekawa, and E. Saitoh "Observation of the spin Seebeck effect", Nature **455**, 778 (2008).

[48] J. Flipse, F. K. Dejene, D. Wagenaar, G. E. W. Bauer, J. Ben Youssef and B. J. van Wees, Observation of the Spin Peltier Effect for magnetic insulators, Phys. Rev. B. **113**, 027601 (2014).

[49] P. Machon, M. Eschrig, and W. Belzig, Nonlocal Thermoelectric Effects and Nonlocal Onsager relations in a Three-Terminal Proximity-Coupled Superconductor-Ferromagnet Device, Phys. Rev. Lett. **110**, 047002 (2013).

[50] A. Ozaeta, P. Virtanen, F.S. Bergeret, and T.T. Heikkila, Predicted Very Large Thermoelectric Effect in Ferromagnet-Superconductor Junctions in the Presence of a Spin-Splitting Magnetic Field, Phys. Rev. Lett. **112**, 057001 (2014).

[51] S. Kolenda, M. J. Wolf, and D. Beckmann, Observation of Thermoelectric Currents in High-Field Superconductor-Ferromagnet Tunnel Junctions, Phys. Rev. Lett. **116**, 097001 (2016).

[52] S. Kolenda, C. Surgers, G. Fischer, and D. Beckmann, Thermoelectric effects in superconductor-ferromagnet

tunnel junctions on europium sulfide, Phys. Rev. B **95** 224505 (2017).

[53] Y. Kajiwara, K. Harii, S. Takahashi, J. Ohe, K. Uchida, M. Mizuguchi, H. Umezawa, H. Kawai, K. Ando, K. Takanashi, S. Maekawa, and E. Saitoh, Transmission of electrical signals by spin-wave interconversion in a magnetic insulator, Nature **464**, 262 (2010).

[54] A. V. Chumak, V. I. Vasyuchka, A. A. Serga and B. Hillebrands, Magnon spintronics, Nature Phys. **11**, 453 (2015).